ION IMPACT PHENOMENA

IN

ANODIC OXIDES

ION IMPACT PHENOMENA IN ANODIC OXIDES

by

LAM QUOC NGHI, B.A.Sc.

A Thesis

Submitted to the School of Graduate Studies

in Partial Fulfilment of the Requirements

for the Degree

Doctor of Philosophy

McMaster University

June 1971

DOCTOR OF PHILOSOPHY (1971) McMASTER UNIVERSITY

(Metallurgy and Materials Science) Hamilton, Ontario

TITLE: Ion Impact Phenomena in Anodic Oxides

AUTHOR: Lam Quoc Nghi, B.A.Sc (Université Laval, Québec, Canada)

SUPERVISOR: Professor R. Kelly

NUMBER OF PAGES: xv, 178

SCOPE AND CONTENTS:

In this thesis results are presented relating to sputtering coefficients of Kr on anodic oxides, high-dose depth distributions of Kr in Al_2O_3, Nb_2O_5, and WO_3, and amorphization in crystalline WO_3.

The comparison of the experimental sputtering data with Sigmund's theory permits the surface binding energy to be estimated. Possible contribution of volatility to sputtering will be discussed for the case of volatile oxides with stable gaseous multimers, namely MoO_3, V_2O_5, and WO_3.

The pronounced "range shortening" has been studied in detail for high doses of Kr in Al_2O_3, Nb_2O_5, and WO_3, and is shown analytically to be reasonable whenever there exists an appropriate spatial variation in the diffusion activation enthalpy. Effects of prebombardment and post-bombardment on depth distributions, as well as information on the migration of implanted dopants near room temperature, are argued as providing a self-consistent explanation for the above-mentioned "range shortening".

Depths of amorphization due to ion impact have been measured with WO_3. They are then used to deduce the critical fraction of atomic

displacements leading to amorphization, the mean size of discrete disordered regions, and estimates of the damage mean range for Kr-WO_3.

ACKNOWLEDGMENTS

I wish to express my particular thanks to Professor R. Kelly for his interest, continuous guidance, encouragement, help, and friendship throughout the various phases of this work and also, for his many valuable criticisms and suggestions during the preparation of this thesis.

The assistance offered by Professors G.R. Purdy and J. Shewchun who both served on the supervisory committee is appreciated. Thanks are extended to the staff and graduate students of the Department of Metallurgy and Materials Science for their helpful discussions and aid.

I am indebted to Professors R. Kelly, A.A. Lee, N.Đ. Hải, and Dr. P.Q. Đán for their help in solving some difficult social problems in the early stage of my graduate study.

Thanks are due to Mrs. S. Wutch for her skill and remarkable patience in typing the manuscript and to Mr. D.S. Hodgson for his assistance in the photographic work.

This project was supported by grants from the Defence Research Board and National Research Council of Canada to Professor R. Kelly and by a McMaster Graduate Scholarship to the author.

A special acknowledgment is addressed to my parents for their constant encouragement. Finally, I am deeply grateful to my wife, Hiền, for her great understanding and patient endurance.

TABLE OF CONTENTS

LIST OF ILLUSTRATIONS

LIST OF TABLES

CHAPTER 1

INTRODUCTION

This work is concerned with various aspects of ion bombardment of oxides, such as sputtering, depth distributions, diffusion of inert-gas ions, and bombardment-induced disorder.

In order to be able to estimate the loss of target material and to obtain depth-profiles of implanted Kr ions in oxides after high-dose ($\geq 10^{15}$ ions/cm^2) bombardment, sputtering coefficients for Kr^+ on various oxides must be determined. So far, several works on sputtering of metals have been published, the major ones being those of Wehner et al.[1], and of Almén and Bruce[2]. On the other hand, for the sputtering of oxides, the experimental results were very few and only concentrated on a limited number of oxides [3-8]. The study of sputtering of oxides is, however, very important, and has useful applications into ionic cleaning of surfaces, space research, and plasma containment (hence work on nuclear fusion). Furthermore, the comparison of the experimental results with Sigmund's theory[9] permits a rough estimate to be made of the otherwise elusive quantity, the surface binding energy.

Measurements of depth distributions of ions injected into solids are of interest firstly in themselves, because of the information they supply on the nature of atomic collisions. In addition, they play a basic role in determining the depths of p-n junction in implanted Si or Ge and in deducing depths of damage in reactor components.

There is increasing evidence that diffusion phenomena in ion-implanted solids do not follow normal diffusion kinetics at high doses. For example, ion depth profiles are sometimes found to move towards the surface after heavy-particle post-bombardments[6,10-12]. The pronounced "range shortening" for high doses of Kr in Al_2O_3, Nb_2O_5, and WO_3 will be argued to be a diffusion effect, and will be shown analytically to be reasonable whenever there is an appropriate spatial variation in the diffusion activation enthalpy[12]. Moreover, migration of implanted Kr has been demonstrated to occur near room temperature with a wide variety of solids, and can be argued as providing a self-consistent explanation for the decrease of ion range, i.e. the out-diffusion.

Many oxides and diamond-type materials amorphize when bombarded with heavy ions. The depths beneath the surface at which such amorphization ceases has been estimated for the particular case of crystallized WO_3 using appropriate techniques which are in general based on bombardment-enhanced solubility. Depths of disorder have then been used to deduce the critical fraction of atomic displacements leading to amorphization of crystalline WO_3.

This dissertation can conveniently be divided into two parts. In the first part, important concepts in treating atomic collisions (Chapter 2), theoretical analyses of sputtering of amorphous solids (Chapter 3), depth distributions of ions and damage (Chapter 4), and diffusion in ion-implanted solids (Chapter 5) are reviewed. The second part is concerned with experimental procedures (Chapter 6), techniques, results, and discussion on sputtering (Chapter 7), on depth distributions of Kr

in oxides (Chapter 8), and on bombardment-induced disorder in WO_3 (Chapter 9). A summary will be given in Chapter 10.

CHAPTER 2

RÉSUMÉ OF ATOMIC COLLISION THEORY

2.1 THE INTERATOMIC POTENTIAL

2.1.1 Why is the Atomic Interaction Potential Important?

During the past twenty years, interest in radiation damage work has led to many calculations of the dynamics of moving atoms in solids. These calculations obviously depend on the nature of the potential which is used to describe the interaction between colliding atoms. A full knowledge of the interaction potential is therefore essential to a proper description of all the problems of radiation damage science, e.g. formation, nature and extent of damage. Without such a knowledge we are not able to describe the regimes of energy loss for a charged particle, we cannot estimate the average number of displaced atoms produced by a primary knock-on, and we cannot determine the mean free paths for the moving atoms. Moreover, we cannot proceed with either the analytical or numerical analyses of focusing, channeling, and ranges of ions and damage in solids.

A large number of analytical and semi-empirical potentials has been proposed in the past (for detailed reviews, see references 13-15). Before considering the theoretical treatments of sputtering and of spatial distributions of ions and damage, it is useful in this chapter to make a short review of the more important potentials.

Consider two atoms with masses M_1 and M_2, nuclear charges Z_1e and Z_2e, and nuclear separation r. Provided one can assume two-body

interactions alone, the force between them can be described by a potential energy $V(r)$ which arises from interactions involving the electrons and the nuclei.

2.1.2 The Born-Mayer and Inverse-Power Potentials

The relation which best describes the atomic interaction of identical atoms at relatively large separations (between 0.5 Å and interatomic spacing) is the Born-Mayer equation or any other function having similar analytical form. For example, one possibility is:

$$V(r) = A \exp\left(-\frac{r}{B}\right) \qquad (2\text{-}1)$$

where A and B are constants to be determined from the equilibrium lattice spacing and from tne elastic moduli. This potential function may be shown to be approximately valid for separations in the vicinity of the equilibrium separation of nearest neighbours in the crystal. Abrahamson[16] has recently listed values for A and B which he considered best suited to fit the approximately exponential tail of his Thomas-Fermi-Dirac potentials for nearly every element[17].

2.1.3 The Hard-Sphere Potential

The interaction between two atoms might in some cases be likened to that between two billiard balls of fixed radius r_o. The potential $V(r)$ is zero, or constant, until the two atoms "touch", it then rises abruptly, becoming essentially infinite in a very small distance:

$$\begin{aligned} V(r) &= \infty \qquad \text{at } r < 2r_o \\ V(r) &= 0 \qquad \text{at } r > 2r_o \end{aligned} \qquad (2\text{-}2)$$

This model does not demonstrate the basic "softness" which characterizes the behaviour of atoms in nature, and there is the further

limitation of adopting a constant value of r_o for an atom, irrespective of its energy.

The energy-dependent (or modified) hard-sphere model, on the other hand, is possibly something of an improvement since, although the hard sphere limitation is retained, the radius of the atom does at least vary continuously with energy. Consider the collision between a moving atom with mass M_1 and kinetic energy E, and a stationary atom with mass M_2. In a centre_of_mass system (G-coordinates) the total kinetic energy of the system is equal to $EM_2/(M_1 + M_2)$, so that in a head-on collision we have:

$$V(2r_o) = \frac{M_2 E}{(M_1 + M_2)} \tag{2-3}$$

Now, if the Born-Mayer potential (equation (2-1)) is used for $V(2r_o)$, then the atomic radii can be shown to be dependent on energy in the following relation:

$$r_o(E) = \frac{B}{2} \ell n \frac{(M_1 + M_2)A}{M_2 E} \tag{2-4}$$

2.1.4 The Simple Coulomb Potential

This is the well-known relation which describes the interaction of two atoms at very small separations (0 to 0.03 Å):

$$V(r) = \frac{Z_1 Z_2 e^2}{r} \tag{2-5}$$

At larger distances, when there is a possibility of electrons entering the internuclear space, the electronic screening becomes important and the validity of this potential is therefore profoundly reduced. One then refers to a Screened Coulomb potential, of which there are many forms.

2.1.5 The Screened Coulomb Potential of Bohr

When the Coulomb field of the nucleus is screened by the orbital electrons, the interaction potential will, for certain distances of separation, take the form:

$$V(r) = \frac{Z_1 Z_2 e^2}{r} \exp\left(-\frac{r}{a}\right) \tag{2-6}$$

where a is the screening radius which is related to the Bohr radius of the hydrogen atom $a_o = 0.529$ Å by the relation:

$$a = \frac{0.8853\ a_o}{(Z_1^{2/3} + Z_2^{2/3})^{1/2}} \tag{2-7}$$

Values of a for various Z_1 - Z_2 combinations have been tabulated by Winterbon[18].

The Screened Coulomb potential is valid for small separations between 0 to 0.3 Å (or $\frac{r}{a}$ = 0 to 1). As the incoming ion of very high energy is slowed down by interactions with the lattice atoms the effect of the electron screening becomes more and more pronounced, until the collisions are best described in terms of an alternative screened potential.

2.1.6 The Thomas-Fermi-Firsov Potential

The TFF potential, which takes into account the change in electron energy connected with the mutual approach of the nuclei, has been formulated by Firsov[19-20] using the Thomas-Fermi model of the atom. The potential may be written as:

$$V(r) = \frac{Z_1 Z_2 e^2}{r} \Phi_o(y) \tag{2-8}$$

where the argument y used by Firsov is:

$$y = (Z_1^{1/2} + Z_2^{1/2})^{2/3} \frac{r}{a} \tag{2-9}$$

$\Phi_o(y)$ is the Thomas-Fermi screening function, of which values have been tabulated by Gombas[21].

The TFF potential is valid in the separation range from 0 to 1.3 Å (or $\frac{r}{a}$ = 0 to 8). This potential is very useful because its validity range covers the range of application of the Simple Coulomb, Screened Coulomb (Bohr), and Inverse Square potentials (to be discussed).

2.1.7 The Thomas-Fermi-Dirac (or Abrahamson) Potential

The large uncertainties which remained over the range of intermediate atomic separations (from 1 to 1.5 Å) prompted Abrahamson[22] to calculate a new potential, using the Thomas-Fermi-Dirac statistical model of the atom.

The fundamental distinction between the TF and TFD atomic models is that the latter takes account of exchange effects whereas the former does not.

The potential is determined as follows:

$$V(r) = \frac{Z_1 Z_2 e^2}{r} \Phi_o(y) + \left[\begin{matrix}\text{terms for electron} \\ \text{rearrangement}\end{matrix}\right] \quad (2\text{-}10)$$

This potential cannot be expressed in a simple analytical form, since the quantity in square brackets on the right side is complicated, involving a set of integrals.

The TFD potential was shown to be valid for separations between 0 and 1.5 Å (or $\frac{r}{a}$ = 0 to 10), though it has been emphasized recently by Wedepohl[23] that Abrahamson's work contains many errors, and the potential in reality offers little improvement.

2.1.8 Inverse Power Potentials

For analytical purposes it is very convenient sometimes to ex-

press $V(r)$ as some inverse power n of r. This is possible by fitting a function (constant)r^{-n} to one of the more exact potential functions (normally the TFF).

One of the advantages of inverse power potentials is that, for several integer values of n, there are simple exact scattering formulae, so that it becomes easy to estimate the accuracy of approximate solutions.

For example, for screened Coulomb interaction between an ion and an atom or between two atoms, Lindhard et al.[24] derived the following approximate form of the differential cross section:

$$d\sigma = \pi a^2 \frac{dt}{2t^{3/2}} f(t^{1/2}) \qquad (2\text{-}11)$$

where a = screening radius, given by equation (2-7),

$t = \varepsilon^2 \sin^2 \frac{\gamma}{2}$,

γ = scattering angle in the centre-of-mass system (G-coordinates),

ε = a reduced parameter of energy, defined in equation (2-40),

$f(t^{1/2})$ = a function that depends on the assumed form of the screening function.

The function $f(t^{1/2})$, which has a complicated analytical form, has been calculated numerically by Lindhard et al.[24]

As an analytical approximation, $f(t^{1/2})$ can be written as[25]:

$$f_A(t^{1/2}) = \lambda' t^{1/6}[1 + (2\lambda' t^{2/3})^{2/3}]^{-3/2} \qquad (2\text{-}12)$$

where $\lambda' = 1.309$

It is seen, in Figure 2-1, that the two curves agree to well within the accuracy of the Thomas-Fermi-Firsov approximation.

At small t equation (2-12) goes over into $f(t^{1/2}) = \lambda' t^{1/6}$, which is a special case of the power approximation[24]:

$$f(t^{1/2}) = \lambda_m t^{1/2 - m} \tag{2-13}$$

where $m = \frac{1}{n}$

Three examples of the above equation for $m = \frac{1}{3}, \frac{1}{2}$, and 1 are also shown in Figure 2-1, with

$$\left.\begin{aligned} \lambda_{1/3} &= \lambda' = 1.309 \\ \lambda_{1/2} &= 0.327 \\ \lambda_1 &= 0.5 \end{aligned}\right\} \tag{2-14}$$

It is found that the case $m = \frac{1}{3}$ is an excellent approximation at small values of t, $m = \frac{1}{2}$ is a reasonable over-all approximation, and $m = 1$ is appropriate for $t \gg 1$.

In general, equation (2-13) describes approximately the scattering from an inverse power potential of the form $V(r) \propto r^{-n}$. The cross sections of equation (2-13) for several values of m have usually been used in radiation-damage work since they allow simple analytic solution of the integral equations for range and damage distributions.

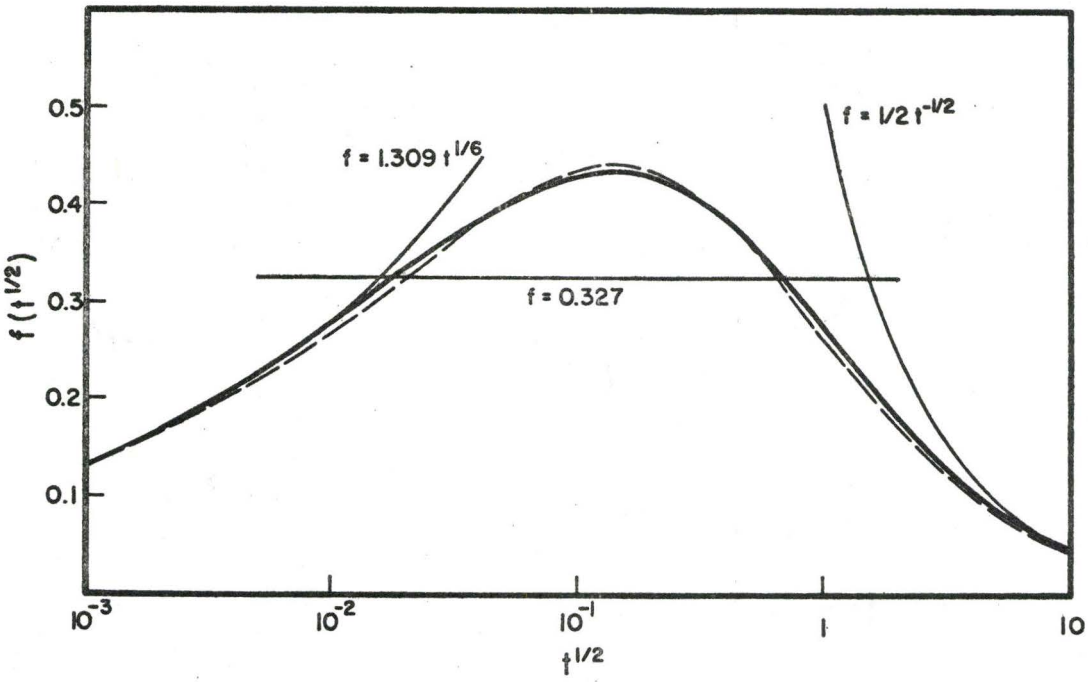

Figure 2-1 Reduced differential cross sections calculated from the TFF potential. Thick solid line: Lindhard's numerical result; dashed line: equation (2-12); thin solid lines: power cross sections, equation (2-13) (after Winterbon, Sigmund, and Sanders[25]).

2.1.9 The Nielsen Potential (or Inverse Square Potential)

If we fit an inverse square function $V(r) \propto r^{-2}$ to the Screened Coulomb potential of Bohr at r = a obtaining the same ordinate, slope, and curvature, then we have the function:

$$V(r) = \frac{Z_1 Z_2 e^2}{r} \left(\frac{a}{2.718r}\right) \qquad (2\text{-}15)$$

This relation is called the Nielsen potential though is really equivalent to an inverse power potential with m = $\frac{1}{2}$ as described in the

preceding section. For a limited range of r = 0.08 to 1.3 Å (or $\frac{r}{a}$ = 0.5 to 8), this can be used as an appropriate potential.

2.1.10 The Wedepohl Potential

Recently, Wedepohl[15] has shown that the TFF potential is given to good accuracy by the simple analytical form:

$$V(r) = C \exp(-\alpha r^{1/4}) \qquad (2\text{-}16)$$

where $C = 1.55 \times 10^{14} Z_1 Z_2 Z_o^{1/3}$ eV

and $\alpha = 8.98 Z_o^{1/12}$ Å$^{-1/4}$

$Z_o = \frac{1}{4}(Z_1^{1/2} + Z_2^{1/2})^2$

The r.m.s. difference between equations (2-16) and (2-8) is only 1.5% over the range $0.3 < y < 16$. This includes the whole range of validity of the TFF potential with the exception of extremely small separations which are not of interest in radiation damage work (at least that involving heavy ions).

2.2 BASIC APPROACHES TO STUDY ATOMIC COLLISIONS

In this section the primary event,which is the collision between a charged particle and an atom of the lattice, will be considered. We shall assume that collisions are elastic and two-bodied (the chance of correlation effects due to neighbouring atoms being assumed to be very small) and, further, that velocities are small enough for non-relativistic mechanics to apply.

Our aim here is to review the four basic approaches to calculate the scattering angle γ, which determines the collision orbits, and the scattering cross sections, which are the important parameters in radiation damage calculations. Thus, knowing these, we can deduce the mean recoil energy, stopping powers, specific energy loss, rate of displacement,

average square fluctuation in energy transfer, total range, etc.....

2.2.1 The Exact Solution

By considering the conservation of energy and angular momentum in a collision in G-coordinates (as illustrated in Figure 2-2) and assuming the interatomic potential $V(r)$ appropriate for the chosen nuclear separations, one can have a time-independent equation for describing the orbit[26]:

$$\frac{du}{d\psi} = \left\{\frac{1}{p^2}\left[1 - \frac{V(u)}{E}\,\frac{M_1 + M_2}{M_2}\right] - u^2\right\}^{1/2} \qquad (2\text{-}17)$$

where p = impact parameter

$u = \frac{1}{r}$

and ψ = angle, described in Figure 2-2.

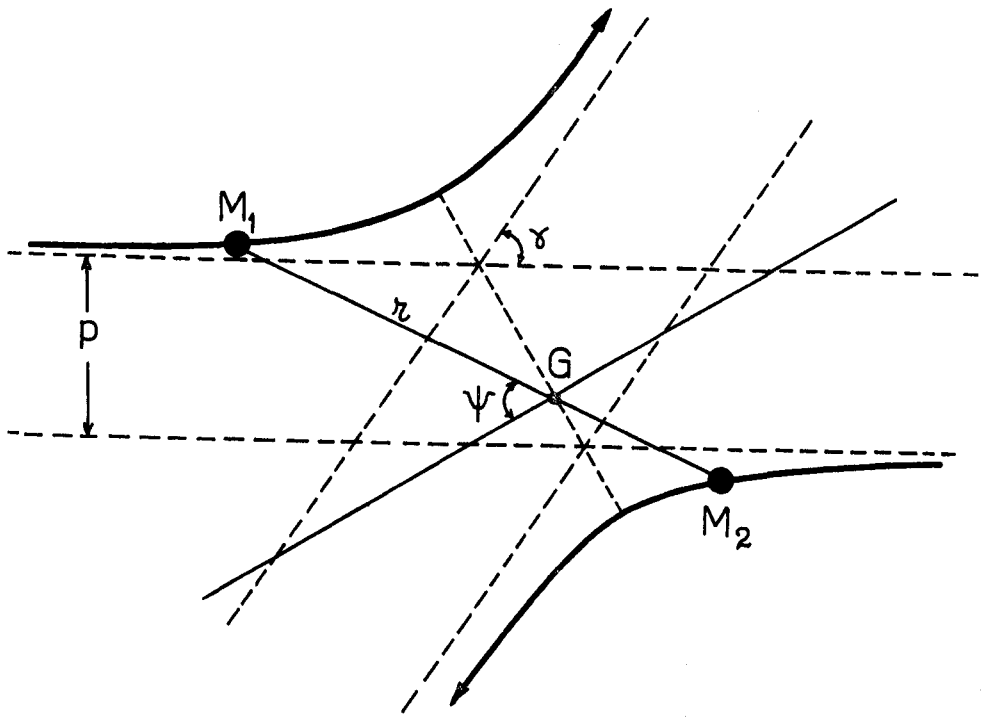

Figure 2-2 Collision orbits in G-coordinates

The scattering angle γ is found from the above equation by integrating $d\psi$ from $\gamma/2$ to $\pi/2$:

$$\gamma = \pi - 2\int_0^{1/\rho} \{\frac{1}{p^2}\left(1 - \frac{V(u)}{E} \cdot \frac{M_1 + M_2}{M_2}\right) - u^2\}^{-1/2} du \qquad (2\text{-}18)$$

where ρ = distance of closest approach

Explicit evaluation of the integral in equation (2-18) is only possible for simple potentials such as the Coulomb (equation (2-5)) and Inverse Square (equation (2-15)). In nearly all other cases difficulties may be involved and numerical methods must be employed.

The distance of closest approach ρ, in the upper limit of u, is the value of r when $\psi = \pi/2$. Since $\frac{du}{d\psi} = 0$ when $\psi = \pi/2$, ρ is given, from equation (2-17), by:

$$\frac{V(\rho)}{1-(p/\rho)^2} = \frac{M_2 E}{M_1 + M_2} \qquad (2\text{-}19)$$

The relation between γ and p can therefore be obtained, just by combining equation (2-19) with equation (2-17). For example, in the case of the Inverse Square potential, we have:

$$\gamma = \pi\{1 - (1 + a^2/2.718p^2\varepsilon)^2\} \qquad (2\text{-}20)$$

with ε, which is proportional to the energy, given by equation (2-40).

The transferred energy is determined by:

$$E_2 = \Lambda E \sin^2(\gamma/2) \qquad (2\text{-}21)$$

where

$$\Lambda = \frac{4M_1M_2}{(M_1 + M_2)^2} \qquad (2\text{-}22)$$

From equation (2-20), it follows that for an Inverse Square potential:

$$E_2 = \Lambda E \cos^2 \{\Pi/2(1 + a^2/2.718p^2\varepsilon)^{1/2}\} \tag{2-23}$$

Expressing p^2 in terms of E_2, differentiating, and using the relation:

$$d\sigma = 2\Pi p dp \tag{2-24}$$

we obtain:

$$\frac{d\sigma}{dE_2} = \frac{4a^2\alpha}{\Lambda E\varepsilon(1 - 4\alpha^2)^2\,[x(1 - x)]^{1/2}} \tag{2-25}$$

with $x = E_2/\Lambda E$ and $\Pi\alpha = \cos^{-1}\sqrt{x}$

For small x, equation (2-25) can be reduced to:

$$\frac{d\sigma}{dE_2} \simeq \frac{\Pi^2 a^2 (\Lambda E)^{1/2}}{8(2.718)\varepsilon E_2^{3/2}} \tag{2-26}$$

The total cross section for collisions with E_2 anywhere in the range $\check{E}_2$ to ΛE is therefore:

$$\sigma = \int_{\check{E}_2}^{\Lambda E} \frac{d\sigma}{dE_2}\, dE_2 \tag{2-27}$$

$$\sigma = \frac{\Pi^2 a^2 (\Lambda E)^{1/2}}{4(2.718)\varepsilon \check{E}_2^{1/2}} \tag{2-28}$$

where $\check{E}_2$ is the minimum recoil energy which is just capable of producing damage, and ΛE is the maximum possible energy transfer.

2.2.2 The Impulse Approximation

Consider a glancing collision, shown in Figure 2-3, between an atom of mass M_1 and energy E and a stationary atom of mass M_2.

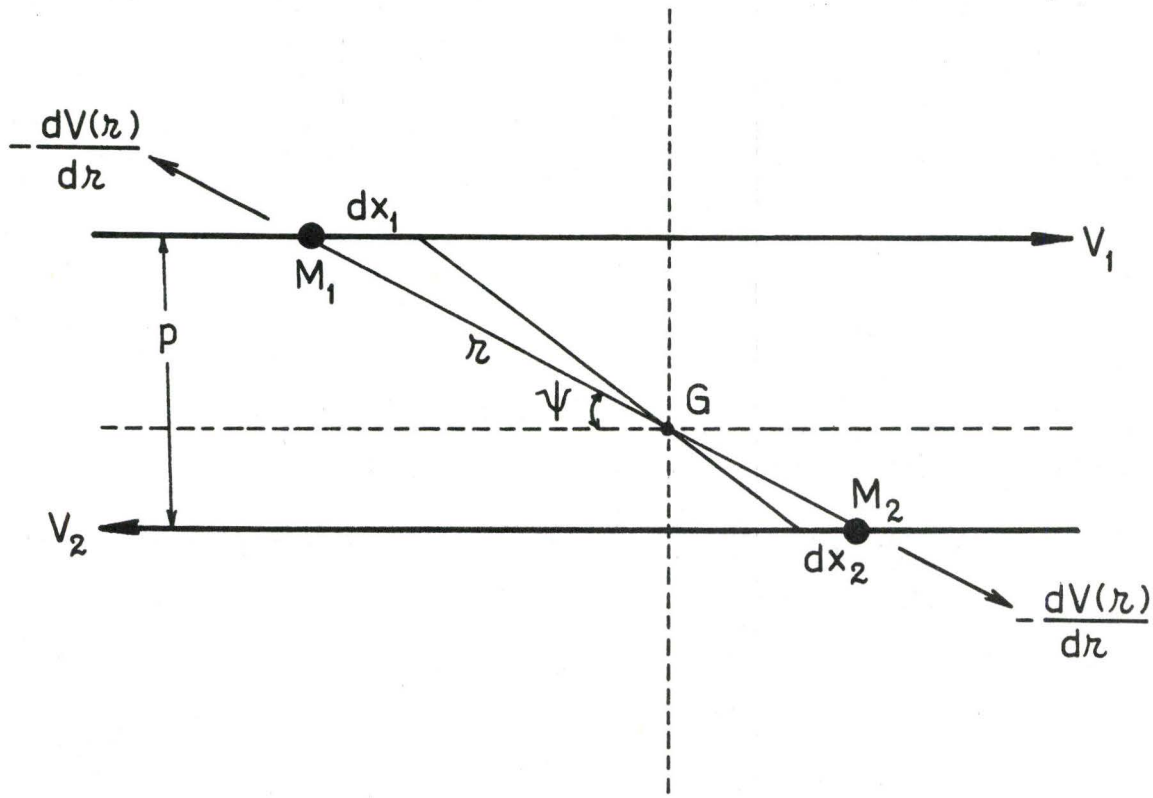

Figure 2-3 Glancing collision in G-coordinates.

For this type of collision γ must be small enough such that the velocity of either particle does not alter substantially throughout the collision. The orbits are then approximately straight lines running parallel at a separation p. The deflection of the moving atom can be approximated by the ratio of the transverse momentum to the momentum along

the original path:

$$\gamma = \frac{\Delta P_\perp}{M_1 V_1} = \frac{\Delta P_\perp}{M_2 V_2} \tag{2-29}$$

The momentum transferred perpendicular to the trajectory of an atom in a glancing collision is in turn given by the impulse approximation as:

$$\Delta P_\perp = \frac{1}{u_1} \int_{-\infty}^{+\infty} \{- \frac{dV(r)}{dr}\} \frac{p dr}{(r^2 - p^2)^{1/2}} \tag{2-30}$$

where u_1 is the velocity of the incident particle before collision in laboratory (L) coordinates.

The transferred energy E_2 is finally found as:

$$E_2 = \frac{(\Delta P_\perp)^2}{2M_2} \qquad \propto \quad \frac{1}{E} \tag{2-31}$$

where we have used:

$$V_1 = \frac{M_2 u_1}{(M_1 + M_2)} \tag{2-32}$$

A characteristic of the approximation is that E_2 is always proportional to E^{-1}, irrespective of the potential used.

Knowing the relations between γ and p^2, or between p^2 and E_2 we are therefore able to compute the scattering cross sections, using equations (2-24) and (2-27).

2.2.3 The Hard-Sphere Approximation

In collisions which are closer to head-on ($p \simeq 0$ and $\gamma \simeq \pi$) the hard-sphere approximation is often applicable. This approximation is clearly a drastic simplification, but has proved a very useful one in a number of rudimentary calculations on atomic collision phenomena. The interaction of two atoms is likened to that between two billiard balls

of radii R_1 and R_2 such that in any collision their centers are separated by a distance $\rho_o = R_1 + R_2$, as illustrated in Figure 2-4.

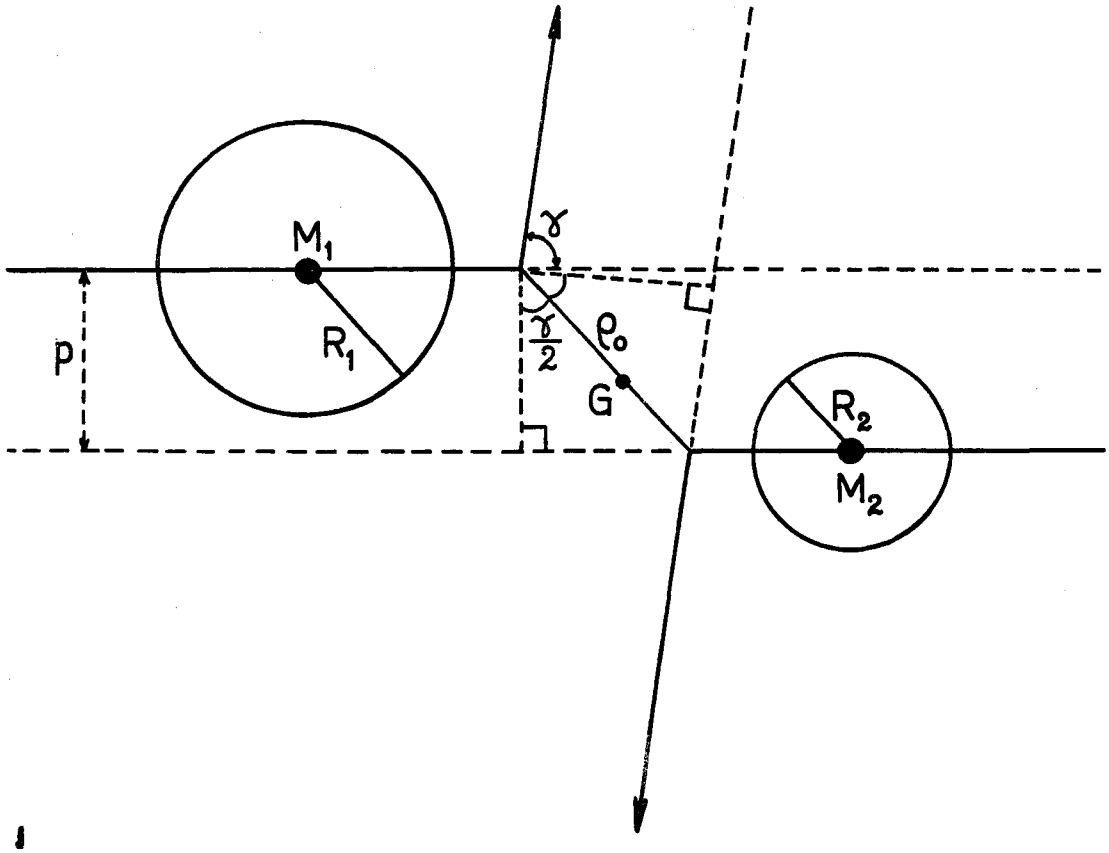

Figure 2-4 Hard-Sphere scattering in G-coordinates.

The potential energy at the moment of collision $V(\rho_o)$ will be equal to asymptotic kinetic energy in G-coordinates given by:

$$V(\rho_o) = \frac{M_2 E}{(M_1 + M_2)} \tag{2-33}$$

This relation defines the distance of closest approach, ρ_o.

From Figure 2-4, if ρ_o is known we have, by a simple geometrical argument:

$$p = \rho_o \cos \gamma/2 \tag{2-34}$$

Differentiating equations (2-34) and (2-21), we obtain:

$$d\sigma = 2\pi p dp = \pi \rho_o^2 \frac{dE_2}{\Lambda E} \tag{2-35}$$

Alternatively, integrating over the range of E_2, one gets:

$$\sigma \simeq \pi \rho_o^2 \tag{2-36}$$

This approximation becomes worse for small values of γ and to some extent it is complimentary to the impulse approximation.

2.2.4 Power-Law Scattering

If we use an inverse power potential of the form:

$$V(r) = \frac{\text{constant}}{r^{1/m}} \qquad \text{with } 0 < m \leq 1 \tag{2-37}$$

to describe the interaction potential between the incoming ion and the target atom, then the scattering cross sections can be written approximately as [24,27-28]:

$$d\sigma \simeq \frac{C dE_2}{E^m E_2^{1+m}} \tag{2-38}$$

and

$$\sigma \simeq \frac{C}{m E^m E_2^m} \tag{2-39}$$

where C is a quantity dependent on the value of m. In the reduced parameters of Lindhard et al.[27]:

$$\varepsilon = E \frac{aM_2}{Z_1 Z_2 e^2 (M_1 + M_2)} \tag{2-40}$$

$$\rho = RN4\pi a^2 \frac{M_1 M_2}{(M_1 + M_2)^2} \tag{2-41}$$

the quantity C in equations (2-38) and (2-39) can be expressed as:

$$C = \frac{\pi}{2} \lambda_m a^2 \left(\frac{E}{\varepsilon}\right)^{2m} \Lambda^m \tag{2-42}$$

with λ_m defined in equation (2-14) and Λ given by equation (2-22).

The nuclear stopping power is therefore defined as follows:

$$S_n(E) = \int_0^E E_2 d\sigma = \frac{C}{1-m} \Lambda^{1-m} E^{1-2m} \tag{2-43}$$

Equations (2-38) and (2-39) are used, with good accuracy, for a power potential, but can also be employed to describe scattering by the TFF potential within certain limits of projectile energy[24]. In general, if ~20% accuracy in both stopping and path length (to be discussed) is required for the power cross sections to be acceptable we obtain the following ranges of validity[25]:

$$m = \frac{1}{3} \quad \text{for } \varepsilon \lesssim 0.2$$

$$m = \frac{1}{2} \quad \text{for } 0.08 \lesssim \varepsilon \lesssim 2$$

At very high energies, $\varepsilon \gtrsim 3$, m = 1 could be used.

CHAPTER 3

THEORETICAL ANALYSES OF SPUTTERING OF AMORPHOUS SOLIDS

3.1 QUALITATIVE PICTURE OF SPUTTERING

When a solid is bombarded with energetic particles, many phenomena can arise. Which ones are possible or predominate depends largely on the kinetic energy of the incident particles. At energies exceeding roughly 25 eV, the dislodging of atoms and their ejection into the gas phase begin to play a decisive role. This process is called physical sputtering.

As shown schematically in Figure 3-1, the impinging ion penetrates the surface of the target and travels its mean free path before undergoing a series of collisions with target atoms. Atoms that recoil with sufficient energy suffer secondary collisions, thereby creating another generation of recoiling atoms:

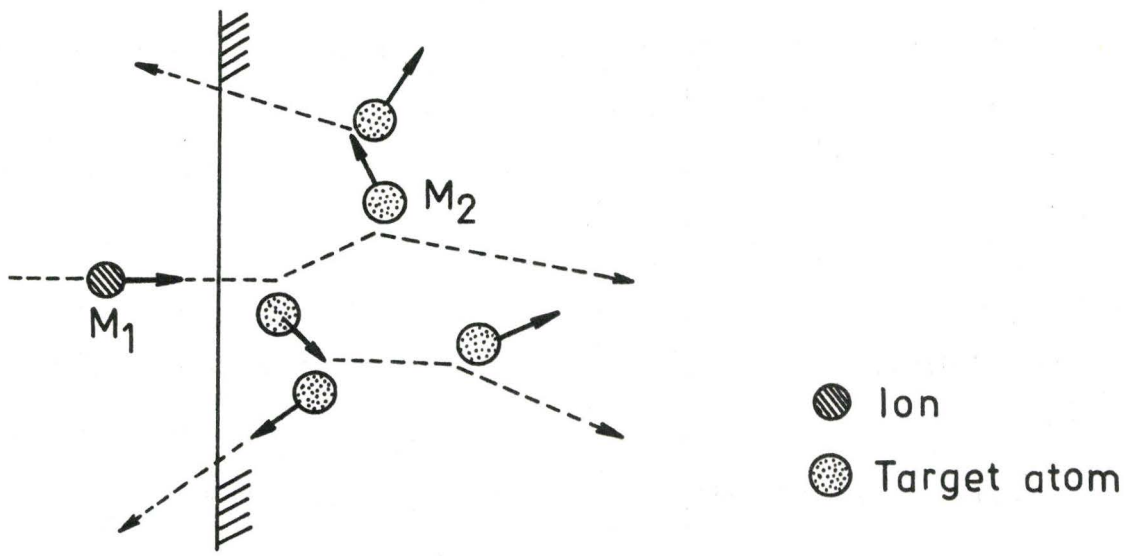

Figure 3-1 Collisions leading to sputtering process.

Both the ion itself and energetic recoil atoms have the possibility of getting scattered through the surface by a series of collisions from a depth that may be a certain fraction of the total ion range. The slowing-down paths of both the ion and all energetic recoils are surrounded by clouds of higher-order recoil atoms with very low energy. These atoms have small ranges and therefore can only get sputtered if they are located originally within a couple of atomic layers from the surface. Note that high-order recoil atoms account for the major portion of the number of sputtered atoms, because, according to Thompson[29], the energy distribution of sputtered atoms peaks heavily at very small energies.

The sputtering coefficient, which is the number of ejected atoms per incident ion, depends on the nature of the ions, their energies, the nature of the target, and the angle of incidence.

3.2 EARLY THEORETICAL MODELS

Various works on the incident-angle dependence of the sputtering coefficient[1,30-33] and on the energy distribution of ejected atoms[29,35-37] have clearly demonstrated that sputtering is indeed a momentum-transfer process. However, the formulation of this concept in an adequate theory which would explain these experimental results as well as many others such as the dependence of the sputtering coefficient on the nature of target, mass and energy of the bombarding ion, and direction of ion impact relative to crystallographic directions is a highly complicated problem.

Since 1955, several theoretical treatments of the sputtering process have been developed. The most important theories, which use the concept of momentum transfer from the incident particle to the lattice atom, are possibly those of Keywell[38], of Goldman and Simon[39], of Pease[40], of Rol et al.[32-33], of Odintsov[41], of Onderdelinden et al.[42-44],

of Martynenko[45], and of Sigmund[9,46].

In the following sections, we are going to review several theoretical analyses of the sputtering of amorphous (and polycrystalline) materials, excluding the dependence of the sputtering coefficient on the direction of impingement relative to crystallographic axes, i.e. anisotropy of the energy transfer within the lattice.

3.2.1 Keywell's Theory

One of the earliest theories of sputtering employing many concepts taken from radiation damage theory was described by Keywell[38]. He modified a neutron cooling theory so that it could be used to calculate how the incident particle transfers its energy in successive collisions to the target atoms. He assumed that the collisions are of the hard sphere type and that the number of sputtered atoms could be related to that of displaced atoms.

The number of displacements, n_d, produced by the n^{th} collision was assumed to be related to the average energy, $\overline{E}_n$, transferred to the lattice atom in the form:

$$n_d = \left(\frac{\overline{E_n}}{E_d} \right)^{1/2} \qquad (3\text{-}1)$$

where E_d is the displacement energy. The total number of displaced atoms, N_D, was found by summing over all collisions. In addition, the probability that the incident particle penetrates into the target, the probability that it rebounds on the first collision, and the probability that an atom displaced from a distance x below the surface might be captured in the lattice before it could escape from the surface have also been taken into account.

From such considerations, Keywell derived the following expression for the sputtering coefficient S:

$$S = \left(\frac{E}{E_d}\right)^{1/2} F(P,n) \qquad (3\text{-}2)$$

where F(P,n) is a semi-empirical quantity which depends partly on the above-mentioned probabilities and the possible number of collisions that an ion can make with the lattice atoms.

According to equation (3-2) the sputtering coefficient S varies as $E^{1/2}$ in first approximation. This relation was found to be approximately correct in some cases and certain energy ranges. The theory ignored energy losses due to electronic excitations and assumed a random target, so that crystallographic effects obviously could not be explained. It should be noted that Keywell used the erroneous relation $n_d=(\bar{E}_n/E_d)^{1/2}$ instead of the $E/2E_d$ derived by Kinchin and Pease[47]. However, for ions incident at very low energies the difference between these expressions is not too large. In addition, the assumption of hard-sphere collisions and the non-analytical form of equation (3-2) can involve drastic limitations in the application of the theory.

3.2.2 Theory of Rol, Fluit, and Kistemaker

In 1960 Rol et al.[32-33] proposed that only the collisions between ions and lattice atoms which take place near the surface are responsible for sputtering. The sputtering coefficient is therefore proportional to the average energy dissipated by the impinging particle in the first few atomic layers by elastic scattering events. The probability that collision will take place near the surface is inversely proportional to the mean free path, λ, of the ion, so that the coefficient can be ex-

pressed as:

$$S = \frac{K}{\lambda \cos \psi} \cdot \frac{M_1 M_2}{(M_1 + M_2)^2} E \qquad (3\text{-}3)$$

where ψ is the angle of incidence and K, which is a different constant for each target material, can be adjusted to fit the experimental data. When Almén and Bruce[2] examined their sputtering coefficient results in terms of the theory of Rol et al. for 10 to 65 keV Ne^+, Ar^+, and Xe^+ which were normally incident on a wide variety of metals, they reached the following conclusion:

$$K = A \exp[-B M_1^{1/2} E_b/(M_1 + M_2)] \qquad (3\text{-}4)$$

where A and B are constants and E_b is the surface binding energy of the target atoms.

The mean free path, λ, is given as usual in terms of the target atomic density, N, and the total scattering cross section, σ:

$$\lambda = 1/N\sigma \qquad (3\text{-}5)$$

Rol et al. have calculated λ from the hard-sphere approximation, in which, as we have seen in Section 2.2.3, $\sigma \simeq \pi \rho_o^2$ where ρ_o is the distance of closest approach, which is, however, determined from the screened Coulomb potential of Bohr. This approximation obviously has a very small range of applicability. The model also fails to take account of the effects of electronic excitation in the high-energy region and of anisotropy of the energy transfer within the lattice of a monocrystal. Moreover, the constant of proportionality K in equations (3-3), and (3-4) is empirical and possibly varies with interatomic potentials used[48]. The theory is therefore not analytical. However, for amorphous (or polycrystalline) materials

and low energies, the theoretical estimates were found to be in good agreement with the experimental results[32-33].

With the present availability of theories and results for ion ranges in solids, we would suggest here, however, to either use power-law approximation to calculate λ or replace λ by experimental (or theoretical) values of ion ranges.

(a) Using a power scattering cross section, equation (2-39), we have:

$$\lambda = \frac{1}{N\sigma} = \frac{m E^m \overset{v}{E}_2^m}{NC} \tag{3-6}$$

where $\overset{v}{E}_2$, which is the minimum recoil energy just capable of producing damage, can be given a value of 25 eV, and C is determined by equation (2-42). The value m = 1/3 is to be preferred for the work reported here ($\varepsilon < 0.2$), though m = 1/2 would be used for higher energies.

For the case of normal incidence, the sputtering coefficient can therefore be written as:

$$S = K_a \cdot \frac{NC}{m\overset{v}{E}_2^m} \cdot \frac{M_1 M_2}{(M_1 + M_2)^2} \cdot E^{1-m} \tag{3-7}$$

where K_a is a constant.

(b) The use of range parameters also gives a possibility to re-express the theory of Rol et al.. Thus, if R_m is the experimental median range of an ion in a random target, we can write:

$$S = \frac{K_b}{R_m} \cdot \frac{M_1 M_2}{(M_1 + M_2)^2} \cdot E \tag{3-8a}$$

where K_b can be adjusted to fit the sputtering data.

If the experimental values of R_m are not available, the theoretical estimates of Lindhard et al.[27] can be used. In that case, we have:

$$S = \frac{K_c}{\langle R \rangle} \frac{M_1 M_2}{(M_1 + M_2)^2} \cdot E \qquad (3\text{-}8b)$$

where K_c is again a constant.

3.3 SIGMUND'S THEORY

3.3.1 General

A completely analytical approach to sputtering has recently been formulated by Sigmund[9], using the methods of transport theory and considering a random target with a plane surface. A Boltzmann-type integro-differential equation was employed together with the power approximation to the Thomas-Fermi-Firsov cross section and a planar-potential barrier at the surface.

The calculation consists of a number of steps: (1) to determine the amount of energy deposited by energetic particles (ion and recoil atoms) near the surface; (2) to convert this energy into a number of low-energy recoil atoms; (3) to determine how many of these atoms come to the very surface; and (4) to select those atoms that have sufficient energy to overcome the surface binding forces. There will be needed only one basic equation, not four. The essential input quantities will be the cross sections for scattering of high-energy ions and atoms, the cross section for scattering of low-energy atoms, and the surface-barrier energy. Two main stages of the collision cascade must be distinguished: first, the slowing down of the primary ion and all recoiling atoms that have comparable energies - these particles determine the spatial extent of the cascade; second, the creation and slowing down of low-energy recoils that constitute

the major part of all atoms set in motion. The separation of the cascade into two distinct stages has the consequence that two characteristic depths are important for the qualitative understanding of the sputtering process. First, the high-energy scattering events that eventually lead to sputtering take place within a certain layer near the surface, the thickness of which depends on ion mass and energy and on ion-target geometry. In the elastic collision region, this thickness is a sizable fraction of the ion range. Second, the majority of sputtered particles originate from a very thin surface layer, because small energies dominate. High-energy collisions are characterized by Thomas-Fermi-Firsov type cross sections, while a Born-Mayer-type cross section is applied in the low-energy region. The electronic stopping is included when needed for high-energy scattering.

3.3.2 Basic Equations

Consider an arbitrary ion starting its motion at a time $t = 0$ in a plane $x = 0$ with a velocity $\vec{v}_o$, as shown in Figure 3-2.

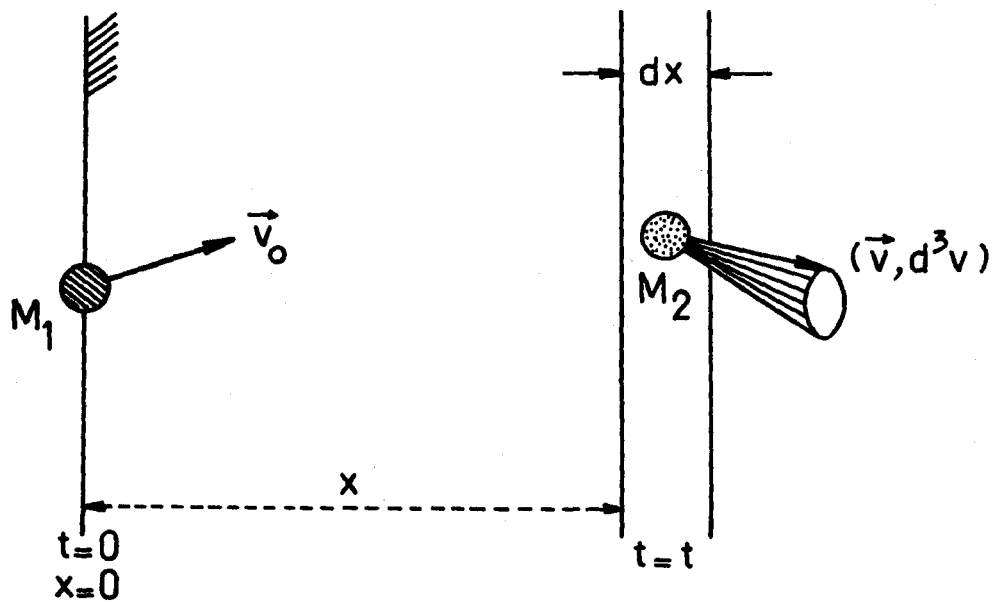

Figure 3-2 Geometry of sputtering calculation.

The average number of atoms with velocity ($\vec{v}$, d^3v) penetrating, as a consequence of the ion impact, the plane at x in a time interval dt is given by:

$$G(x,\vec{v}_o,\vec{v},t)\ d^3v\ |v_x|dt$$

where v_x is the x-component of $\vec{v}$, and $G(x,\vec{v}_o,\vec{v},t)$ is a function that must be defined.

The sputtering coefficient for backward sputtering of a planar target at x = 0 is then:

$$S_b = \int |v_x| d^3v \int_0^\infty G(0,\vec{v}_o,\vec{v},t)dt \qquad (3\text{-}9)$$

where the integration over d^3v extends over all $\vec{v}$ with negative x-components large enough to overcome surface binding forces.

In an isotropic and homogeneous medium, the function $G(x,\vec{v}_o,\vec{v},t)$ will satisfy Boltzmann's equation. Consider a particle moving at t = 0 in a plane at x = 0. After a time δt, it may or may not have made a collision. Figure 3-3 shows the geometry of a scattering event in the laboratory system where $\vec{v}'$ is the velocity of scattered particle, $\vec{v}''$ is the velocity of recoiling atom. Let N be the atomic density of the target , $d\sigma = d\sigma(\vec{v}_o,\vec{v}',\vec{v}'')$ be the ion-target differential cross section, and η be v_{ox}/v_o. By a standard argument used by Lindhard et al.[27] and Sanders[49], the function $G(x,\vec{v}_o,\vec{v},t)$ can be expressed as follows:

$G(x,\vec{v}_o,\vec{v},t)$ = (probability of creation of a scattered particle at x with $\vec{v}'$) + (probability of creation of a recoiling particle at x with $\vec{v}''$) + (probability of appearance of a non-colliding particle at x with $\vec{v}$)

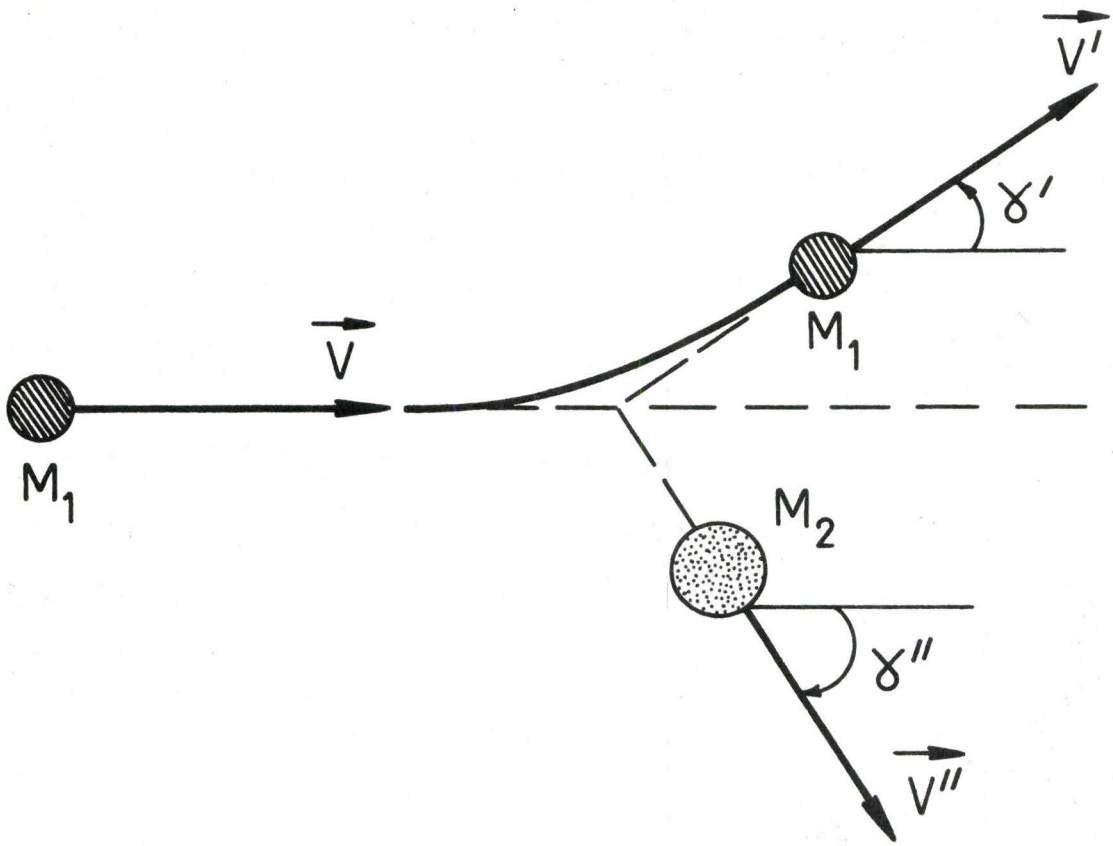

Figure 3-3 Single-scattering event in L-coordinates

$$= N v \delta t \int d\sigma [G(x,\vec{v}',\vec{v},t) + G(x,\vec{v}'',\vec{v},t)$$

$$+ (1 - N v \delta t \int d\sigma)\, G(x - \eta v \delta t, \vec{v}_o, \vec{v}, t - \delta t) \qquad (3\text{-}10)$$

Expanding this equation in powers of δt and taking the first order terms, it is straightforward to conclude:

$$-\frac{1}{v}\frac{\partial}{\partial t} G(x,\vec{v}_o,\vec{v},t) - \eta \frac{\partial}{\partial x} G(x,\vec{v}_o,\vec{v},t) = N \int d\sigma [G(x,\vec{v}_o,\vec{v},t) -$$

$$G(x,\vec{v}',\vec{v},t) - G(x,\vec{v}'',\vec{v},t)] \qquad (3\text{-}11)$$

In view of equation (3-9), one is only interested in the function:

$$F(x,\vec{v}_o,\vec{v}) = \int_0^\infty G(x,\vec{v}_o,\vec{v},t)\,dt \qquad (3\text{-}12)$$

$F(x,\vec{v}_o,\vec{v})|v_x|d^3v$ will be the total number of atoms that penetrate the plane x with a velocity $(\vec{v},d^3v)$ during the development of the collision cascade. From equation (3-11), we immediately get:

$$-\eta \frac{\partial}{\partial x} F(x,\vec{v}_o,\vec{v}) = N \int d\sigma [F(x,\vec{v}_o,\vec{v}) - F(x,\vec{v}',\vec{v}) - F(x,\vec{v}'',\vec{v})] \qquad (3\text{-}13)$$

This equation is rather comprehensive but is not easy to solve, since there are seven variables. According to equations (3-9) and (3-12), the sputtering coefficient follows from equation (3-13) by integration over $\vec{v}$, so that we can immediately get rid of the three variables t, v_x, and v. Introduce the function:

$$H(x,\vec{v}_o) = \int |v_x|\, d^3v\, F(x,\vec{v}_o,\vec{v}) \qquad (3\text{-}14)$$

where the integration over $\vec{v}$ obeys the following conditions:

$$\eta_o = \frac{v_x}{v_o} \leq 0 \tag{3-15}$$

$$E = \frac{1}{2} M_2 v_o^2 \geq U(\eta_o) \tag{3-16}$$

$U(\eta_o)$ is the surface binding energy that, in general, depends on the direction of ejection, characterized by the directional cosine η_o.

Equation (3-13) can now be written as:

$$-\eta \frac{\partial}{\partial x} H(x,\vec{v}_o) = N\int d\sigma[H(x,\vec{v}_o) - H(x,\vec{v}') - H(x,\vec{v}'')] \tag{3-17}$$

where $\vec{v}_o$, $\vec{v}'$, and $\vec{v}''$ may be expressed in terms of the energies E_1, E_1-E_2, and E_2, and the directional cosines η, η', and η'' of the incident ion, scattered ion, and recoiling atom, respectively.

The standard procedure for solving this type of equation is firstly to expand the angular dependence of H in terms of Legendre polynomials, $P_\ell(\eta)$:

$$H(x,E,\eta) = \sum_{\ell=0}^{\infty} (2\ell + 1)H_\ell(x,E)P_\ell(\eta) \tag{3-18}$$

Secondly, one introduces the moments:

$$H_\ell^{\,n}(E) = \int_{-\infty}^{\infty} x^n H_\ell(x,E)dx \tag{3-19}$$

Finally, using the scheme of Lindhard et al.[27], we can have the following equation, with separation of elastic from inelastic collisions:

$$n[\ell H_\ell^{\,n-1}(E) + (\ell+1)H_{\ell+1}^{\,n-1}(E)] = (2\ell+1)NS_e(E)\frac{d}{dE} H_\ell^n(E)$$
$$+ (2\ell+1)N\int_0^{\Lambda E} d\sigma(E,E_2)[H_\ell^n(E) - P_\ell(\cos\gamma')H_\ell^n(E-E_2) - P_\ell(\cos\gamma'')H_\ell^n(E_2)] \tag{3-20}$$

where γ' and γ'' are the laboratory scattering angles of scattered and recoil atoms (Figure 3-3), $S_e(E)$ is the electronic stopping cross section and $d\sigma(E,E_2)$ is the differential cross section for elastic scattering. The above equation can therefore be solved if we know the input quantities: $S_e(E)$, $d\sigma(E,E_2)$, and surface binding energy $U(n_o)$.

Considering only backward sputtering, the coefficient will be given by:

$$S_b(E) = H_o(x=0, E) \tag{3-21}$$

3.3.3 Analytical Solution

We are now going to specify the necessary input quantities and consider the analytical solution for backward sputtering coefficient.

Electronic Stopping Cross Section:

When the incident energy $E \lesssim Z_1^{4/3} M_1 .25\text{keV}$ we use Lindhard's expression[27]:

$$S_e(E) = -\frac{1}{N}\left(\frac{dE}{dx}\right)_e = KE^{1/2} \tag{3-22}$$

where K is a constant that depends on the atomic numbers Z_1, Z_2 and masses M_1, M_2 of ion and target.

Note that, in a reduced form, we have:

$$s_e(\varepsilon) = -\left(\frac{d\varepsilon}{d\rho}\right)_e = k\varepsilon^{1/2} \tag{3-23}$$

The constant k is of the order of 0.1 to 0.2 except for $Z_1 << Z_2$ where k can become larger than 1. Thus, for $\varepsilon \lesssim 1$ electronic stopping is usually a minor correction, unless $Z_1 \lesssim 10Z_2$, when it may not be neglected[50].

When the ion energy becomes extremely high, the electronic

stopping cross section can be approximated as:

$$S_e(E) = \frac{\text{constant}}{E} \qquad (3\text{-}24)$$

where the constant depends on Z_1, Z_2, M_1, and M_2.

Nuclear Stopping and Scattering Cross Section:

A standard procedure in solving equation (3-21) is to make a series development in powers of E_2 (provided $E_2 << E$) for the first-moment equation which is deduced from equation (3-20). In doing so, we shall arrive at the integration $\int_0^E E_2 d\sigma$. The nuclear stopping power is therefore needed.

A useful choice is the power approximation of the Thomas-Fermi-Firsov cross section, where, as mentioned in Section 2.2.4:

$$d\sigma = \frac{C dE_2}{E^m E_2^{1+m}}$$

Apart from the differential cross sections, we need the nuclear stopping powers, as defined in equation (2-43):

$$S_n(E) = \int_0^E E_2 d\sigma = \frac{C}{1-m} \Lambda^{1-m} E^{1-2m}$$

We can also compute $S_n(E)$ using Lindhard's expression[24], calculated by assuming Thomas-Fermi-Firsov interaction:

$$S_n(E) = \frac{4\pi Z_1 Z_2 e^2 a M_1}{M_1 + M_2} s_n(\varepsilon) \qquad (2\text{-}25)$$

where the reduced nuclear stopping cross section $s_n(\varepsilon)$ is the universal function tabulated by Lindhard et al.[24], and reproduced here in Table 3-1:

TABLE 3-1

Reduced Nuclear Stopping Cross Section $s_n(\varepsilon)$ for Thomas-Fermi-Firsov Interaction (after Lindhard et al.[24]).

ε	$s_n(\varepsilon)$
0.002	0.120
0.004	0.154
0.01	0.211
0.02	0.261
0.04	0.311
0.10	0.372
0.15	0.393
0.20	0.403
0.40	0.405
1.0	0.356
2.0	0.291
4.0	0.214
10.0	0.128
20.0	0.0813
40.0	0.0493

Surface Binding Energy:

Sigmund assumed that the most realistic expression for $U(n_o)$ is:

$$U(n_o) = U_o/n_o^2 \qquad (3\text{-}26)$$

with U_o equal to the measured sublimation energy. Equation (3-26) is obtained from the planar potential barrier or work-function model.

With the preceding quantities, equation (3-20) can be solved. Sigmund[9] obtained the following analytical solution:

$$S_b(E) = 0.0420 \frac{\alpha S_n(E)}{U_o} \qquad (3\text{-}27)$$

for the coefficient of backward sputtering of a random target under normal incidence of keV heavy or medium-mass ions.

α is a factor that depends, in the elastic collision region, on M_2/M_1, as illustrated in Figure 3-4.

Sigmund's theory therefore does not require a computer. The sputtering coefficients over a wide range of ion energies can be rather quickly calculated, with the aid of a graph and a table.

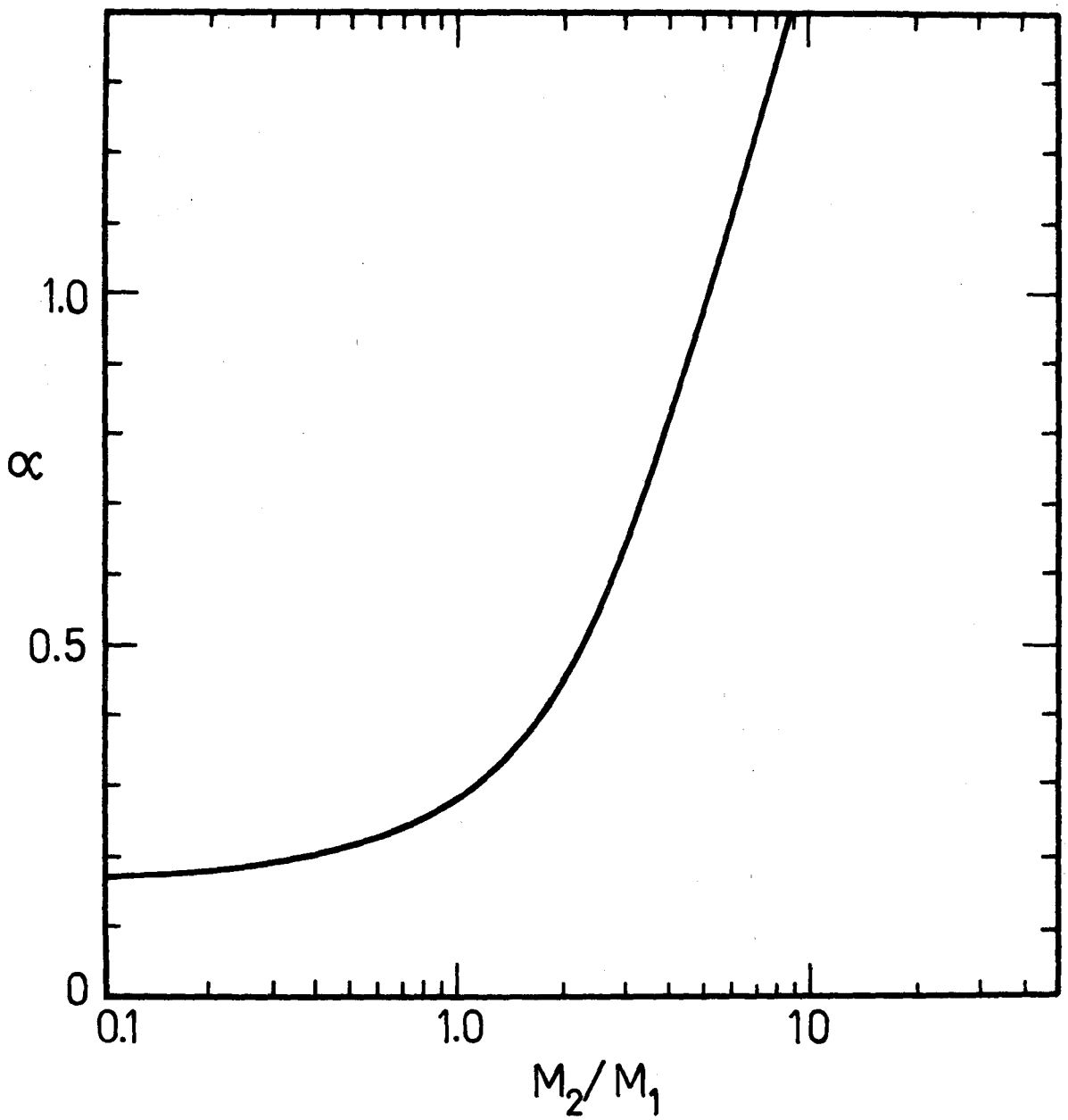

Figure 3-4 Variation of α with mass ratio in the elastic collision region (after Sigmund[9])

CHAPTER 4

DEPTH DISTRIBUTIONS OF IONS AND DAMAGE

4.1 INTRODUCTION

An energetic ion entering a target will, through collisions with nuclei and electrons of the lattice, lose its energy, slow down, and finally come to rest. The total distance that the ion has travelled in coming to rest is called its range, denoted by R. Because the number of collisions and the energy transferred in each collision are random variables , all ions of a given type with given initial conditions will not have the same range. Rather, the ions will form a distribution which must be characterized by quoting an ion mean range, $\langle R \rangle$, a standard deviation in ion range, $\langle \Delta R \rangle$, and perhaps higher moments of the distribution function, $\langle R^m \rangle$. Another interesting quantity is the projection of the range on the direction of incidence, that is,the projected range, R_p. These quantities are defined in Figure 4.1.

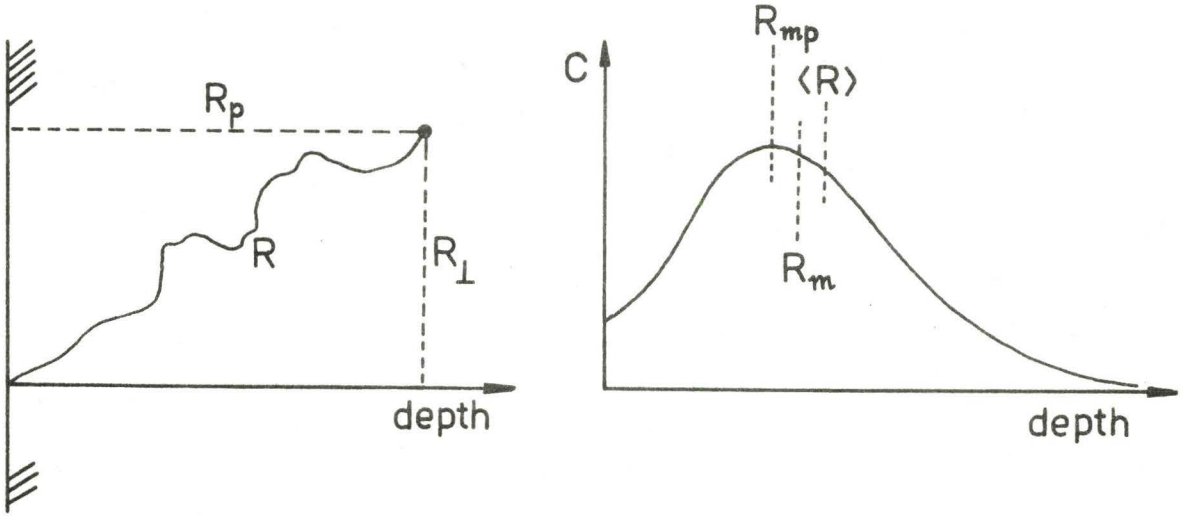

Figure 4-1 Definition of ranges.

tely from the theories of Lindhard et al.[27] and of Winterbon, Sigmund, and Sanders[25]. In the former of these both electronic and nuclear stoppings are taken into account while in the latter the comparatively simple case of a heavy ion or atom slowing down by elastic collisions is considered. The distribution profiles of ions and damage follow from the ranges by using the Edgeworth expansion[49,51-52]. We shall review these important theories in the following sections.

4.2 PENETRATION THEORY OF LINDHARD ET AL.

4.2.1 Energy Loss Mechanisms:

The distance travelled by a particle in a solid before coming to rest, can in principal be directly estimated from the rate of energy loss. Two physical mechanisms are responsible for most of the energy loss of ions: (1) nuclear stopping due to elastic collisions of the ion with the nuclei of the substrate and (2) electronic stopping due to inelastic interactions between the ion and electrons in the solid. The nuclear stopping accounts for part of the energy transfer, and essentially all of the angular scattering, whereas the electronic stopping appears much as a viscous damping effect and does not cause appreciable angular deviations. To a good approximation, the two mechanisms may be treated as independent events. Recently, they have been developed into a comprehensive unified theory of atomic stopping by Lindhard and his collaborators [27] (referred to as LSS).

By using a differential scattering cross section based on a TFF potential (equation (2-8)) between the atoms, LSS derived a universal relationship for nuclear stopping, $(-d\varepsilon/d\rho)_n$, in terms of reduced parameters, ε and ρ, as already mentioned in Section 2.2.4:

$$\varepsilon = \frac{EaM_2}{Z_1 Z_2 e^2 (M_1 + M_2)}$$

$$\rho = RN4\pi a^2 \frac{M_1 M_2}{(M_1 + M_2)^2}$$

To obtain the stopping contribution due to electronic collisions, LSS have derived a velocity-proportional electronic stopping power, $(-d\varepsilon/d\rho)_e$, given by:

$$s_e(\varepsilon) = \left(-\frac{d\varepsilon}{d\rho}\right)_e = k\varepsilon^{1/2} \qquad (4\text{-}1)$$

where

$$k = \frac{\xi_e \; 0.0793 \; Z_1^{1/2} Z_2^{1/2} (M_1+M_2)^{3/2}}{(Z_1^{2/3}+Z_2^{2/3})^{3/4} \; M_1^{3/2} \; M_2^{1/2}} \qquad (4\text{-}2)$$

with

$$\xi_e \simeq Z_1^{1/6}$$

The electronic-stopping calculations therefore do not give a universal $(-d\varepsilon/d\rho)_e$ curve, but rather a set of curves each characterized by a particular value of k which depends on ion-target combinations.

$(-d\varepsilon/d\rho)_n$ and $(-d\varepsilon/d\rho)_e$ are plotted in Figure 4-2. We see that nuclear stopping is the more important process at low energies, that it reaches a maximum value around $\varepsilon = 0.35$, and then falls off. Electronic stopping, on the other hand, increases linearly with energy over a wide range, passes through a maximum, and subsequently falls off as ε^{-1}. The quantity $(-d\varepsilon/d\rho)_e$ therefore becomes the dominant process at very high energies ($\varepsilon > 2$).

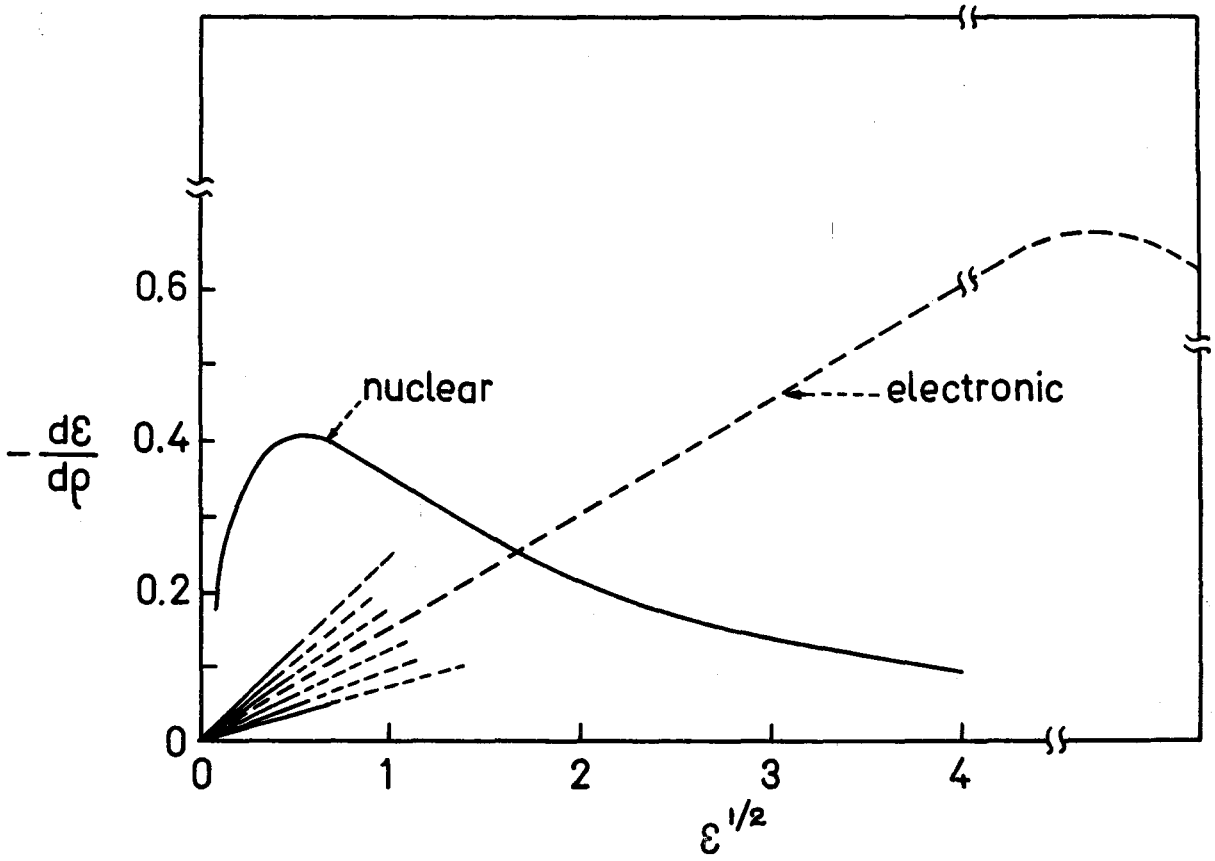

Figure 4-2 Theoretical nuclear and electronic stopping-power curves (based on Lindhard et al.[27])

4.2.2 Approximate Range-Energy Relationship

To a first approximation, the range measured along the ion path is related to the total stopping power by the relation:

$$\langle R \rangle = \int_0^E \frac{dE}{\left(-\frac{dE}{dx}\right)_n + \left(-\frac{dE}{dx}\right)_e} \tag{4-3}$$

or in a reduced form:

$$\rho = \int_0^\varepsilon \frac{d\varepsilon}{\left(-\frac{d\varepsilon}{d\rho}\right)_n + \left(-\frac{d\varepsilon}{d\rho}\right)_e} \tag{4-4}$$

At low energies, the nuclear stopping is dominant, and the ion range will therefore be:

$$\langle R \rangle = \int_0^E \frac{dE}{(-\frac{dE}{dx})_n} = \int_0^E \frac{dE}{NS_n(E)} \tag{4-5}$$

For power-law scattering, $S_n(E)$ is given by equation (2-43), namely:

$$S_n(E) = \frac{C}{1-m} \Lambda^{1-m} E^{1-2m}$$

and it follows that:

$$\langle R \rangle = \frac{(1-m) E^{2m}}{2mC\Lambda^{1-m}N} \tag{4-6}$$

or

$$\rho = \frac{1-m}{m} \cdot \frac{\varepsilon^{2m}}{\lambda_m} \tag{4-7}$$

For the case of an inverse square potential, m = 1/2 and $\lambda_{1/2}$ = 0.327 (Section 2.1.8), we have:

$$\rho = 3.06\ \varepsilon \tag{4-8}$$

This equation is Nielsen's formula of range-along-path which can be used in the energy region where elastic collisions are dominant.

At very high energies, the nuclear stopping becomes negligible compared with the electronic stopping power (Figure 4-2). The range equation is then approximately written as:

$$\langle R \rangle = \int_0^E \frac{dE}{(-\frac{dE}{dx})_e} = \int_0^E \frac{dE}{NS_e(E)} \tag{4-9}$$

From equation (3-22), <R> follows immediately:

$$\langle R \rangle = \frac{2E^{1/2}}{K} \tag{4-10}$$

or in a reduced form:

$$\rho = \frac{2\varepsilon^{1/2}}{k} \tag{4-11}$$

When both nuclear and electronic stoppings are simultaneously taken into account, or when a TFF potential is used, the general equation (4-3) or (4-4) must be considered. The resulting ρ versus ε relationship is shown in Figure 4-3. The curve marked "Th-F" shows the limiting case where the electronic stopping has been neglected. The inclusion of a relatively large electronic stopping term into $\rho = \rho(\varepsilon, k)$ is shown by the curve marked "k = 0.4". Nielsen's formula (equation (4-8)), which corresponds to the inverse square potential, is also included for comparison.

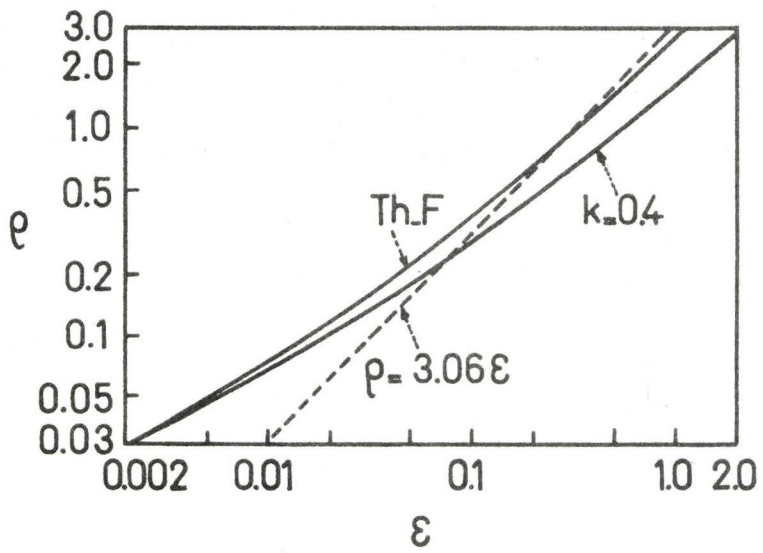

Figure 4-3 Theoretical range-energy relationship for $\varepsilon < 2$ (after Lindhard et al.[27])

4.2.3 Exact Integral Equation for the Projected Range

In most experiments in ion bombardment, it is the penetration depth measured along the normal of the surface that is of interest. This distance is the projected range R_p defined in Section 4.1.

In deriving projected range statistics, we have to consider the angular deviations of the impinging particle as well as its energy loss. Again, the projected range theory of Lindhard et al.[27] will be discussed here. The basic approach taken was to write an integral equation describing the conditional probability $p(E,R_p)\delta R_p$ that a particle with initial energy E entering a target would have a projected range between $R_p-\delta R_p$ and R_p:

$p(E,R_p)$ = (probability of creation of a scattered particle at $R_p-\delta R_p$ with $E-E_2$) + (Probability of appearance of a non-colliding particle at $R_p-\delta R_p$ with E)

$$= N\,\delta R \int_{E_2=0}^{\Lambda E} d\sigma\; p(E-E_2,\, R-\delta R)\cos\gamma + (1-N\,\delta R \int_{E_2=0}^{\Lambda E} d\sigma)\,p(E,R_p-\delta R_p) \qquad (4\text{-}12)$$

where γ = scattering angle in L-coordinates,

and E_2 = energy lost in nuclear and electronic stopping in a single collision.

In the limit of $\delta R \to 0$:

$$\frac{\partial p(E,R_p)}{\partial R_p} = N\int_0^{\Lambda E} d\sigma[p(E-E_2,R)\cos\gamma - p(E,R_p)] \qquad (4\text{-}13)$$

The solution of this equation has been described by Schiøtt, in Appendix of his article[52], using the $\langle R^m\rangle$-moment concept of LSS[27]:

$$m\langle R_p^{m-1}\rangle = N\int_0^{\Lambda E} d\sigma[\langle R_p^{m}\rangle - \langle R_p^{m}(E-E_2)\rangle \cos\gamma] \qquad (4\text{-}14)$$

where m is the order of the moment. By means of this equation we may successively derive the first, second, etc., moments of the projected range.

For m = 1, for example, equation (4-14) yields:

$$1 = N\int_0^{\Lambda E} d\sigma[\langle R_p\rangle - \langle R_p(E-E_2)\rangle \cos\gamma] \qquad (4\text{-}15)$$

By assuming that $E_2 << \Lambda E$ we can introduce the dependence upon E_2 by a series expansion of the function in powers of E_2. The simplest case utilized only the first order term. Equation (4-15) now becomes:

$$1 = \frac{\langle R_p\rangle}{\lambda_{tr}} + \frac{d\langle R_p\rangle}{dE}\cdot NS_{tr} \qquad (4\text{-}16)$$

where λ_{tr} is the transport mean free path, given by:

$$\frac{1}{\lambda_{tr}} = N\int_0^{\Lambda E} d\sigma\,(1-\cos\gamma) \qquad (4\text{-}17)$$

and S_{tr} is a transport stopping cross section, defined as:

$$S_{tr} = \int_0^{\Lambda E} d\sigma\,(E_2\cos\gamma) \qquad (4\text{-}18)$$

with $$\cos\gamma = \left(1 - \frac{1 + M_2/M_1}{2}\cdot\frac{E_{2(n)}}{E}\right)\left(1 - \frac{E_{2(n)}}{E}\right)^{-1/2} \qquad (4\text{-}19)$$

where $E_{2(n)}$ is the energy lost only to the nucleus.

The solution of equation (4-16) is written as follows[52]:

$$\langle R_p\rangle = \int_0^{E} \frac{dE'}{NS_{tr}(E')}\exp\left[\int_E^{E'} \frac{dE''}{\lambda_{tr}(E'')\,NS_{tr}(E'')}\right] \qquad (4\text{-}20)$$

Values of projected range $\langle R_p \rangle$ and projected standard deviation $\langle \Delta R_p \rangle$ for a wide variety of ion-target combinations have recently been tabulated by Schiøtt[53] at the University of Aarhus (Denmark).

In the energy region where nuclear stopping dominates and for $M_1 > M_2$, the expression of LSS[27]:

$$\frac{\langle R \rangle}{\langle R_p \rangle} = 1 + \frac{M_2}{3M_1} \tag{4-21}$$

is a fair approximation. This relation is actually derived for power-law scattering with m = 1/2.

4.2.4 Range Straggling

In ion-bombardment studies, we are interested in the entire depth distribution, and therefore need to know something about the range straggling. In a random target, the range distribution is approximately Gaussian in shape, and so requires at least one extra parameter, namely, the standard deviation ΔR_p in projected range. Again, LSS[27] have developed a useful theoretical framework for treating this problem.

Provided $M_1 > M_2$, the difference between $\frac{\langle \Delta R \rangle}{\langle R \rangle}$ and $\frac{\langle \Delta R_p \rangle}{\langle R_p \rangle}$ is quite small. In such cases, and for $\varepsilon < 3$, LSS find that the predicted range straggling, expressed in terms of the reduced parameter:

$$\frac{\langle \Delta R_p \rangle}{\langle R_p \rangle} \cdot \frac{(M_1 + M_2)}{2(M_1 M_2)^{1/2}}$$

approaches an almost constant value of 0.35.

Range straggling can readily be estimated from recent tabulations by Schiøtt[53].

The large values of $\frac{\langle \Delta R_p \rangle}{\langle R_p \rangle}$ for light ions might be anticipated from the fact that $\langle R_p \rangle$ is now much smaller than $\langle R \rangle$. The decrease in

$\frac{<\Delta R_p>}{<R_p>}$ with increasing energy is due to the increased contribution of electronic stopping.

4.3 THEORETICAL ANALYSES OF SPATIAL DISTRIBUTION OF ENERGY DEPOSITED INTO ATOMIC COLLISIONS

4.3.1 General

As the incident ions lose their energy in penetrating the solid they transfer energy to electrons and atoms of the target, resulting in atomic motion or displacement. The structural damage will depend on the energy which ultimately resides in the atomic processes, regardless of the measurement chosen to quantify the damage. For example, the theoretical depth distribution of vacancy production, which was calculated by Pavlov et al.[54] using a Monte Carlo technique, has been shown to be proportional to the depth distribution of energy deposited into atomic processes for 60-keV B^+ incident on Si, calculated by Brice[55]. Similarly, the total neutron damage in Si, as measured by carrier removal has been shown experimentally to be proportional to the total energy deposited into atomic processes[56]. Even the depth distribution of more complex forms of damage such as small point-defect clusters has also been shown to be comparable to the distribution of energy deposited into atomic processes for 400-keV O^+ incident on Si[55,57-58]. The deposited energy is therefore a basic quantity which is accessible to precise quantification and which correlates well with other experimental and theoretical measures of damage in a solid.

Sigmund and Sanders[28] have presented an integro-differential equation which governs the spatial distribution of energy deposited by atomic particles in elastic collisions with a random solid, using a power law approximation to the TFF potential. A minimum number of assumptions have been incorporated into this equation and its solution therefore represents the most accurate estimate of the spatial distribution of damage available to us at the present time. Recent work of Sigmund and his colleagues is based on the TFF potential; however, there is no result published yet. Likewise, the work of Brice is less rigorous than that of Sigmund and Sanders.

In the following paragraphs, we are going to have a look on these important theoretical treatments of the spatial distribution of deposited energy: Brice's theory and theory of Sigmund and Sanders.

4.3.2 Brice's Theory

Brice[55,59] analysed the damage process using a method which consists of two steps. First, he determined the spatial distribution of the ions in the target as they slow down and come to rest. That is, he determined the spatial distribution of the ions at energies E', intermediate between the initial energy E and the final energy 0. Then, from the ion locations, a knowledge of the interaction cross section, and the experimentally measured values of the partition of the transferred energy into electronic and nuclear processes, he calculated the initial spatial distribution of the energy deposited into atomic processes. If the energy transport through the recoil of struck target atoms is neglected (i.e. the deposited energy does not move), and the effects of radiation -enhanced diffusion, annealing, and saturation are negligible, then

the resultant spatial distribution is the final spatial distribution of damage in the solid.

We define the functions:

$P_3(E,E',r)\ d^3r$ = probability that an incident ion with initial energy E on a random target will be found in the volume element d^3r about r when its energy is E'.

and

$$P_1(E,E',x) = \int_{-\infty}^{\infty}\int_{-\infty}^{\infty} P_3(E,E',r)\ dy\ dz \qquad (4\text{-}22)$$

where x represents a coordinate parallel to the initial direction of motion of the incident ion, and y and z are orthogonal axes perpendicular to x.

Let the incident ions and target atoms interact with some energy dependent cross section $d\sigma_q$ to produce some quantity of interest Q, of which the average amount produced in d^3r is then given by $d^3\overline{Q}$:

$d^3\overline{Q}$ = (probability of the appearance of a particle at r with E') X (number of target atoms in 1x1x$d\overline{R}$) X (energy loss per target atom over unit distance).

$$= \int_0^E [P_3(E,E',r)d^3r\{\frac{d\overline{R}}{dE'}\} NS_n(E)]\ dE' \qquad (4\text{-}23)$$

where $d\overline{R}$ is the average distance moved by an ion of energy E' in loosing dE'. Since d^3r is not a function of the energy E', it can be carried outside the integration to yield $\frac{d^3\overline{Q}}{d^3r}$, the spatial distribution of the produc-

tion of $\overline{Q}$. The depth distribution of $\overline{Q}$ is therefore determined as:

$$\frac{d\overline{Q}}{dx} = \int_0^E [P_1(E,E',x)\{\frac{d\overline{R}}{dE'}\}NS_n(E)]\, dE' \qquad (4\text{-}24)$$

In order to evaluate $d^3\overline{Q}/d^3r$ or $d\overline{Q}/dx$ in equations (4-23) and (4-24), one must determine the distribution functions $P_3(E,E',r)$ or $P_1(E,E',x)$. In the Gaussian approximation, Brice obtained:

$$P_1(E,E',x) = (2\pi<\Delta R_p>^2)^{-1/2} \exp[-(x-<R_p>)^2/2<\Delta R_p>^2] \qquad (4\text{-}25)$$

and

$$P_3(E,E',r) = \frac{P_1(E,E',x)}{\pi<\Delta R_\perp>^2} \exp\,[-(y^2+z^2)/<\Delta R_\perp>^2] \qquad (4\text{-}26)$$

where R_p and $R_\perp$ are already defined in Figure 4-1.

In our specific applications, the quantity Q represents the energy deposited into atomic processes. Since it is not convenient to illustrate the depth-distribution profiles for more than a few different incident energies, Brice[59] presented the results in form of graphs, in which the contours of constant damage density, dQ/dx, are plotted as functions of incident energy, E, and penetration depth into the solid, x. Damage depth-distribution profiles can therefore be constructed for any incident energy by plotting the contour values, corresponding to that energy, as a function of penetration distance.

Comparison of calculations by Brice's method with exact numerical solution for the moments of the damage distribution show that Brice's theory is only valid for incident ion energies in the range corresponding to the dimensionless energy ε being greater than perhaps three.

4.3.3 Theory of Sigmund and Sanders

As we have seen in the preceding sections, the distribution of ion ranges in a random medium is determined by an integro-differential equation of the transport type. The same is true for the distribution of deposited energy. Integral equations have therefore been used by Sigmund and Sanders[28] to describe the spatial distribution of structural damage in a bombarded medium.

Thus, we define the function:

$f(\vec{r},\vec{v}_o)d^3r$ = average amount of energy deposited in nuclear motion by a foreign projectile and recoil atoms in the volume element $(\vec{r},d^3r)$ at the end of the slowing down process.

The normalizing condition will therefore be:

$$\int f(\vec{r},\vec{v}_o)d^3r = \nu(E) \qquad (4\text{-}27)$$

where $\nu(E)$ is the amount of energy spent in nuclear motion. The function $f(\vec{r},\vec{v}_o)$ must satisfy the integral equation, which is similar to equation (3-13). In order to calculate spatial averages over the distribution function, $f(\vec{r},\vec{v}_o)$ is expanded in terms of Legendre polynomials. Furthermore, by introducing moments and using power-law approximation, Sigmund and Sanders obtained results for the first, second, and third order moments of the range and damage distributions (see Tables 1a-2d of reference 28). Recently, Winterbon, Sigmund, and Sanders[25] have put their results, obtained by computer instead of by desk calculator, in form of graphs up to fourth order moments. Figures 4-4a-c are reproduced from reference 25 for future use, in Chapter 9. These figures show the variation

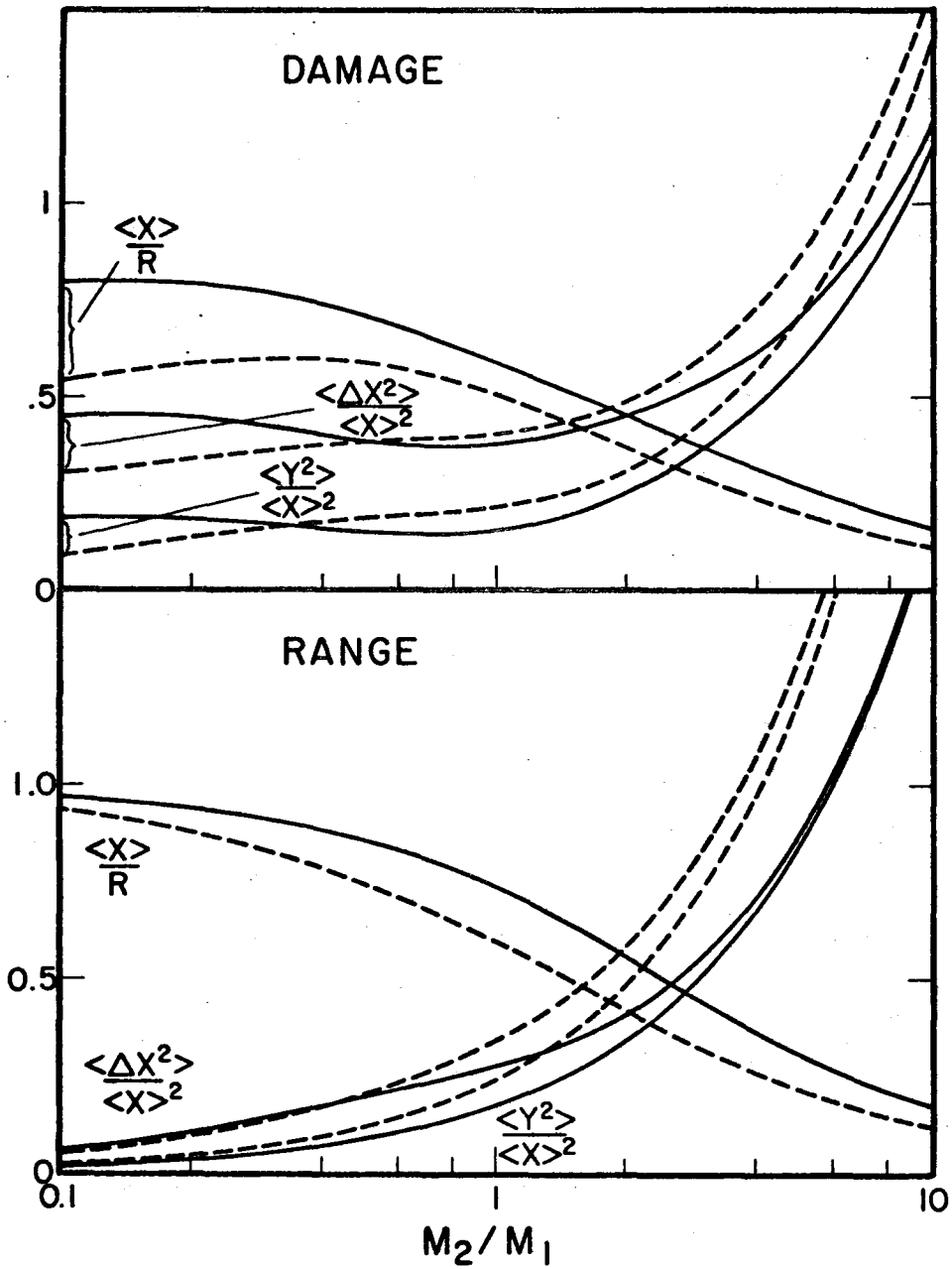
DAMAGE
1
.5
0
$\frac{\langle X \rangle}{R}$
$\frac{\langle \Delta X^2 \rangle}{\langle X \rangle^2}$
$\frac{\langle Y^2 \rangle}{\langle X \rangle^2}$
RANGE
1.0
0.5
0
$\frac{\langle X \rangle}{R}$
$\frac{\langle \Delta X^2 \rangle}{\langle X \rangle^2}$
$\frac{\langle Y^2 \rangle}{\langle X \rangle^2}$
0.1
1
10
M_2 / M_1

(a)

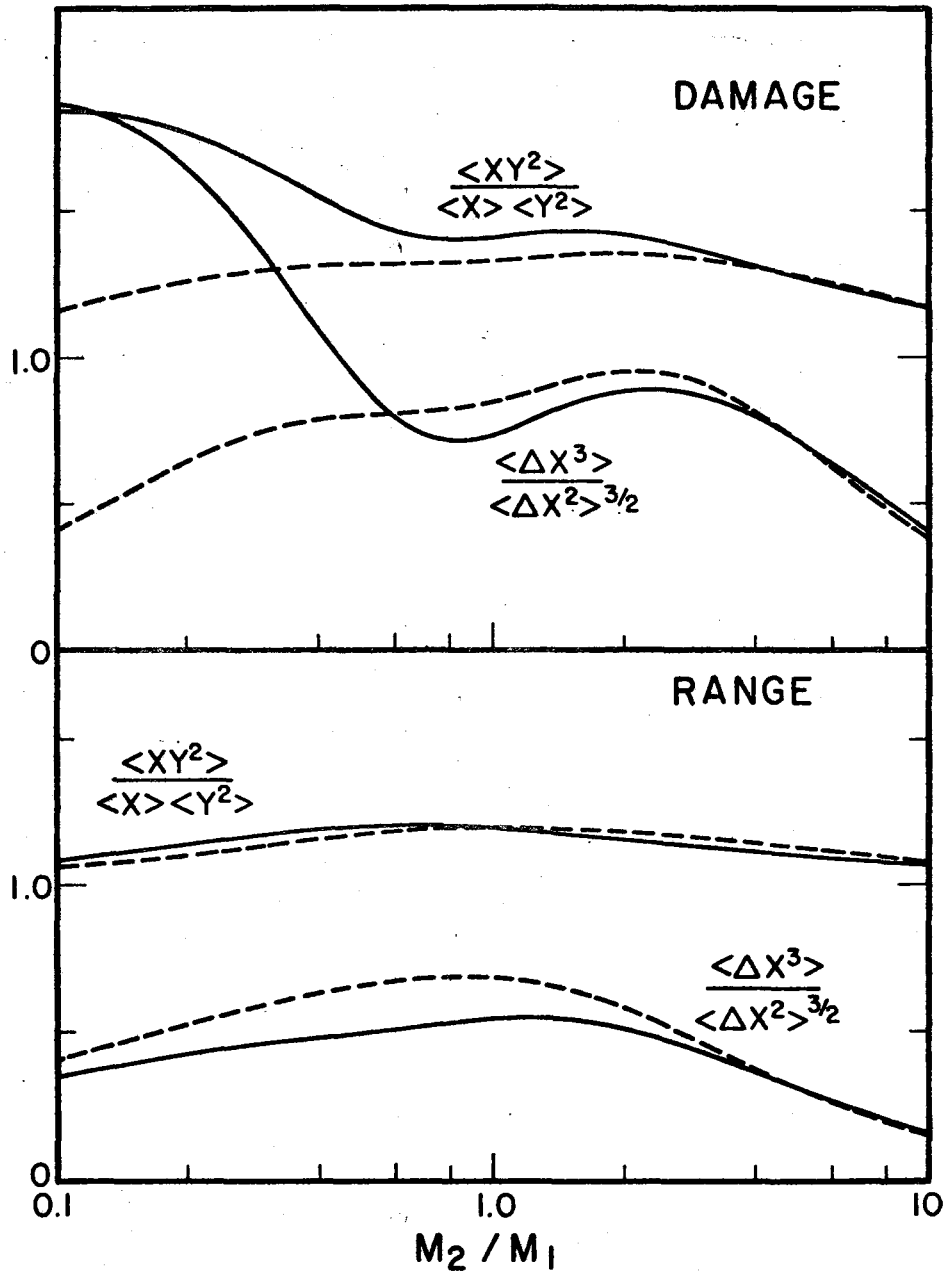
DAMAGE
$\frac{\langle XY^2 \rangle}{\langle X \rangle \langle Y^2 \rangle}$
1.0
0
$\frac{\langle \Delta X^3 \rangle}{\langle \Delta X^2 \rangle^{3/2}}$
RANGE
$\frac{\langle XY^2 \rangle}{\langle X \rangle \langle Y^2 \rangle}$
1.0
0
$\frac{\langle \Delta X^3 \rangle}{\langle \Delta X^2 \rangle^{3/2}}$
0.1
1.0
10
M_2 / M_1

(b)

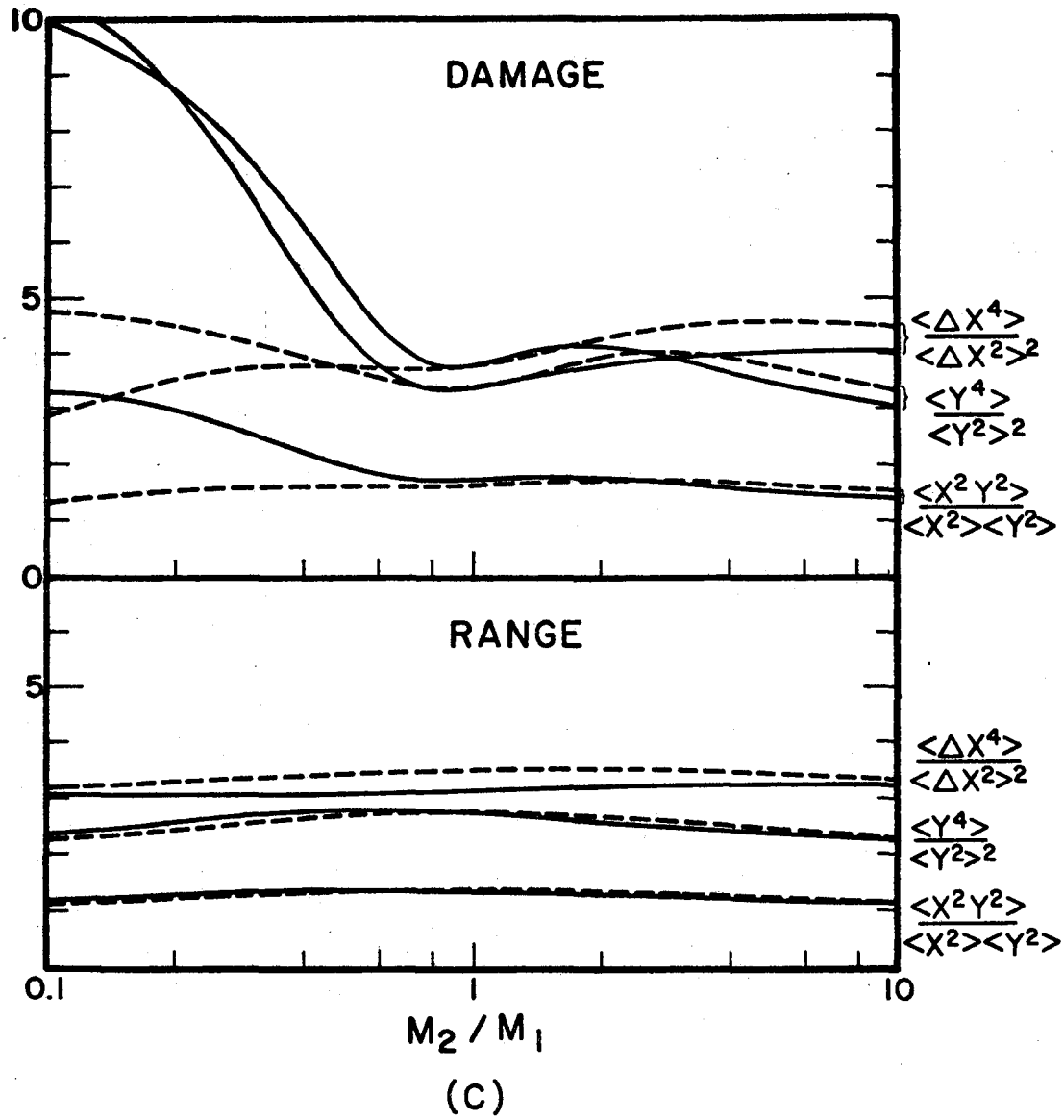

Figure 4-4 First, second, third, and fourth order averages over damage and range distributions. Dashed line: m = 1/3; solid line: m = 1/2 (after Winterbon, Sigmund, and Sanders[25])

of first, second, third, and fourth order averages over damage and range distributions as functions of mass ratio M_2/M_1. Note that $\langle y^2 \rangle = \langle z^2 \rangle$, where y and z are coordinates perpendicular to the incoming direction, and $R = \int_0^E dE/NS_n(E) = (1-m)E^{2m}/2mC\Lambda^{1-m}N$, equation (4-6), is the approximate path length of the travelling ion.

Figures 4-5a and b, which are also taken from reference 25, show the comparison of range moments with the corresponding damage moments. In Figure 4-5a, we see that the mean damage depth is consistently smaller than the mean projected range. The difference is small except for $M_2/M_1 \ll 1$ and $m = \frac{1}{3}$, i.e. low energies. This is a consequence of the fact that for $M_1 \gg M_2$ the incident-particle track is relatively straight, the range straggling is small, and therefore the ion comes to rest essentially at the far end of the damage clound. For light ions ($M_1 < M_2$), large-angle scattering of the primary beam can occur, and so both the defect and range distributions averaged for many ions, are comparable in shape. Figure 4-5b shows that the damage distribution is much broader than the range distribution for $M_2 \ll M_1$, and the opposite is true for $M_2 \gtrsim M_1$. In the last case, the ion undergoes large deflections, but mainly those in the beginning, where the ion still has much energy to share with its collision partners, determine the region where the energy is located, while those collisions undergone by the ion toward the end of its slowing down still may contribute to range straggling, but not to a broadening of the damage distribution.

4.3.4 Use of the Edgeworth Expansion

In a random target, the distribution profiles of ions and damage

(a)

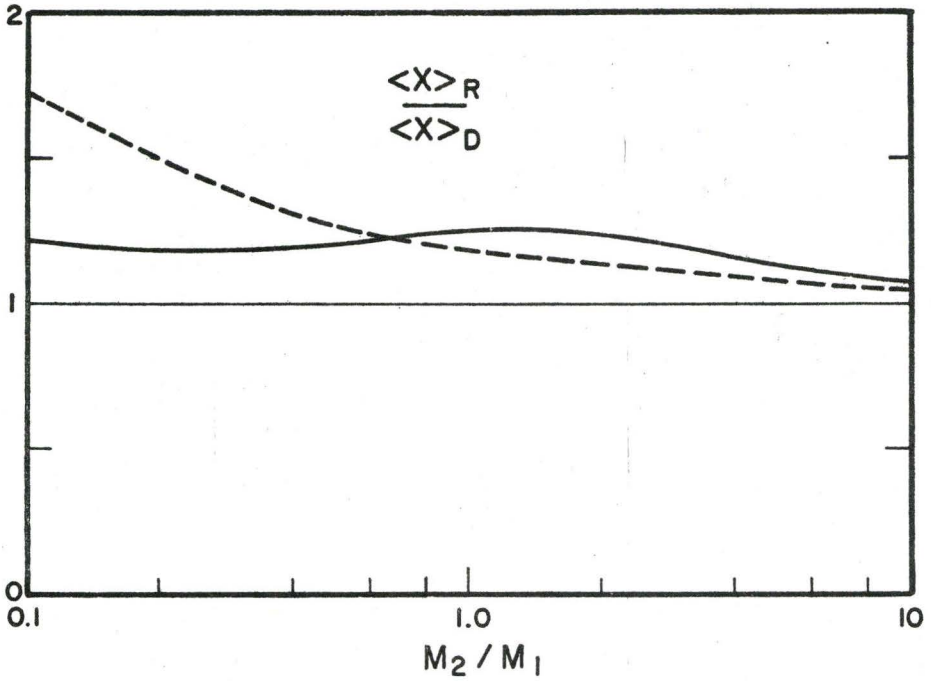

(b)

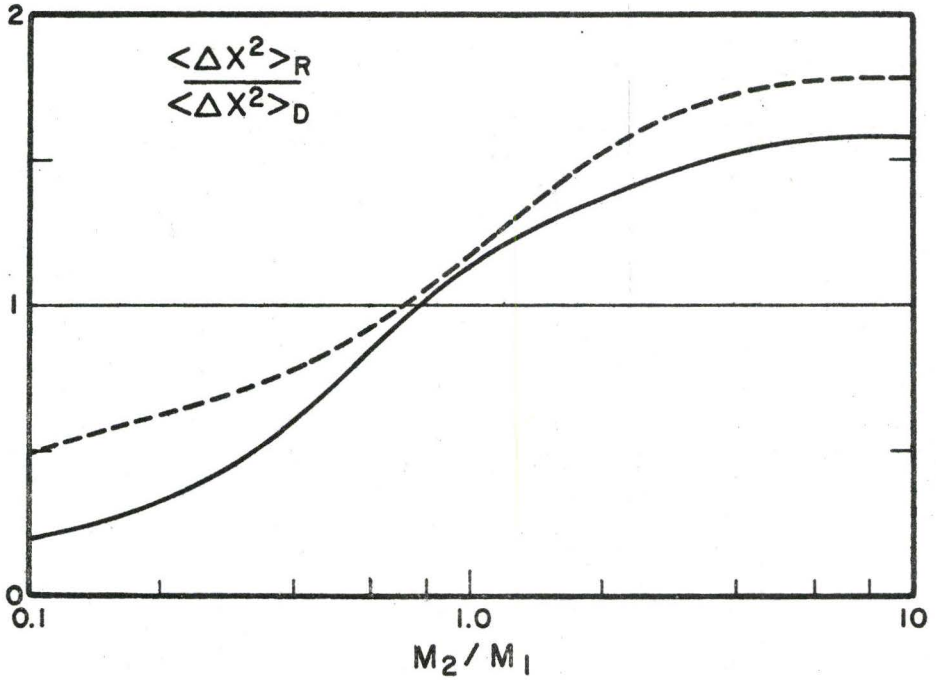

Figure 4-5 Ratio between averages over range and damage distributions. Dashed line: m = 1/3; solid line: m = 1/2 (after Winterbon, Sigmund, and Sanders[25])

are similar to a Gaussian. Therefore, one can approximate the distribution function by the Edgeworth expansion[49-51] in terms of spatial moments:

$$F(x) = (2\pi\mu_2)^{-1/2} \exp(-\xi^2/2)\, f(\xi) \qquad (4\text{-}29)$$

with $$f(\xi) \simeq 1-(1/6)(\mu_3/\mu_2^{3/2})(3\xi - \xi^3) + (1/24)(\mu_4/\mu_2^2-3)(3-6\xi^2 + \xi^4) - (1/72)(\mu_3^2/\mu_2^3)(15-45\xi^2 + 15\xi^4 - \xi^6)$$

where $$\mu_n = \langle \Delta x^n \rangle = \langle (x-\langle x \rangle)^n \rangle$$

and $$\xi = (x - \langle x \rangle)/\mu_2^{1/2}$$

If only the first term of $f(\xi)$ is taken into account one has a simple Gaussian with the width $\mu_2^{1/2}$, centered around $x = \langle x \rangle$. The second term introduced the "skewness", and the third one gives the "excess" of the distribution.

For our specific applications, x is the penetration depth, $\langle x \rangle$ represents $\langle R_i \rangle = \langle R_p \rangle$ or $\langle R_d \rangle$, and $\mu_2^{1/2}$ is $\langle \Delta R_i \rangle = \langle \Delta R_p \rangle$ or $\langle \Delta R_d \rangle$ of ions and damage. These values including values of μ_3 and μ_4, can be obtained from Figure 4-4.

CHAPTER 5

DIFFUSION IN ION-IMPLANTED SOLIDS *

5.1 INTRODUCTION

With most types of diffusion in solids, the behaviour is classed very simply as either intrinsic or extrinsic. Intrinsic behaviour is said to arise when the point defects, or other means giving rise to the diffusion, exist in their equilibrium concentrations, while extrinsic behaviour involves the point defects, or other diffusion carriers, being present in excess owing to such factors as radiation damage, doping, quenching, or cold work. The study of implanted-atom diffusion has confirmed the general view that both intrinsic and extrinsic processes occur, though it has led to the recognition of a much wider role for the latter. One reason for this is that the introduction of foreign atoms into a solid by implantation necessitates a violent technique such as ion bombardment or nuclear reaction and excess defects due to radiation damage are unavoidable. This should not be interpreted, however, to mean that the phenomena found will be more complex than normal . In fact, the connection between excess defects of all types and implanted-atom diffusion is such as to make the experimental results sometimes easier to interpret than in other work on, for example, inert-gas diffusion since, by suitable choice of bombardment energy and dose, it is possible to vary

---

* This Chapter is largely based on the publication by R. Kelly and the author[12].

almost at will the roles played by unperturbed diffusion, damage, trapping, and bubbles. (Effects due to pre-existing dislocations, grain-boundaries, and cracks are normally negligible due to the short diffusion distances.) The motion of implanted atoms in ion-bombarded solids has been proposed as a solid-state probe for defects.

We are now going to discuss two cases of diffusion in ion-implanted solids: diffusion with uniform parameters and diffusion with non-uniform parameters.

5.2 DIFFUSION WITH UNIFORM DIFFUSION PARAMETERS

Diffusion in ion-implanted targets is a relatively simple process to treat when the diffusion parameters are uniform. Many authors have shown that there is no difficulty in obtaining solutions for normal diffusion with a constant diffusion coefficient[60,61], for diffusion in the presence of permanent traps with uniform spacing[60,62], or even for diffusion in the presence of reversible traps provided both the spacing and trap depth are uniform [62,63]. A characteristic feature of diffusion with uniform diffusion parameters is found to be what might be called the "rotation effect", such that a diffusion profile will, as a result of the target being heated after implantation, seemingly rotate about the original position, as illustrated in Figure 5-1.

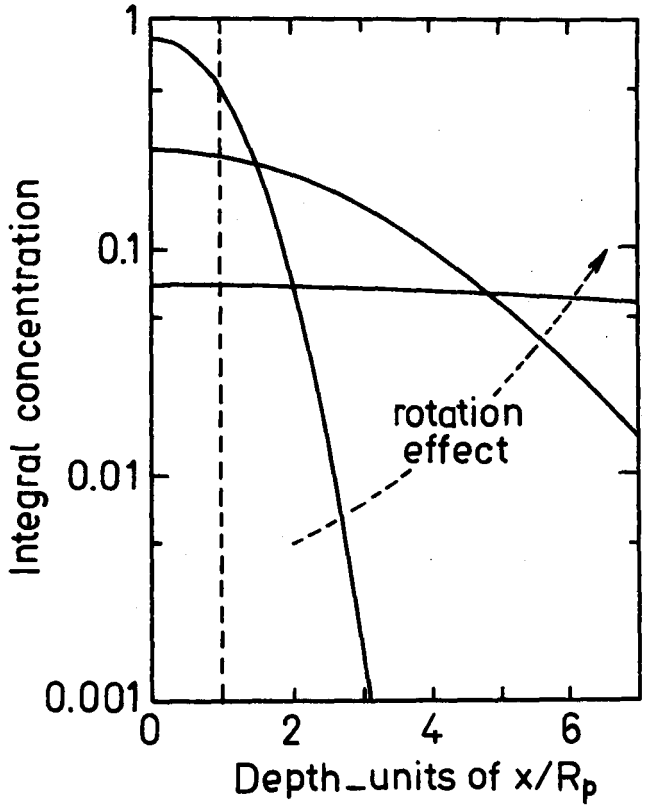

Figure 5-1 Rotation effect in diffusion with uniform parameters.

5.2.1 Diffusion with a Constant D

For most types of impurity or self-diffusion, the usual diffusion equation is adequate:

$$\frac{\partial C_1}{\partial t} = D\frac{\partial^2 C_1}{\partial x^2} \qquad (5\text{-}1)$$

where C_1 (in fractional units) is the concentration in the absence of trapping, and D is a constant diffusion coefficient.

In a random target, where the ion distribution is generally compact due to the absence of channelling, the diffusing material is con-

centrated in the vicinity of R_p, the most probable range, or R_m, the median range ($R_p = R_m$ for this case), and the use of the plane source is allowed. The integral-concentration solution for a plane source at $x = R_p$ in a semi-infinite medium is given by[60]:

$$C_1^{int} = \int_x^\infty C_1^{diff}\, dx = \frac{1}{2}\{\text{erf}\frac{R_p+x}{2(Dt)^{1/2}} + \text{erf}\frac{R_p-x}{2(Dt)^{1/2}}\} \qquad (5\text{-}2)$$

This solution gives results as in Figure 5-1. Experimental examples of the rotation effect have been reported by Kelly and Ruedl[64], and by Matzke[65].

5.2.2 Diffusion in the Presence of Permanent Traps with Uniform Spacing

When permanent trapping is considered, the motion of diffusing species becomes complicated and the modified diffusion equations are required. The mathematical consequences of trapping have been discussed by Hurst[62] and Gaus[63]. For the particular case of true diffusion where only permanent trapping is important, the proposed equations were[60]:

$$\frac{\partial C_2}{\partial t} = D\frac{\partial^2 C_2}{\partial x^2} - \frac{DC_2}{L^2} \qquad (5\text{-}3a)$$

$$\frac{\partial m}{\partial t} = \frac{DC_2}{L^2} \qquad (5\text{-}3b)$$

where C_2 is the concentration in the presence of permanent trapping, m (in fractional units) is the trapped concentration, and L is the trapping length.

The concentration expressions for diffusion of a plane source at $x = R_p$ have been obtained by Kelly and Matzke[60]:

$$C_2^{int} = \exp(-Dt/L^2)\, C_1^{int} \tag{5-4}$$

and

$$m_\infty^{int} = (D/L^2)\int_0^\infty C_2^{int} dt \tag{5-5a}$$

$$\left.\begin{aligned} &= 1-e^{-R_p/L}\cosh(x/L) \quad [x \le R_p] \\ &= e^{-x/L}\sinh(R_p/L) \quad [x \ge R_p] \end{aligned}\right\} \tag{5-5b}$$

where m_∞^{int} is the high-temperature limit of m^{int}; the full, i.e. time dependent , expression of m^{int} is somewhat cumbersome.

The solutions of equations (5-3) for the other types of distribution, such as e^{-x} and xe^{-x}, have also been derived in reference 60. The graphical representations of equations (5-4) and (5-5) still show the rotation effect.

5.2.3 Diffusion in the Presence of Reversible Traps with Uniform Depth and Spacing

When a large number of trappings takes place, a more realistic form for the diffusion equation is probably that with trapping terms as described by Hurst[62]:

$$\frac{\partial C}{\partial t} = D\frac{\partial^2 C}{\partial x^2} - \frac{DC}{L^2} + bm \tag{5-6a}$$

$$\frac{\partial m}{\partial t} = \frac{DC}{L^2} - bm \tag{5-6b}$$

where C,D,L, m have the usual meanings, and b is the detrapping rate constant. These equations are solvable as they stand provided D,L, and

b are constants: for example, Gaus[63] has developed solutions for a semi-infinite medium. The integral-concentration solutions for a plane source at $x = R_p$ in a plane sheet of thickness ℓ, such that:

$$C = 0 \qquad \text{at } x = 0$$

$$\frac{\partial C}{\partial x} = 0 \qquad \text{at } x = \ell$$

and $$m^{int} = 0 \qquad \text{at } t = 0$$

have been derived in reference 12:

$$C^{int} \simeq \frac{4}{\pi}\sum_{n}\frac{1}{2n+1}\cos(ax)\sin(aR_p)F_c(D,L,b,\ell,t) \qquad (5\text{-}7a)$$

$$m^{int} \simeq \frac{4}{\pi}\sum_{n}\frac{1}{2n+1}\cos(ax)\sin(aR_p)F_m(D,L,b,\ell,t) \qquad (5\text{-}7b)$$

where a stands for $(2n+1)\pi/2\ell$, and F_c and F_m are functions of D,L,b,ℓ, and t, as stated in reference 12. The corresponding solution for diffusion without trapping follows by letting $L \to \infty$:

$$C^{int} = \frac{4}{\pi}\sum_{n}\frac{1}{2n+1}\cos(ax)\sin(aR_p)\exp(-Da^2t) \qquad (5\text{-}8)$$

The overall diffusion ($C^{int} + m^{int}$) in the presence of reversible traps was argued to consist of two parts: one part is governed by un-diffusion-like parameters (namely $\sim DAt/L^2$) and the other is governed by diffusion-like parameters almost equivalent to D being replaced by bL^2 (namely $\sim bL^2a^2t/A$), (where A stands for $1 + a^2L^2$).

5.3 DIFFUSION WITH NON-UNIFORM DIFFUSION PARAMETERS

Diffusion when the parameters are not uniform with depth constitutes a variant of particular interest in this work. Several situations have been envisaged. Fairfield and Crowder[66], and Meyer and

Mayer[67] have treated the diffusion in a composite target with D being larger near the surface than deeper in, though the solutions obtained are incorrect. (They neglected the boundary.) Kelly and Nghi[12] and Pronko and Kelly[68] considered the target being composite in the converse sense, due to D being smaller in the surface layer than inside. This could arise from there being a higher damage concentration in the vicinity of the damage mean range than beyond it, a situation which is shown to be fairly realistic from the truncated Gaussian shape of the damage distribution profiles. Both the above situations will be noted to correspond to an idealization of target which consists of the sequence surface/damage/no-damage. As an alternative the target may be regarded as having either a continuous fall-off in damage concentration, thence an increase in D, from the damage mean range to the interior, or else, a continuous decrease in the trap depth, thence an increase in D, from the damage mean range to the interior. Most ideally, of course, D would be given a Gaussian variation, but analytical solutions cannot then be obtained.

On the atomic scale, the diffusion barriers that would be seen by a diffusing entity may be represented in three ways as in Figure 5-2. Here (a) corresponds to the case of Meyer and Mayer[67], (b) to the case of Kelly and Nghi[12], and (c) to the case of a continuous decrease in trap depths.

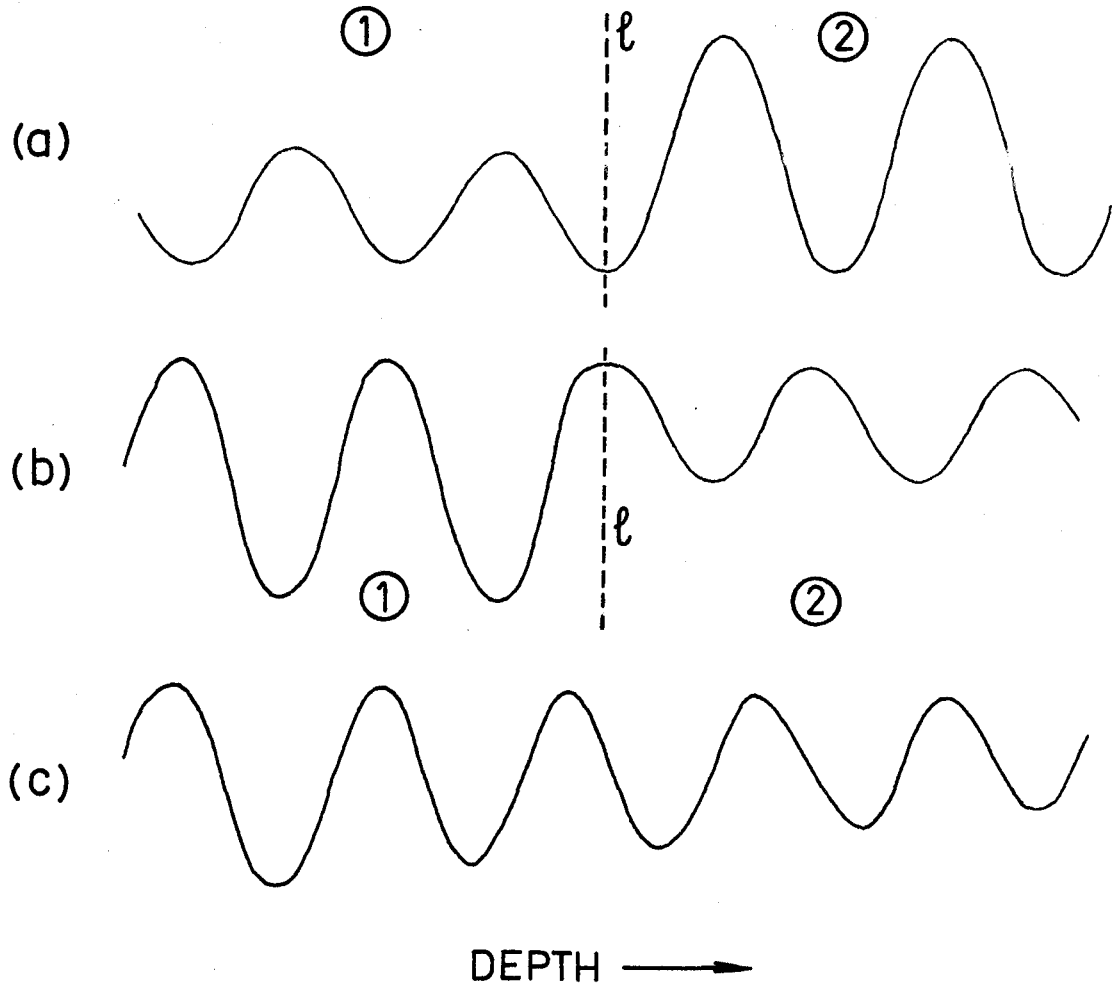

Figure 5-2 Schematic representation of the atomic-scale barriers that would be seen by an entity diffusing (a) near a boundary ℓ described by equation (5-9), (b) near a boundary at ℓ described by equation (5-11), and (c) when there is a continuous decrease in trap depth (equation (5-16)).

5.3.1 Solutions for Damage/No-Damage System

We first examine the two cases (a) and (b) where a region with deep traps adjoins a region with shallow traps.

Carslaw and Jaeger[69] discuss a situation very close to this, involving an infinite solid with a boundary at ℓ separating regions with different D. The conditions obeyed at the boundary are:

$$C_1 = C_2$$
$$D_1 \frac{\partial C_1}{\partial x} = D_2 \frac{\partial C_2}{\partial x} \qquad (5\text{-}9)$$

and the boundary might be represented as in Figure 5-2a.

The total amount of diffusant in region 2 has been found to be:

$$C_{x=\ell}^{int} = \int_{\ell}^{\infty} C_2 dx = \frac{2f}{f+1} (D_1 t/\pi)^{1/2} \qquad (5\text{-}10)$$

where f stands for $(D_2/D_1)^{1/2}$. This result shows that for $D_2 << D_1$, which is similar to the model used in references 66 and 67, $C_{x=\ell}^{int}$ tends to become zero and this could explain occasional instances[66-67] in which the rotation effect was absent.

The above treatment is not quite correct when the difference in D is due to trapping effects. When traps are being considered, $D_2 >> D_1$ becomes physically more realistic, and a more correct treatment would be based on the following boundary conditions:

$$D_1 C_1 = D_2 C_2$$
$$D_1 \frac{\partial C_1}{\partial x} = D_2 \frac{\partial C_2}{\partial x} \qquad (5\text{-}11)$$

This situation can be represented, on an atomic scale, by Figure 5-2b where the boundary at ℓ separates two regions of different types of traps. For example, the traps might be respectively multiple and single vacancies[70] or the presence and absence of dislocation loops[71].

The total amount of diffusant in region 2, calculated with the boundary conditions (5-11), has been shown to be:

$$C_{x=\ell}^{int} = \frac{2}{f+1} (D_1 t/\pi)^{1/2} \qquad (5\text{-}12)$$

The result is very similar to what was obtained before, except that $C_{x=\ell}^{int}$ now approaches zero for $D_2 >> D_1$.

A boundary between regions with different D thus sometimes acts as nearly impermeable interface provided D_2/D_1 takes on the appropriate value.

5.3.2 Solutions for Surface/Damage/No-Damage System

We now consider a more detailed case involving boundary (5-11) namely C=0 at x=0 while at $x=\ell$ (where ℓ would in practice be related to $<R_d>$) the trap depth decreases abruptly in accordance with Figure 5-2b. Such a model would be applicable both at low bombardment energies or high doses, whence the sequence surface/damage/no-damage, and to a lesser extent, at high energies or low doses, whence the sequence surface/no-damage/damage/no-damage.

The total build-up of diffusant in region 2 has been determined as:

$$C_{x=\ell}^{int} = \frac{\tau}{f+1} \left\{ \frac{1}{\pi} - 2\ \text{ierfc}(1/\tau) + \frac{2}{f+1}\ \text{ierfc}\ (2/\tau) \right.$$

$$\left. + \frac{2(f-1)}{f+1}\ \text{ierfc}(3/\tau) - \frac{2(f-1)}{(f+1)^2}\ \text{ierfc}(4/\tau) + \ldots \right\} \qquad (5\text{-}13)$$

where τ is equal to $2(D_1 t/\ell^2)^{1/2}$. $C_{x=\ell}^{int}$ is plotted as a function of temperature in Figure 5-3.

The interesting result is that the possibility that the rotation effect may sometimes be absent, as already alluded to in the preceding section, is evident for $\Delta H_2/\Delta H_1 \leq 5/6$. Real implantation geometries

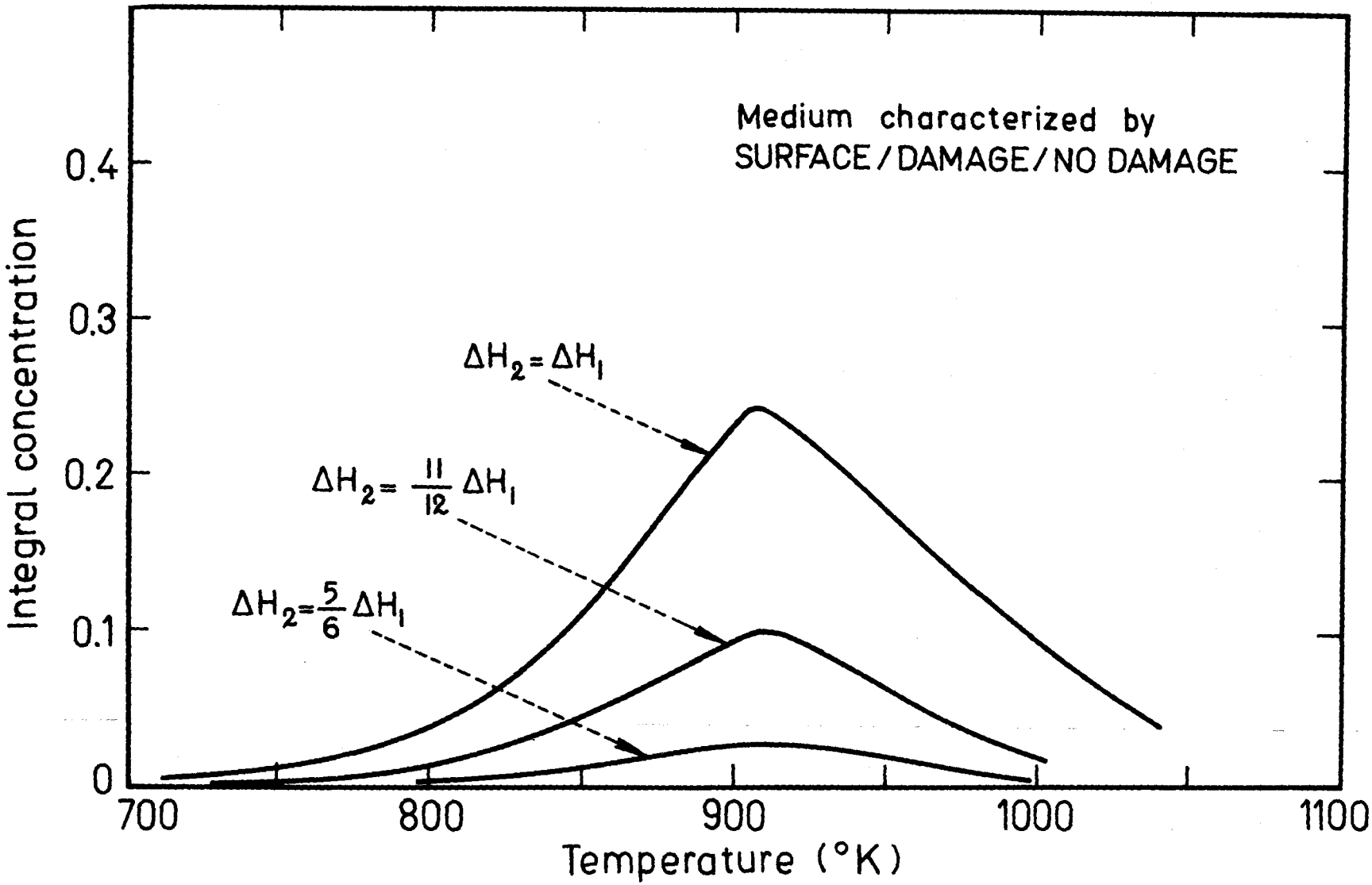

Figure 5-3 The build-up of diffusant in region 2 ($x \geq \ell$). Based on (5-13) with $D_o = 0.3$ cm^2/sec, $t = 300$ sec, $\ell = 10^{-6}$cm, and $\Delta H_1 = 60{,}000$ cal/mole

could, in principle, be treated as in this part.

5.3.3 Solutions for Variable Trap Spacing

It may in some cases be an oversimplification to regard a damaged target as consisting of two regions, each with a different trap depth. A possible alternative would be to allow for continuous variation of trap spacing, ie. to write:

$$L^2 = L_o^2 (1 + cx) \qquad (5\text{-}14)$$

where L_o is the value of L at the surface. From section 5.2.3 it follows that the problem becomes one of solving :

$$\frac{\partial C}{\partial t} \simeq bL_o^2 \frac{\partial}{\partial x} \left[(1 + cx)\frac{\partial C}{\partial x}\right] \qquad (5\text{-}15)$$

Solutions to an equation similar to this have recently been obtained by Kelly (unpublished) and show that the rotation effect, as in Figure 5-1, not only still occurs, but is even more prominent than usual.

A system in which the trap spacing increases from the surface to the interior, though it certainly represents a possible description of a bombarded target, thus does not lead to significantly deviant behaviour.

5.3.4 Solutions for Variable Trap Depth

Still a further approach for describing diffusion in ion-implanted solids is to allow for a continuous variation in the trap depth as shown in Figure 5-2c:

$$\Delta H = \Delta H_o (1 - gx) \qquad (5\text{-}16)$$

hence, $$b = b_o \exp(-[\Delta H_o/RT][1-gx]) \qquad (5\text{-}17)$$

where ΔH_o is the value of ΔH at the surface, and b_o is a pre-exponential term probably similar to $10^{15\pm1}$ sec^{-1} [72]. The problem to solve may therefore be written approximately as:

$$\frac{\partial C}{\partial t} \simeq (b_o L^2 \exp[-\Delta H_o/RT]) \frac{\partial}{\partial x} (\exp[\Delta H_o g x/RT] \frac{\partial C}{\partial x}) \qquad (5\text{-}18)$$

Substituting $s = \exp(-\Delta H_o g x/2RT)$, one can obtain the equation:

$$\frac{\partial C}{\partial t} = \overline{D} \left(\frac{\partial^2 C}{\partial s^2} - \frac{\partial C}{s \partial s}\right) \qquad (5\text{-}19)$$

where $\overline{D} = b_o L^2 (\Delta H_o g/2RT)^2 \exp(-\Delta H_o/RT)$, subject to the boundary conditions $C=0$ at $s=1$ and C definable as $s \to 0$.

The integral-concentration solution for a plane source at $x=R_p$, i.e. $s=s_p$, has been derived in reference 12:

$$C^{int} = 2s_p \sum_{\alpha_n} \frac{1}{\alpha_n J_o^2(\alpha_n)} \{1-J_o(\alpha_n s)\} J_1(\alpha_n s_p) \exp(-\overline{D}\alpha_n^2 t) \qquad (5\text{-}20)$$

where $\alpha_1 = 3.83$ and $J_1(\alpha_1) = 0$ [73].

The numerical examination of equation (5-20) has been done in reference 12. It is found that a surprisingly modest value of gR_p, i.e. what is in effect a small fractional reduction in ΔH over the range of the implanted ions, has been sufficient to eliminate the rotation effect of Figure 5-1. Figure 5-4 is taken as an example to show the surface-directed motion of the implanted ions, assuming $\Delta H_o/RT = 40$ and an initial plane-source distribution. The curves which are normalized to begin at $C^{int} = 1$, may be interpreted as showing that rotation occurs for $gR_p < 1/40$, while motion toward the surface takes place for $gR_p > 1/40$.

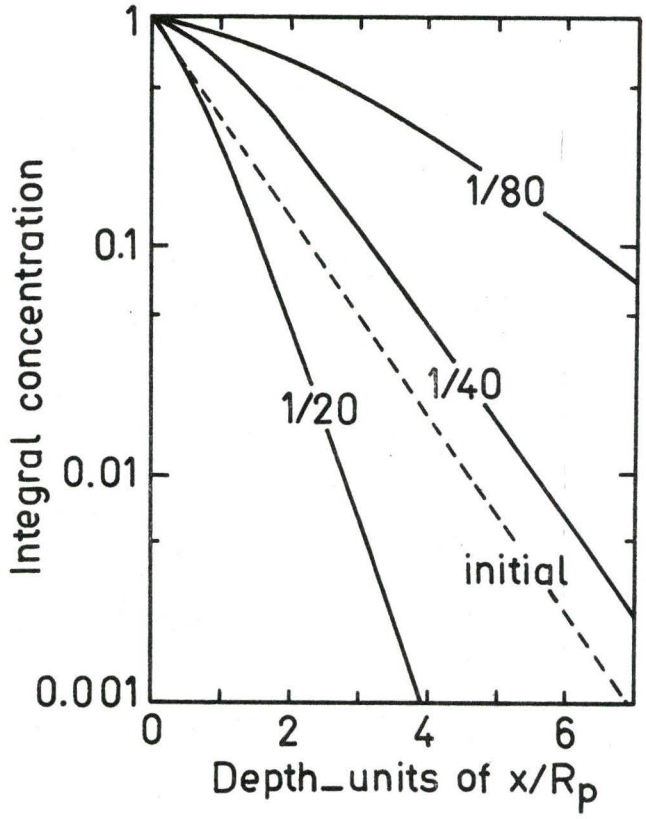

Figure 5-4 Integral-concentration curves obtained from equation (5-20) with s=exp(-20gx). Curves are normalized to begin at $C^{int}=1$, and correspond to $gR_p=1/80$, 1/40, and 1/20.

Real implantation geometries are not quite as simple to treat, except for the particular cases of rectangular and e^{-x}-type distributions. It was suggested that a useful approximation to equation (5-20) would be the following relation, normalized to yield unity for x=t=0:

$$C^{int} \simeq 0.713[1-J_o(\alpha_n \exp\{-\Delta H_o gx/2RT\})]\exp(-\overline{D}\alpha_n{}^2 t) \qquad (5\text{-}21)$$

This relation is reasonably exact for $\overline{D}t$ sufficiently large that the fraction of the diffusant remaining is ≤ 0.80.

As a word of caution, it should be emphasized that equation

(5-20) involves an unrealistic situation in which the trap depth continues to decrease indefinitely. The conclusions should, therefore, be regarded as tentative.

CHAPTER 6

EXPERIMENTAL PROCEDURES

6.1 MATERIALS

The anodic oxides of Al, Mo, Nb, Si, Ta, Ti, V, W, and Zr were used during the course of this work. The metal substrates were high-purity polycrystalline foils of dimensions 20x20x0.1 mm. All specimens were chemically polished before the anodizing step. In addition, Al, Mo, Nb, V, and W were given a pre-anodizing treatment, which consisted of the successive formation and dissolution of several anodic oxide layers approximately 1000-2000 Å thick. This pre-anodization helps remove submicroscopic irregularities, thus giving a reproducibly flat clean surface of constant area.

6.2 ANODIZATION

The anodic oxidations were all carried out at constant current. Table 6-1 summarizes the electrolytes, conditions of anodization, and thicknesses of oxide films formed on metals used:

TABLE 6-1

Information on Anodic-Oxide Formation

Metal	Oxide	Electrolyte and Conditions of Formation	Oxide Thickness	Ref.
Al	Al_2O_3	Aqueous solution of C.P. Ammonium citrate (30g/liter), room temperature, cathode: Al time: 10 min. current density: $\leq$10 mA/cm^2	x=0.472(V+1.8) (μg/cm^2)	(74)

Mo	MoO_3 (assumed)	Solution of 2M H_2O and 0.02M $Na_2B_4O_7$ in acetic acid, room temperature, cathode: Pt time: 15 min. current density: 2 mA/cm^2	x=1.40+1.78V (μg/cm^2)	(75)
Nb	Nb_2O_5	(1) Aqueous solution of 0.25% KF, room temperature, cathode: stainless steel time: 10 min. current density: $\leq$20 mA/cm^2	x=1.4+1.41V (μg/cm^2)	(7) Fig.6-1
		(2) Solution of H_2SO_4 (80 parts) and HNO_3 (20 parts), temperature : < 30°C, cathode: Pt time: 5 min. current density: 10 mA/cm^2	x=1.4+0.69V (μg/cm^2)	(76) Fig. 6-2
Si	SiO_2 (assumed)	Solution of ethylene glycol (96 ml), H_2O (4 ml), and KNO_3 (0.4 g), room temperature cathode: Pt time: 20 min. current density: 10 mA/cm^2	x $\simeq$ 5.75V (Å)	(77) (78)
Sn	SnO_2	Solution of ethylene glycol (90 ml) and ammonium pentaborate (30 g), room temperature, cathode: Pt time: 1 hour current density: 10 mA/cm^2		(79)
Ta	Ta_2O_5	Aqueous solution of 0.2% KF, room temperature cathode: stainless steel time: 3 min. current density: $\leq$ 20 mA/cm^2	x $\simeq$ 16.7V (Å)	(80)
Ti	TiO_2	Aqueous solution of 1% KOH room temperature cathode: Pt time: 3 min. current density: 10 mA/cm^2	x $\simeq$ 22 V (Å)	(6)
V	V_2O_5 (assumed)	Same electrolyte and conditions as for anodizing Mo	x = 1.42 V (μg/cm^2)	(75)

W	WO_3	Aqueous solution of 0.4 M KNO_3 and 0.04 M HNO_3, room temperature cathode: Pt time: 1 min. current density: 2 mA/cm^2	x=3+1.28V ($\mu g/cm^2$)	(81) Fig.6-3
Zr	ZrO_2	Aqueous solution of ammonium pentaborate (30g/liter), room temperature, cathode: Pt time: 3 min. current density: 10 mA/cm^2	$x \simeq 27V$ (Å)	(82)

For thick films formed at $\geq$ 10 volts, the relation between the oxide film thickness and the anodic voltage was determined by the conventional weight-change method. In the case of W, specimens were weighed, with a micro-balance, before (i.e. after anodization) and after dissolution of WO_3. For Nb, however, the weight change of Nb foils before and after anodization has been measured, the weight gain (due to oxygen) being then converted to oxide thickness using a simple stoichiometric relation. The specimens used were in all cases large enough to give meaningful weight-change measurements (i.e. $\geq$ 50μg).

Figure 6-1 shows the variation of the thickness of an Nb_2O_5 film formed by anodizing in 0.25% KF for 10 min. as a function of anodization voltage. In agreement with the case of Ta_2O_5[83], the thickness of Nb_2O_5 does not depend on the history of the Nb substrate; in fact, we have the same calibration curve for non-preanodized and preanodized specimens. We can also anodize Nb in H_2SO_4 - HNO_3 solution (Table 6-1), the thickness-voltage calibration being given in Figure 6-2.

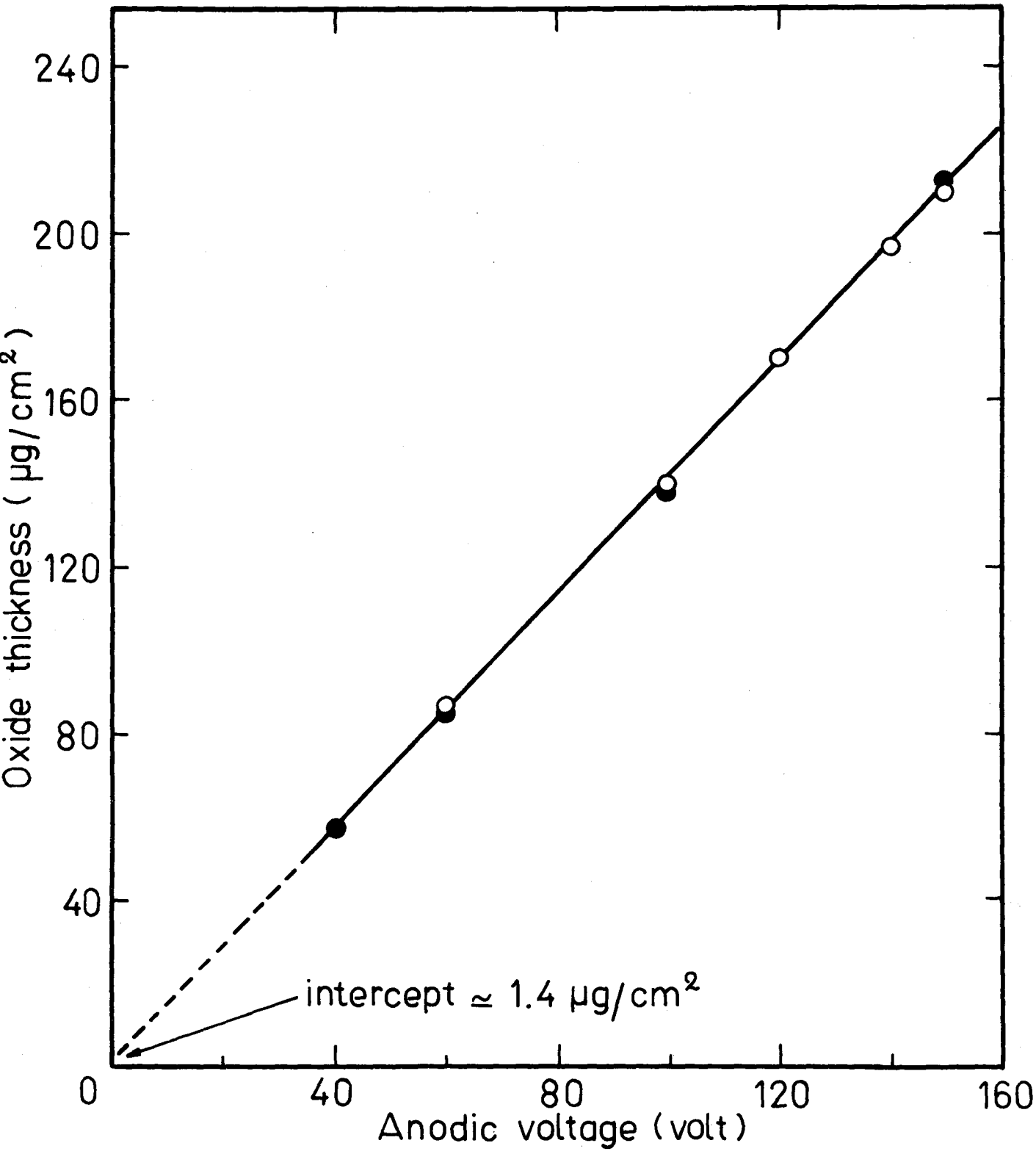

Figue 6-1 Thickness-voltage calibration of Nb_2O_5 film formed in 0.25% KF, 10 min. ○: preanodized specimens, ●: non-preanodized specimens .

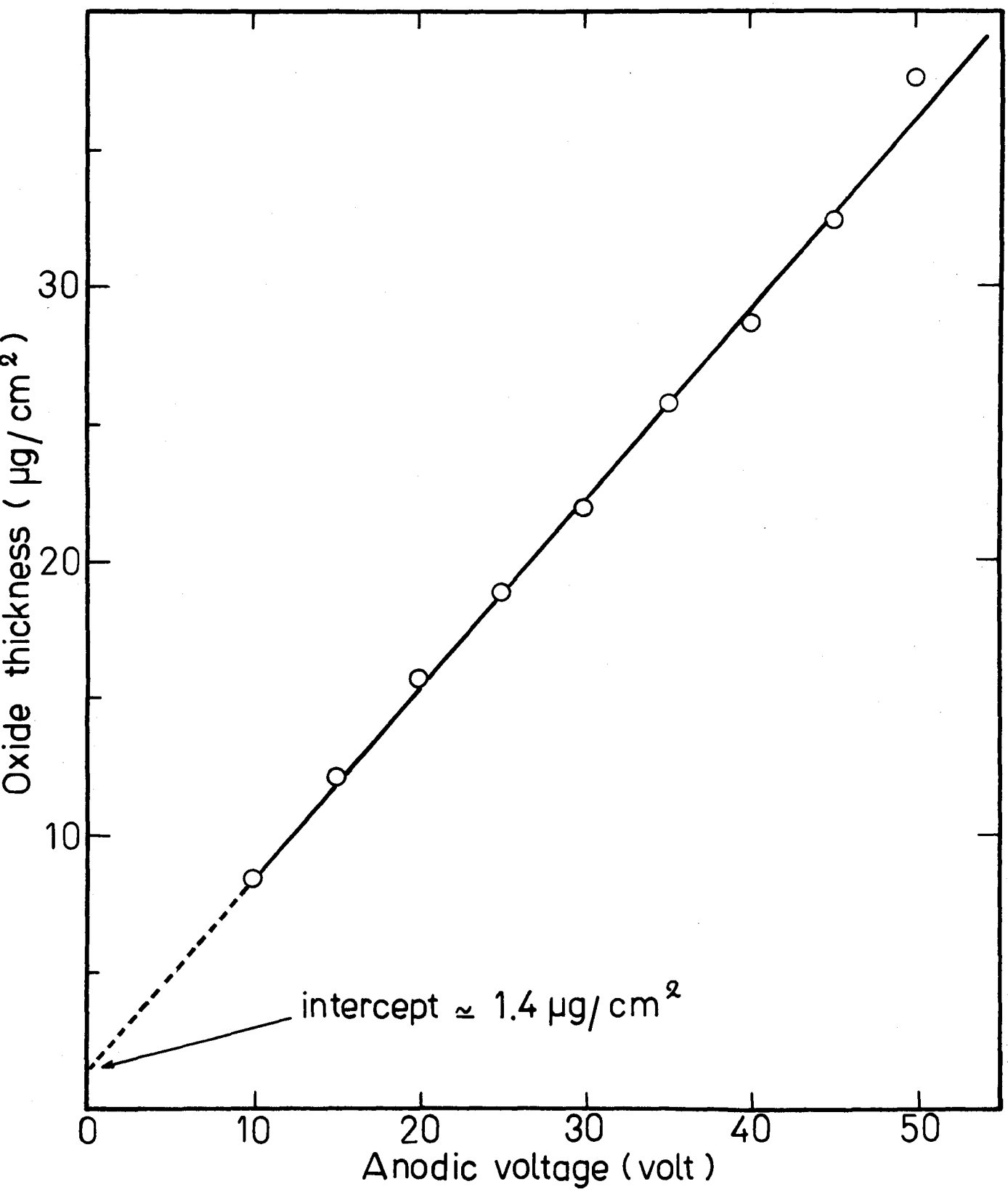

Figure 6-2 Thickness-voltage calibration of Nb_2O_5 film formed in H_2SO_4-HNO_3 electrolyte, 5 min.

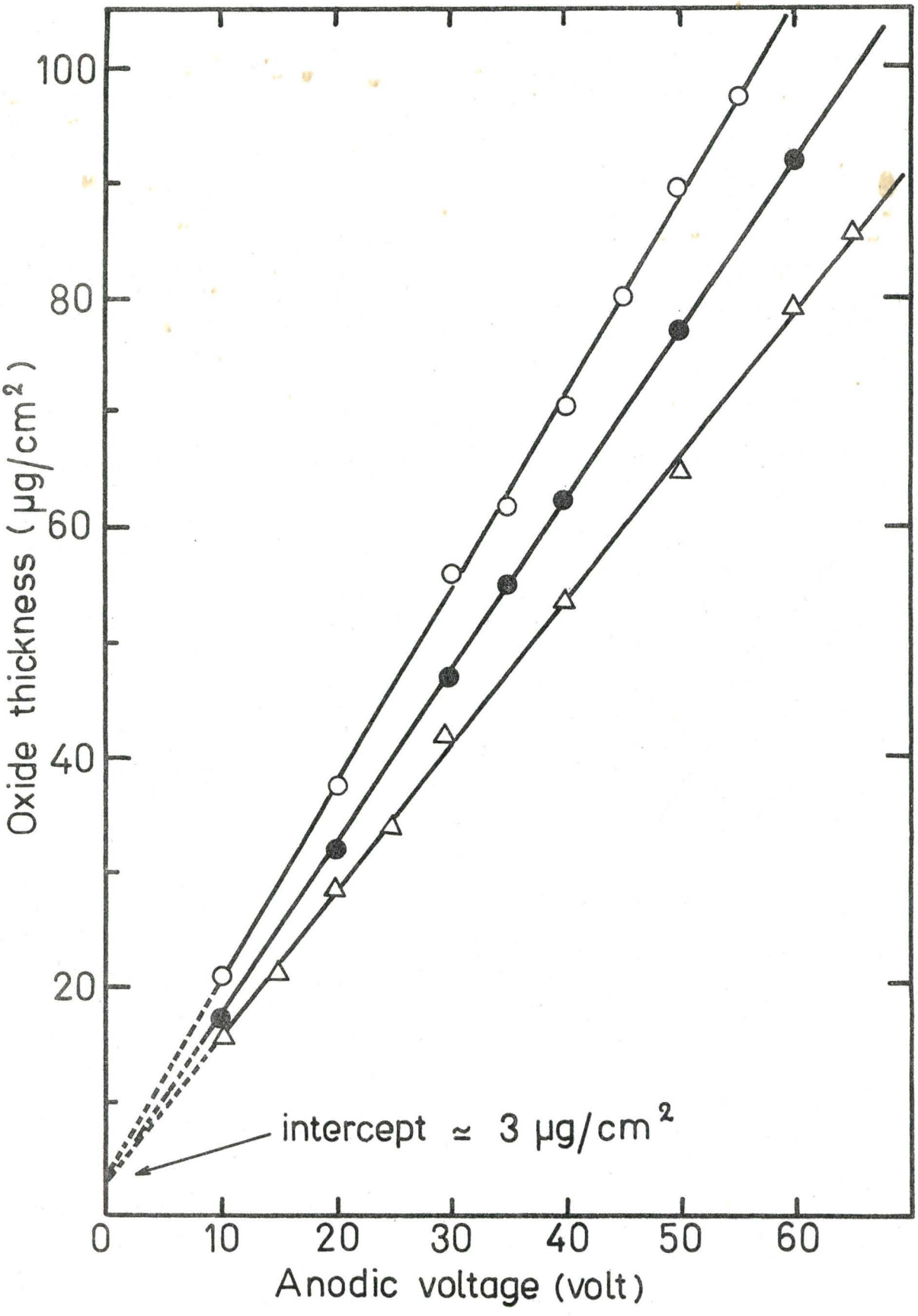

Figure 6-3 Thickness-voltage calibration of WO_3 film formed in KNO_3-HNO_3 electrolyte. ○: non-preanodized specimens, anodized for 3 min; ●: non-preanodized specimens, 1 min; and △: preanodized specimens, 1 min.

The thickness of anodic WO_3 formed in KNO_3 - HNO_3 electrolyte is illustrated in Figure 6-3, as a function of anodization voltage. In contrast to Nb_2O_5, the final thickness of a WO_3 film is influenced by the history of the W substrate: in particular, preanodization (Figure 6-3) and cold work[84]. Around 80 volts, the anodization in KNO_3 - HNO_3 electrolyte became difficult and in order to reach higher voltages (up to ~250V), the electrolyte for anodizing Mo and V (Table 6-1) must be used[75].

6.3 DISSOLUTION OR STRIPPING OF OXIDES

The anodic oxides can be removed from the metal substrates by dissolution or stripping, depending on the oxide. Solvents used and conditions of oxide removal are summarized in Table 6-2. The oxides anodically formed on Al, Mo, Nb, V, and W can be dissolved completely, using solvents which do not attack the underlying metals. The oxide-metal interface therefore corresponds to an end-point of the oxide dissolution. This characteristic property has an important application in the study of depth distributions of ions in metals and oxides, and will be discussed again in Chapter 8.

TABLE 6-2

Information on Removal of Anodic Oxides

Oxide	Solvent and Conditions	Remark	Ref.
Al_2O_3	Dissolved in aqueous solution of H_3PO_4 (50g/liter) and CrO_3(30 g/liter); temperature: >90°C time: 2 min.	Dissolution end-point occurs at oxide-metal interface	(74)
MoO_3	Dissolved in dilute solution of KOH time: < 1 min.	Dissolution end-point occurs at oxide-metal interface	(75)

Nb_2O_5	(1) Film formed in KF solution can be stripped mechanically using a 2% solution of Parlodion in amyl acetate		(7,80)
	(2) Film formed in H_2SO_4-HNO_3 solution can be dissolved in azeotropic solution of 68% HNO_3, boiling at 120°C	Large decrease in the dissolution rate occurs at oxide-metal interface.	(76) Figs.8-3 & 8-6
	(3) Nb_2O_5 can also be dissolved in a solution of 40% HF saturated with NH_4F	Very large decrease in the dissolution rate occurs at oxide-metal interface	(85) Figs.8-2 & 8-5
SiO_2	Dissolved in aqueous solution of 1N HF, time: 2-3 min.	Large decrease in the dissolution rate occurs at oxide-metal interface	(86)
Ta_2O_5	(1) Film formed in KF solution can be stripped mechanically using a 2% solution of Parlodion in amyl accetate.		(7,80)
	(2) Ta_2O_5 can also be dissolved in a solution of 40% HF saturated with NH_4F	Large decrease in the dissolution rate occurs at oxide-metal interface	(87)
TiO_2	Dissolved in dilute HF	No end-point	(6)
V_2O_5	Same solvent as for MoO_3	Dissolution end-point occurs at oxide-metal interface	(75)
WO_3	Same solvent as for MoO_3	Dissolution end-point occurs at oxide-metal interface	(81) Figs. 8-1 & 8-4
ZrO_2	Dissolved in a 5% solution of HF	No end-point	(88)

6.4 ION BOMBARDMENT

In this work all the bombardments have been performed with either Kr or O_2 ions, and for most of them, using an ion accelerator which can operate within the energy range from 2-40 keV yielding currents up to 100 μA. This ion accelerator does not allow for mass separation, though it permits suppression of secondary electrons. The lack of mass separation should not be a serious problem provided only heavy ions are used, since impurity ions, which are always of low mass, would create less damage than one predicts from their abundance.

Figure 6-4 shows a general view of the ion accelerator which we have in our laboratory. The gas to be implanted is stored in a small pressurized container located near the ion source. The gas is bled into the discharge vessel at a controlled rate through a variable leak. Before entering the ion source, however, the gas passes through a liquid-nitrogen trap, where water vapor and other condensable impurity gases are eliminated by condensation. The detail of the accelerating column is shown in Figure 6-5. The ions are produced in a discharge vessel, which is a radio-frequency-type ion source (A), they are then extracted through a small aluminum canal, focused by means of a series of electrostatic lenses (B), and accelerated by an electrical field. The energies beyond those which are necessary to the extraction (2-5 keV) were obtained by rendering the target negative (0-35 keV) with respect to the extraction canal.

Figure 6-6 shows the target arrangement (C) used in room-temperature bombardments. A Faraday cage in two parts (a and a') floating

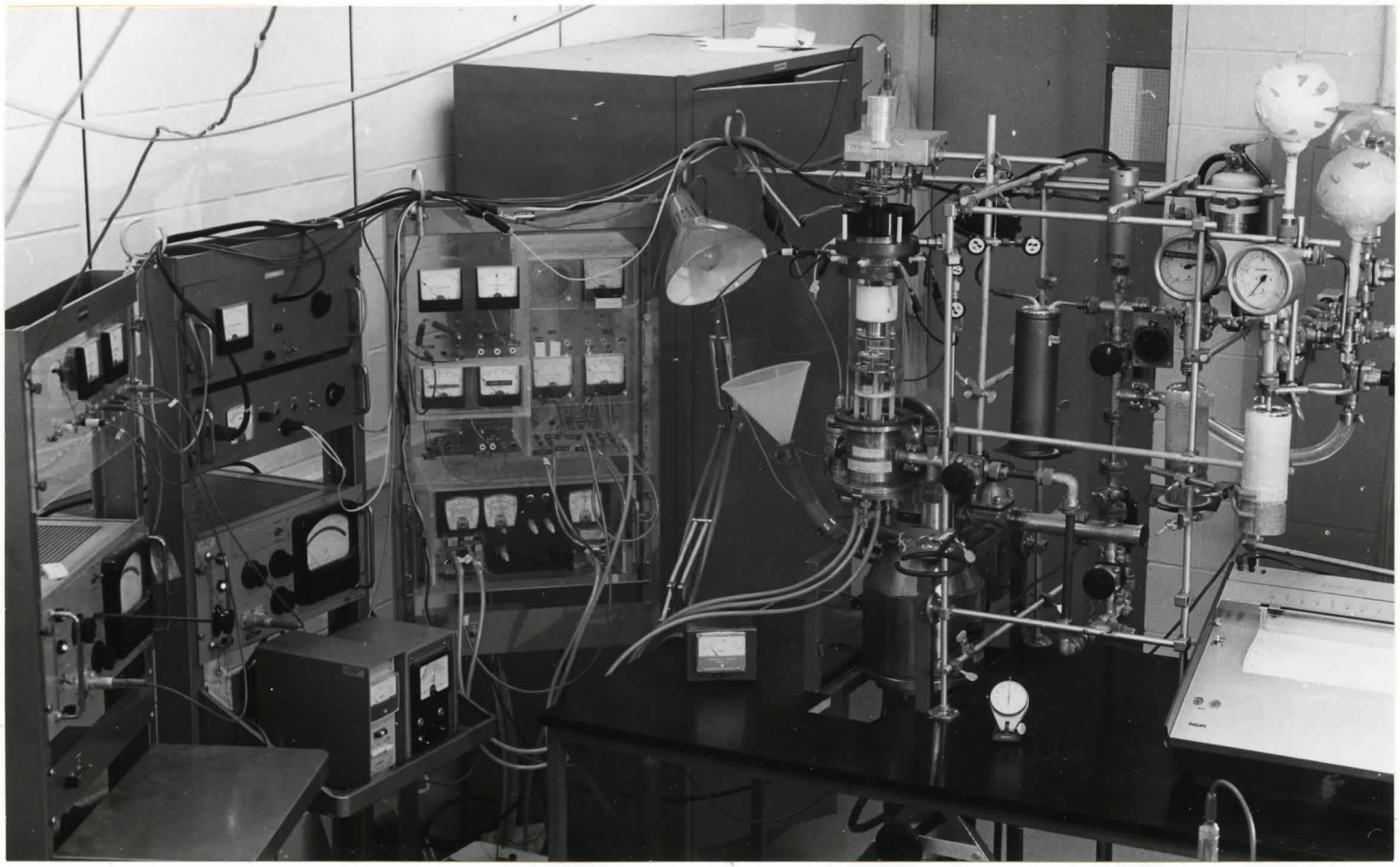

Figure 6-4 General view of the ion accelerator

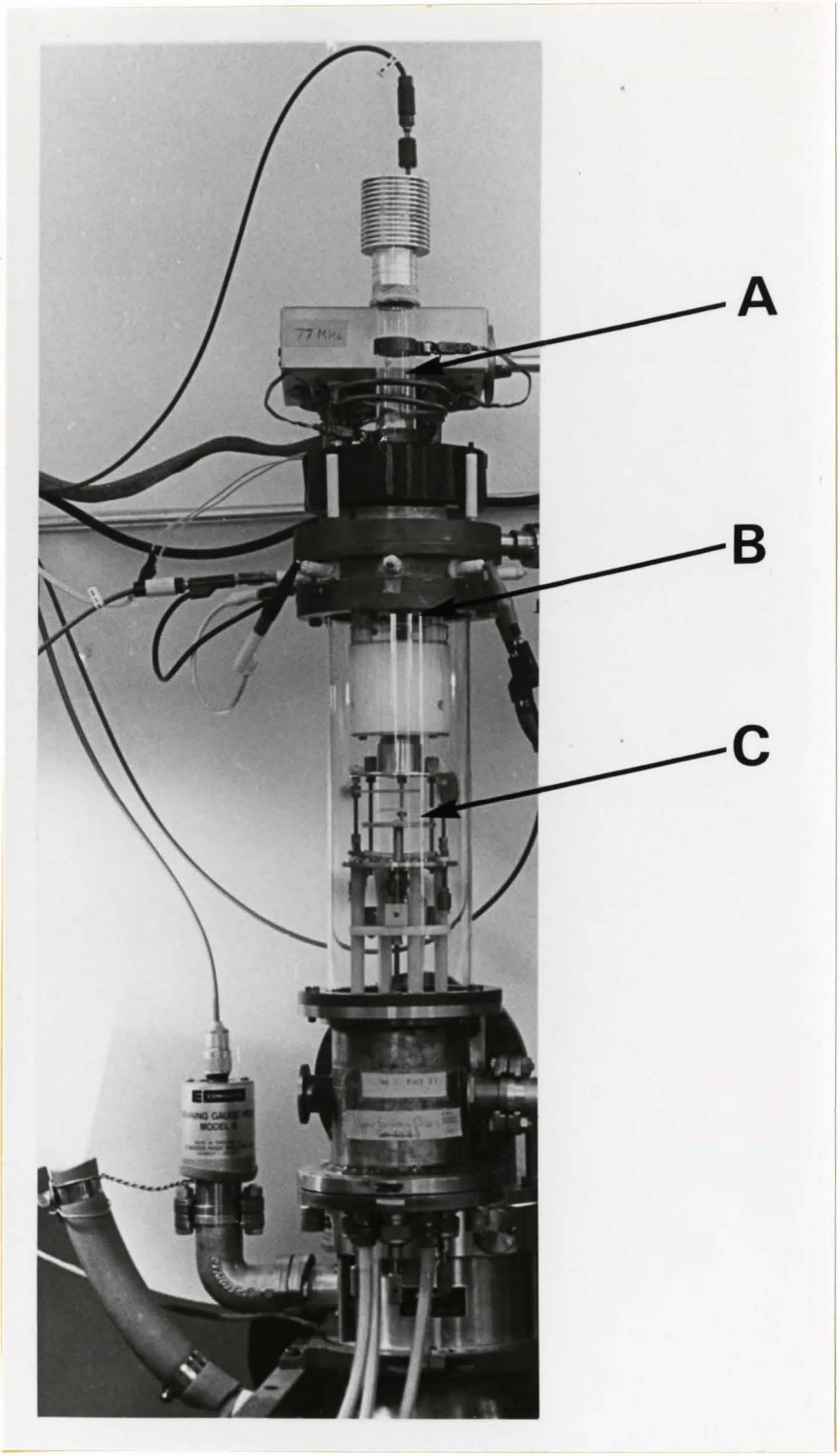

Figure 6-5 Accelerating column. A: RF ion source; B: focusing electrodes; and C: target arrangement

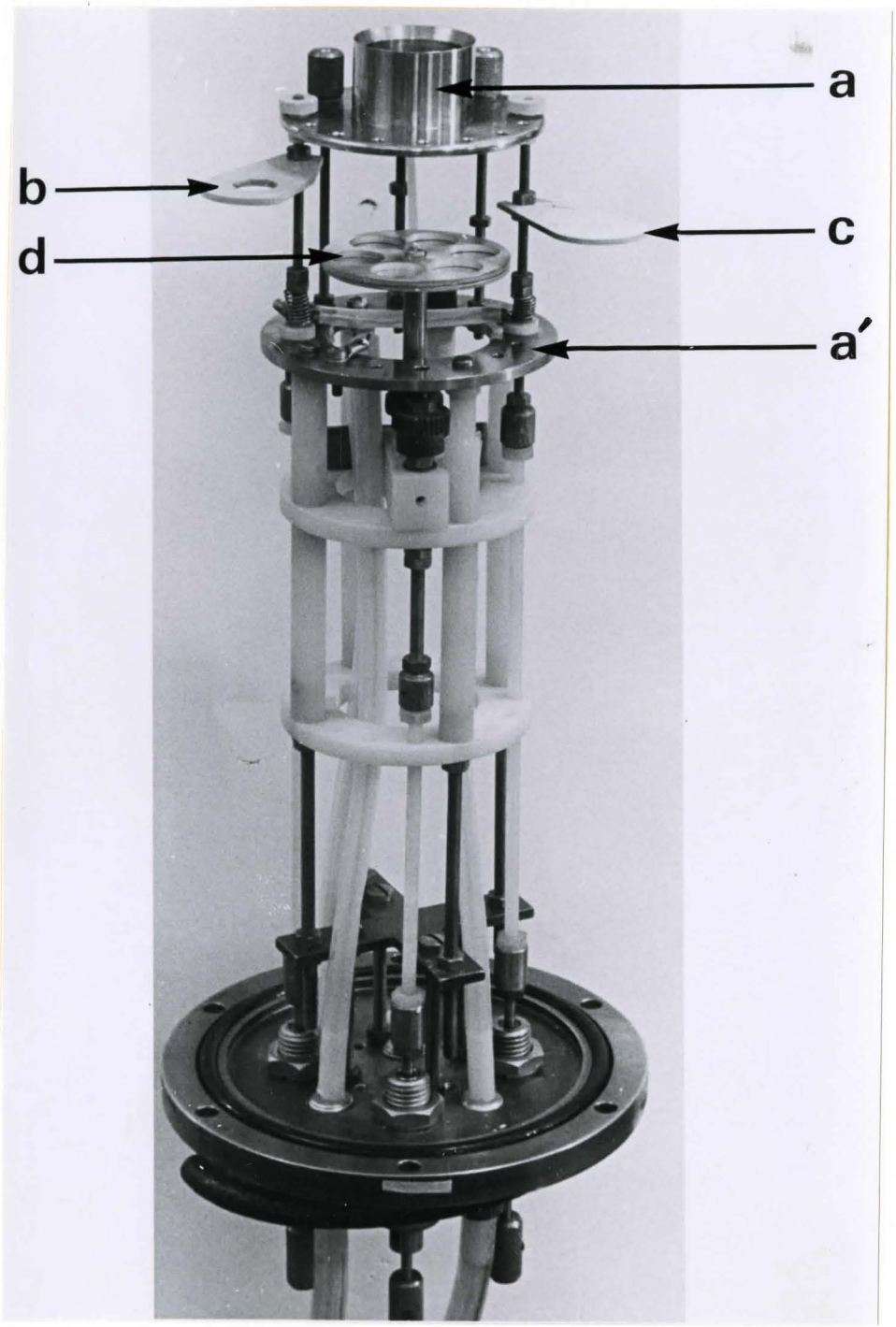

Figure 6-6 Target arrangement.a and a': Faraday cage; b: shutter and electron suppressor; c: fluorescent screen and electron suppressor; and d: target holder

at -800 volts with respect to the target is used to prevent the escape of secondary electrons, which would give false ionic-current readings. An intermediate shutter (b) for either stopping temporarily the bombardment or shaping the beam and a fluorescent screen (c) for observing the ion beam, are negatively biased at -400 volts so that they also yield true currents. The target (d) is connected to the negative terminal of a high-tension power supply. For room-temperature bombardments, the target arrangement is quite simple; in the case of low- and high-temperature implantations, however, the target holder must be modified in such a way that we can cool or heat the specimens (Figures 8-17 and 8-22).

During the bombardment, the pressure in the accelerating column was $\simeq 10^{-6}$torr, corresponding to an ion mean free path of $\simeq 10^{4}$ cm.

6.5 DESIGN FOR GAS-RELEASE EXPERIMENTS

In these experiments, specimens were Tessla-labeled[89] with $\sim$ 1-keV Kr^{85} at liquid-nitrogen temperature and were heated first to room-temperature and then (after a short unavoidable interruption) beyond.

The experimental design is shown in Figure 6-7. This system, which was used for both low-energy bombardment and gas release, consists of two large pyrex tubes, 1 and 2, separated by a valve (B). Before the bombardment, the two chambers 1 and 2 were evacuated and immersed in liquid nitrogen. With valves A,B,C, and D being closed and a low pressure of Kr^{85} (tenths of a torr) being established in the tube 1, which contained the specimen, a Tessla discharge was produced by connecting a planar electrode placed externally on the bottom of the tube 1 with the high-voltage terminal of a 1.6 MHz high-frequency generator which could be

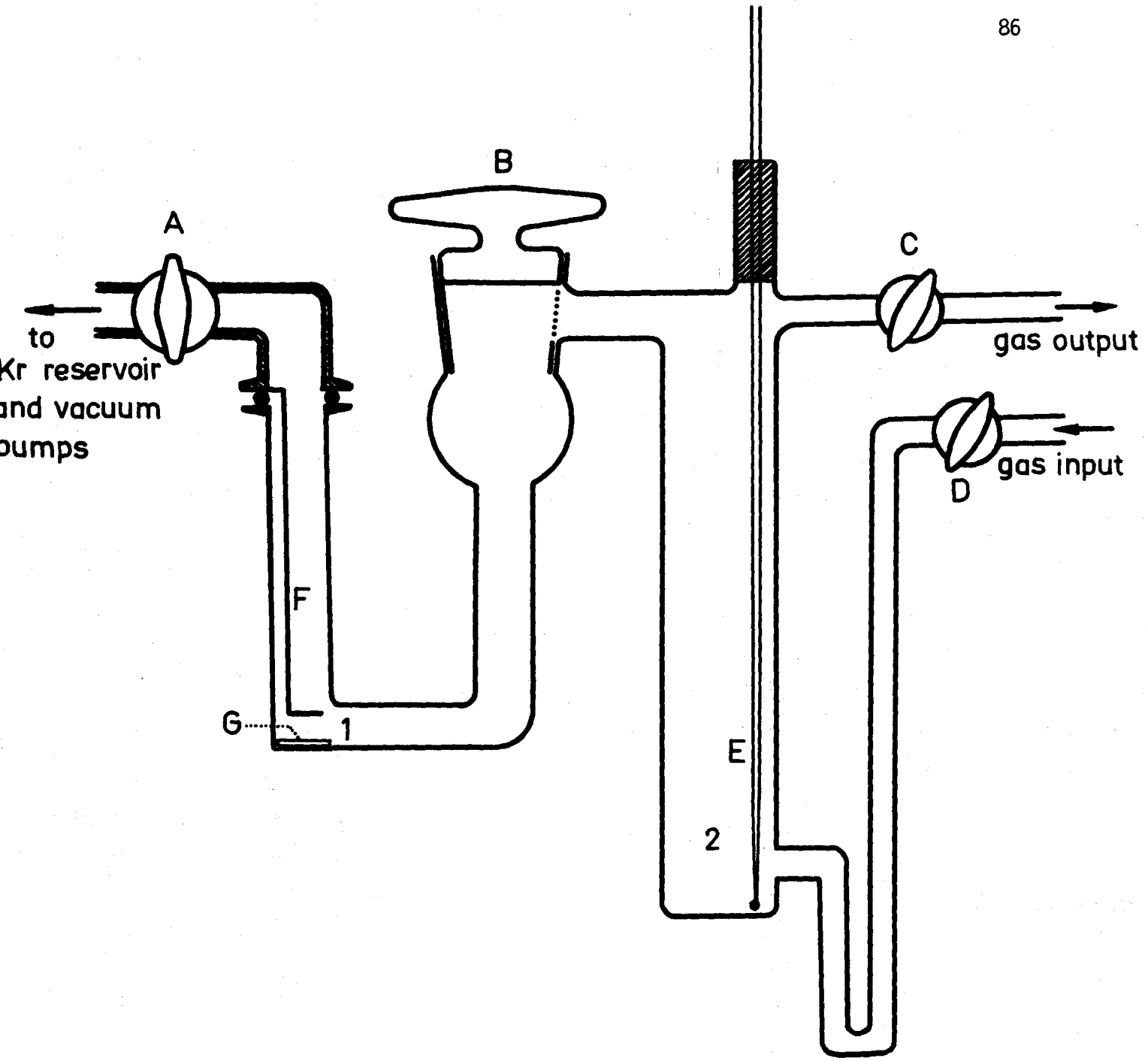

Figure 6-7 Experimental arrangement for gas release. A,B,C,D: valves; E: thermocouple; F: aluminum electrode; and, G: specimen.

actioned for a preset time of 0.1 to 7.5 sec. by means of an electronic timer. A dose of $\sim 8 \times 10^{14}$ Kr^{85} ions/cm^2 was implanted in the specimen. The radioactive gas was then removed. With the valve B opened, the specimen was brought to the chamber 2, and the valve B was then re-closed. The transfer of specimen from tube 1 to tube 2 must be very fast (1-2 sec.) in order to avoid warming up the sample, the reason for this transfer being to exclude all possible Kr desorption from the electrode and glass walls. The specimen was linearly heated, in He, to room temperature,, and the first part of gas-release spectrum was recorded.

The second part of the spectrum was obtained with the specimen transferred to another gas-release chamber, in which the specimen was linearly heated from room temperature to 1000°C.

CHAPTER 7

SPUTTERING COEFFICIENTS OF OXIDES *

7.1 TECHNIQUES

The sputtering coefficient, S, due to Kr bombardment of amorphous anodic films of Nb_2O_5, Ta_2O_5, and WO_3 has been determined for ion energies of 2-30 keV. Three methods were employed, based respectively on (a) the change of interference colors due to ion bombardment, (b) the perforation of a film of free oxide by an intense ion beam, and (c) the loss of weight of the target.

(a) The first method to determine S consists of bombarding, with Kr ions, specimens anodized at 60 V (W) and 150 V (Nb and Ta) and observing the change of interference color of the anodic film. This technique has been discussed by Nielsen and Shepherd[90] and Kelly[6]. The doses used were generally between 100 and 250 μA min. A color-voltage calibration helped interpret the final color, and deduce the apparent variation of the anodization voltage (ΔV), thence the oxide thickness (x) removed by sputtering. One could finally calculate S (atoms/ion) using the equation:

$$x(\text{in } \mu g/cm^2) = (S\overline{M}Bt)(6.21 \times 10^{-4}) \qquad (7\text{-}1a)$$

or

$$x \text{ (in } \mathring{A}) = (S\overline{M}Bt/\rho)(0.0621) \qquad (7\text{-}1b)$$

---

* This Chapter is largely based on a publication by the author and R. Kelly[7].

where $\bar{M}$ is the mean atomic mass of the target, βt is the bombardment dose (μA min/cm^2), and ρ is the density of the target (g/cm^3). The forms taken by equations 7-1a and 7-1b after substitution of $\bar{M}$ and relation between x and ΔV are given in Table 7-1.

(b) In the second method, which is only applicable to Nb_2O_5 and Ta_2O_5, one bombards a "free" anodic film of about 2700 Å thick until it perforates. After its stripping, the film, still covered with parlodion, was placed on a Ti foil anodized at 23V so as to have a deep blue color. The whole system was then put in amyl acetate where the parlodion was dissolved rapidly. Figure 7-1 illustrates a target system which is ready for bombardment.

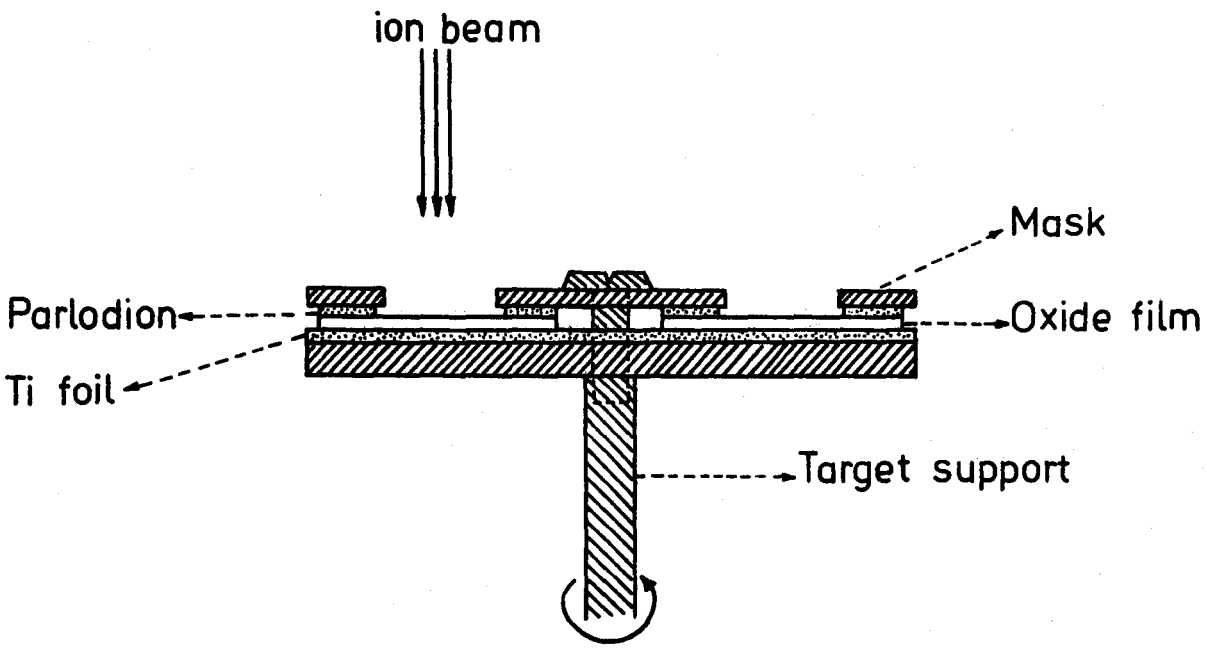

Figure 7-1 Target arrangement in the second method.

TABLE 7-1

Parameters used to Calculate S

Substance	Density (g/cm^3)	x = f(ΔV) (ΔV in volts)	S = f(ΔV) (S in atoms/ion, Bt in μAmin/cm^2)
Nb_2O_5	4.74[a]	(29.6)ΔV Å[b]	(59.5)(ΔV/Bt)
Ta_2O_5	8.04[a]	(16.7)ΔV Å[c]	(34.3)(ΔV/Bt)
WO_3 (non-preanodized)	~6.8 [d]	(1.70)ΔV μg/cm^2 [e]	(47.3)(ΔV/Bt)
		(1.43)ΔV μg/cm^2 [f]	(39.7)(ΔV/Bt)
WO_3 (preanodized)	~6.8 [d]	(1.28)ΔV μg/cm^2 [f]	(35.5)(ΔV/Bt)
		(1.34)ΔV μg/cm^2 [g]	(37.2)(ΔV/Bt)
Al_2O_3	3.12[d]	(0.472)ΔV μg/cm^2 [h]	(37.2)(ΔV/Bt)

[a] Schrijner and Middelhoek[91]

[b] Figure 6-1

[c] Pawel[80]

[d] Young[92]

[e] Figure 6-3 anodization for 3 min.

[f] Figure 6-3 anodization for 1 min.

[g] McCargo et al.[81], anodization for 1 min.

[h] Davies et al.[74]

The anodized Ti served to determine the dose necessary for a total perforation of the oxide film (generally, the dose was $\sim$ 2200 μAmin/cm^2). As the Nb_2O_5 or Ta_2O_5 became thinner and thinner, the blue of the Ti became more and more evident, until, with the onset of perforation, the Ti abruptly began changing color, and the bombardment was terminated. The sputtering coefficient S has been calculated as indicated in Table 7-1, except that ΔV was identified as the original anodic voltage. We note that forward sputtering did not play an important role in these experiments since the oxide films were $\sim$ 45 times thicker than the median range of Kr ions.

(c) The third method, the conventional one, is based on the loss of weight of a target anodized at 200 V, the specimen having been weighed with a microbalance before and after a prolonged bombardment. The typical doses were around 500 μAmin.

7.2 RESULTS FOR Nb_2O_5, Ta_2O_5, AND WO_3

Figures 7-2 and 7-3 show the variation of S for Nb_2O_5, Ta_2O_5, and WO_3 as a function of energy of Kr ions. The results obtained using the first method (color change) are considered as well verified by the third one (weight loss). The second method (perforation) gives slightly varied measurements, however, probably due to the fact that the removal of matter by bombardment was not uniform on the bombarded area and that the determination of the time necessary for a total perforation therefore became a little arbitrary. However, the results are acceptable and reasonably verify the others.

Each point on Figures 7-2 and 7-3 represents an average of at least four measurements, the specimens having been, moreover, bombarded

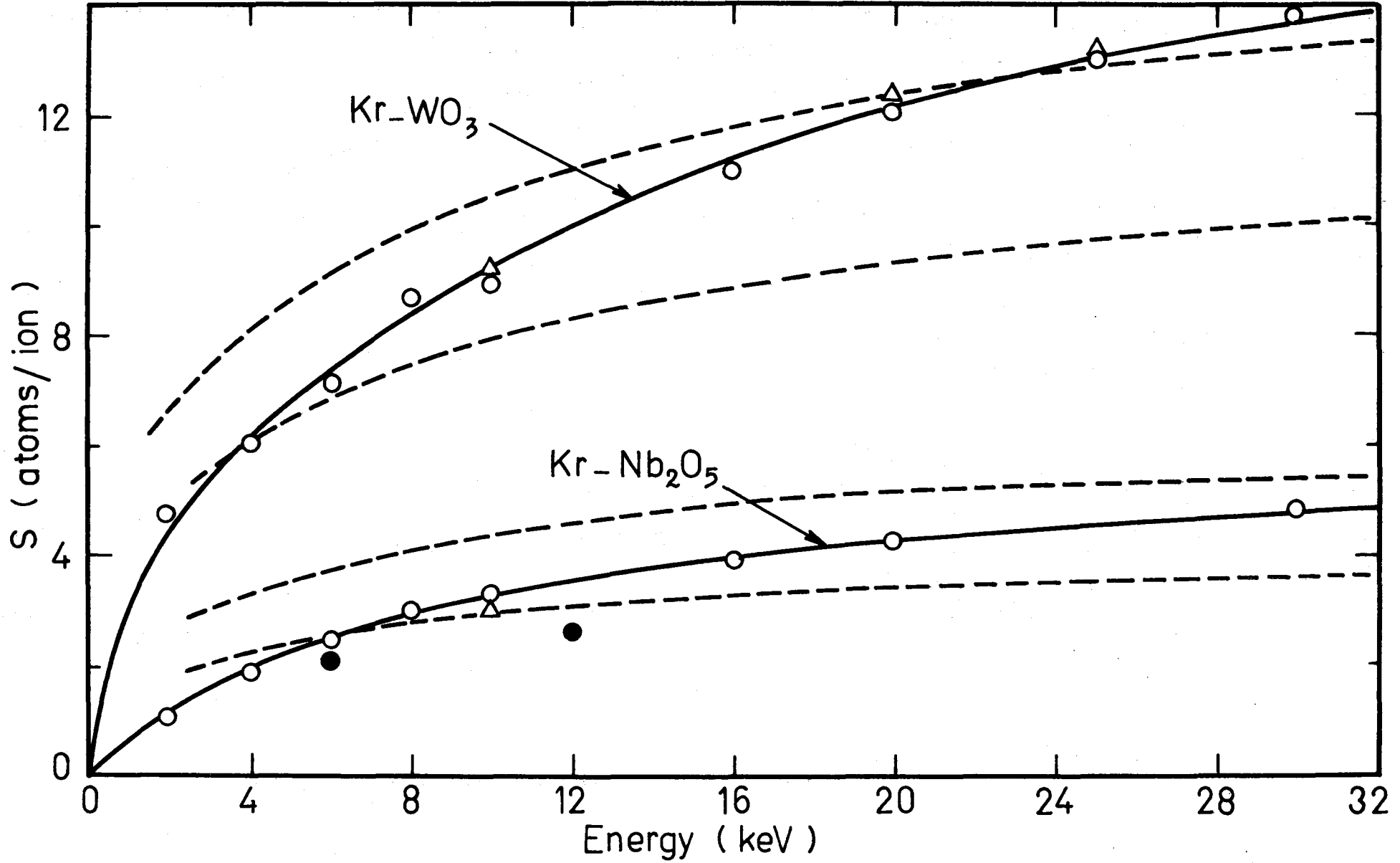

Figure 7-2 Sputtering coefficient for Kr bombardment of anodic Nb_2O_5 and WO_3. ○: obtained by the first method, ●: by the second method, △: by the third method, and ---: calculated from Sigmund's theory(9).

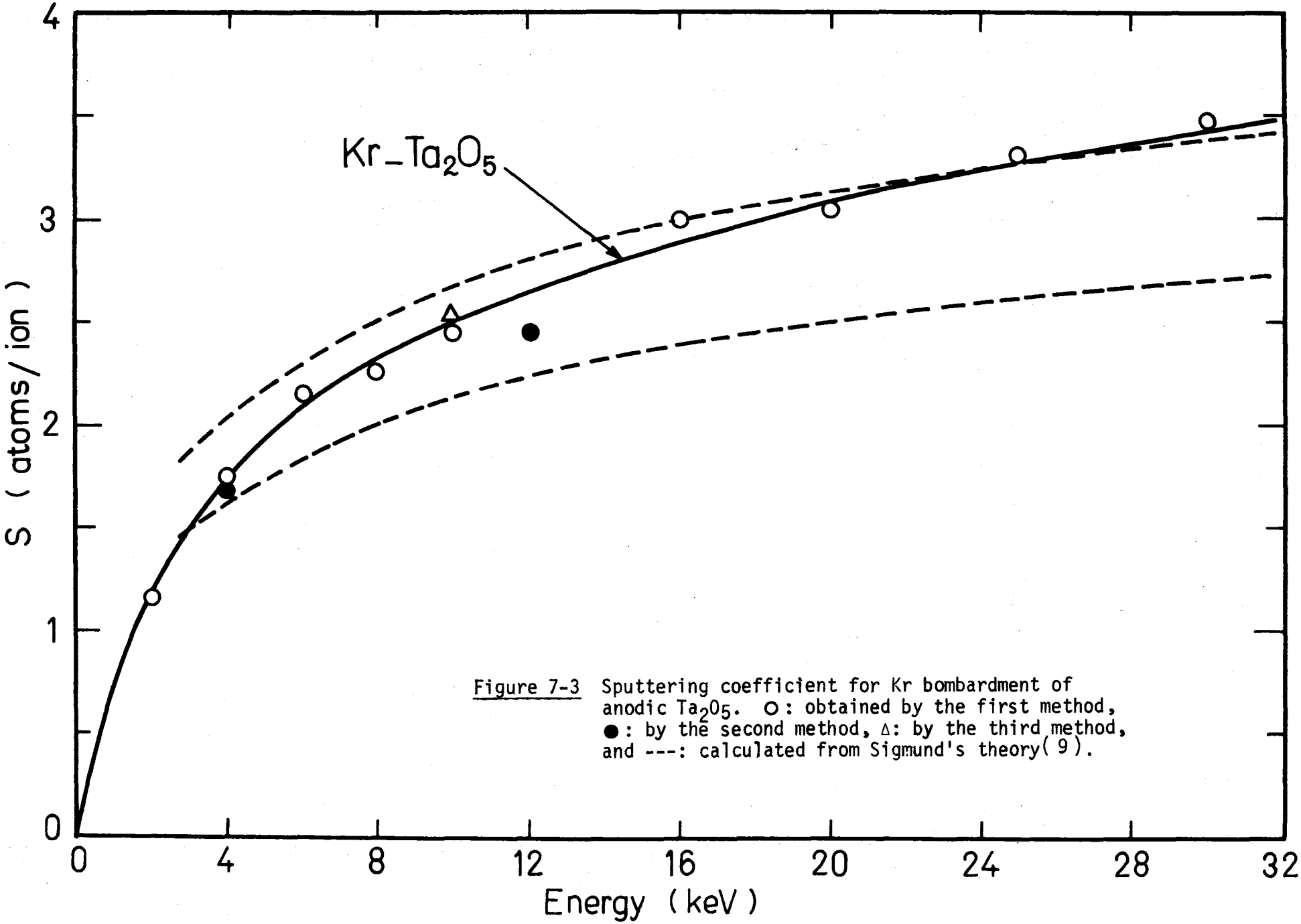

Figure 7-3 Sputtering coefficient for Kr bombardment of anodic Ta_2O_5. ○: obtained by the first method, ●: by the second method, △: by the third method, and ---: calculated from Sigmund's theory(9).

with different doses of Kr ions. Figure 7-4 shows that, with the methods used, the sputtering coefficients for the three oxides were dose-independent after averaging over all random fluctuations.

The general characteristic of S for these oxides is that S increases with the augmentation of E, but the rate of increase is smaller and smaller. This is, in effect, exactly the same behaviour as what one observes in the sputtering of metals[1-2,32].

We also note that the values of S for Kr-Nb_2O_5 and Kr-Ta_2O_5 are similar to those obtained for sputtering with Kr of Al_2O_3[6], TiO_2[6], and UO_2[4]. Only WO_3 is out of step, having value of S about three times larger.

7.3 RESULTS FOR OTHER OXIDES

The third method (weight loss) has been used to determine the sputtering coefficients for 10-keV Kr bombardment of MoO_3, SiO_2, V_2O_5, and ZrO_2. The results are summarized in Table 7-2. We see that MoO_3 and V_2O_5 can be classified in the same group, along with WO_3, which has a very high sputtering coefficient, whereas SiO_2 and ZrO_2 behave similarly to Al_2O_3, Nb_2O_5, Ta_2O_5, and TiO_2.

7.4 DISCUSSION

7.4.1 Comparison with the Theory of Rol et al.

The sputtering theory of Rol et al.[32-34] is based on the assumption that S is proportional to the energy dissipated in collisions near the target surface. As discussed in Section 3.2.2, Rol et al. have suggested treating the ion mean free path, λ, theoretically from the hard-sphere approximation. We would regard this as clearly incorrect for the

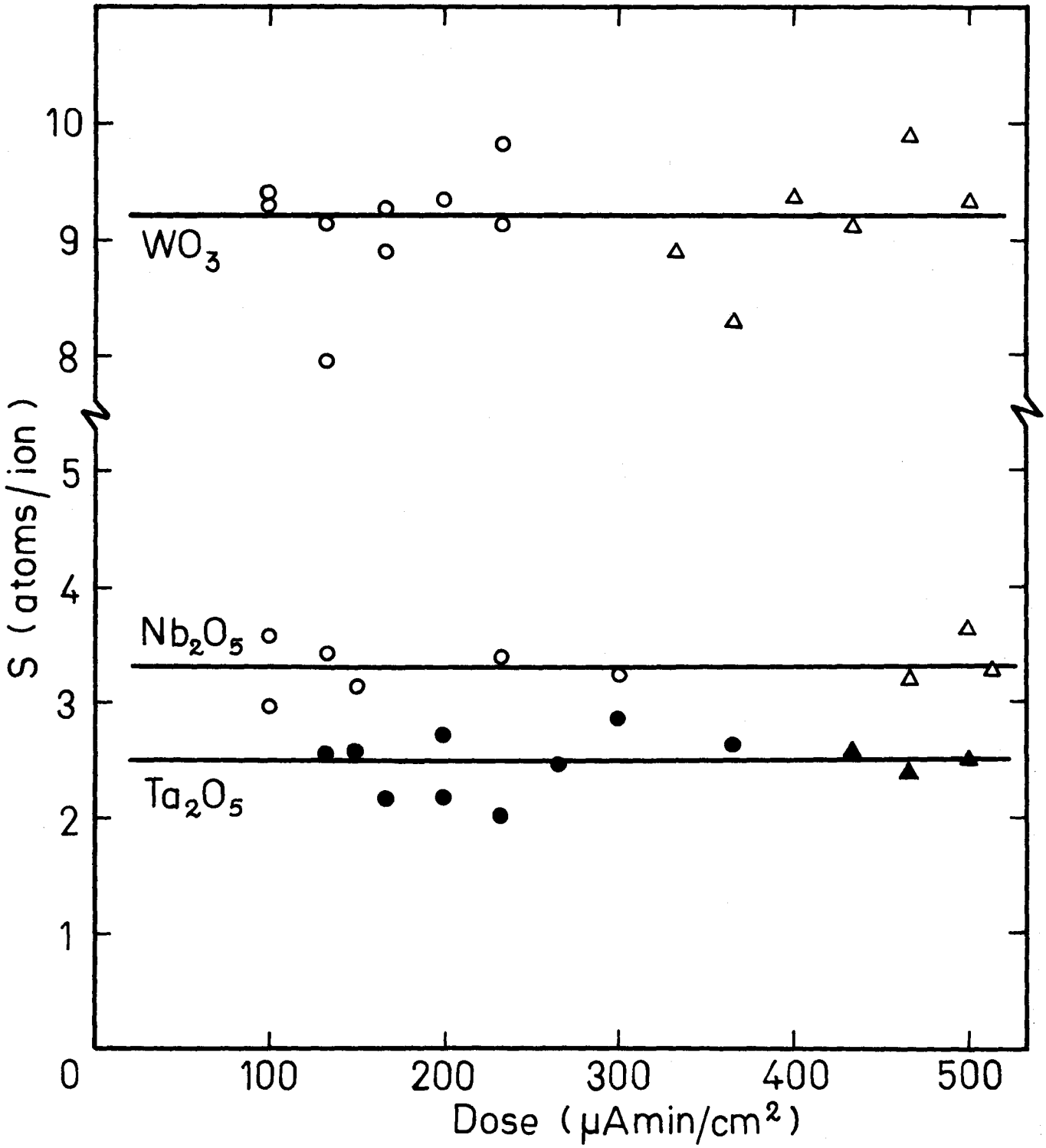

Figure 7-4 Variation of sputtering coefficient with dose for 10-keV Kr bombardment of Nb_2O_5, Ta_2O_5, and WO_3. ○,●: obtained by the first method; and △,▲: by the third method.

TABLE 7-2

Sputtering Coefficients for 10-keV Kr *

Oxides	$\bar{M}$	S(atoms/ion)
Al_2O_3	20	1.6 +
MoO_3	36	9.6
Nb_2O_5	38	3.4
SiO_2	20	4.2
Ta_2O_5	63	2.5
TiO_2	26.6	1.9 +
V_2O_5	26	12.7
WO_3	58	9.2
ZrO_2	41	2.8

* Determined generally by the third method (weight loss).

\+ After Kelly[6].

bombardment energies as used here. Rather one should use either power-law scattering with m=1/3 or else, as we shall employ here, range parameters as determined experimentally. Therefore, from equation (3-8a), the sputtering coefficient, S, can be written in the form:

$$S = \frac{\kappa}{R_m} E \tag{7-2}$$

where κ is an empirical constant and R_m is the experimental median range.

In order to demonstrate whether equation (7-2) can reasonably describe the sputtering process in Nb_2O_5, Ta_2O_5, and WO_3, as well as in Al_2O_3 and TiO_2 (Kelly[6]), the values of κ have been calculated. These values are included in Table 7-3 and we note that a good agreement between experimental results and equation (7-2) is demonstrated by virtue of the uncertainty in κ being small.

7.4.2 Comparison with Sigmund's Theory

As we have seen before, in Section 3.3, Sigmund's theory permits the sputtering coefficient to be calculated analytically. Equation (3-27) can be written as:

$$S = \frac{82\alpha Z_1 Z_2 M_1 s_n(\varepsilon)}{(Z_1^{2/3} + Z_2^{2/3})^{1/2} (M_1+M_2) U_o} = \alpha F(1,2)/U_o \tag{7-3}$$

where α is taken from Figure 3-4, $s_n(\varepsilon)$ is the reduced nuclear stopping cross section given in Table 3-1, and U_o is the surface binding barrier in units of Kcal/gram-atom. The dimensionless parameter ε, which is defined as in equation (2-40), can readily be obtained using Winterbon's tabulation[18].

In order to apply this theory to oxides under study, we make the approximation, as suggested by Sigmund (private communication), that

TABLE 7-3

Evaluation of κ in Equation (7-2)

Target	κ (Å/keV)	Ranges
Al_2O_3	13 ± 1	R_m for Kr - Al_2O_3 *
Nb_2O_5	25 ± 1	R_m for Kr - Al_2O_3 *
Ta_2O_5	13 ± 1	R_m for Kr-Ta_2O_5 and Rb-Ta_2O_5 +
TiO_2	15.5 ± 1.5	R_m for Kr - Al_2O_3 *
WO_3	48 ± 10	R_m for Kr - WO_3 ✓

* Domeij et al.[93]

\+ Pringle[85]

✓ this work (Table 9-2, column 2)

α can take the value appropriate for M_2 equal to the mean mass of the target (Table 7-2). The group of terms F(1,2) can be evaluated approximately by weighting the atomic fractions: for example, with Al_2O_3 we have:

$$F(1,2) = \frac{2}{5} F(Kr,Al) + \frac{3}{5} F(Kr,O) \qquad (7\text{-}4)$$

Finally, since U_o is in general not well defined for an oxide, we consider it as an unknown. The values chosen for U_o are included in Table 7-4 .

The values of U_o are comparable to within a factor of two to those typically found for atomization (Table 7-4), at least for the case of Al_2O_3, Nb_2O_5, SiO_2, Ta_2O_5, TiO_2, and ZrO_2 which have low sputtering coefficients. There is, however, no agreement between U_o and heat of atomization for the other oxides: MoO_3, V_2O_5, and WO_3, whose sputtering coefficients are in the order of three times larger.

7.4.3 Possible Contribution of Volatility to Sputtering

The large discrepancy in the values of S for the two groups of oxides can be rationalized in a simple way, using an argument based on the volatile nature, together with the stability of gaseous multimers, in the case of MoO_3, V_2O_5, and WO_3.

The contribution of evaporation from thermal spikes to the sputtering process, as suggested by Thompson and Nelson[96], could be very important in the case of volatile oxides with multimeric gas molecules. Thus, the loss of target material might have resulted from both a single-atom-ejection process, which was due to momentum transfer, and from an evaporation process due to local heating by ion impact. The formation

TABLE 7-4

Evaluation of U_o in Equation (7-3)

Target	α[a]	U_o (Kcal/gram-atom)	Heat of Atomization (Kcal/gram - atom)
Al_2O_3	0.19	225 - 275	146[c]
MoO_3	0.21	40 - 55 [b]	140[d]
Nb_2O_5	0.21	100 - 150	160[c]
SiO_2	0.19	70 - 95 [b]	172[d]
Ta_2O_5	0.25	200 - 250	166[c]
TiO_2	0.20	200 - 250	151[d]
V_2O_5	0.20	25 - 35 [b]	131[d]
WO_3	0.24	45 - 60	146[d]
ZrO_2	0.22	150 - 200 [b]	173[c]

[a] Taken from Figure 3-4.

[b] Calculated from sputtering coefficient for 10-keV Kr but allowing for 15% errors.

[c] After Vijh[94].

[d] Calculated according to Vijh's suggestion[94], using thermodynamical parameters of Kubaschewski et al.[95].

of polymolecular species has been revealed by mass spectroscopy, to be dominant in the evaporation of MoO_3, V_2O_5, and WO_3. For example, the tendency to associate was found to be very strong in the case of MoO_3 and WO_3 where the trimer (i.e. $(MoO_3)_3$ and $(WO_3)_3$) represents more than 80% of the vapor species[97].

Although local heating by ion impact has a minor effect on the sputtering of metals at room temperature[96], one should not neglect its contribution to the sputtering of these oxides, which have considerably lower thermal conductivity. Further study on the temperature dependence of the sputtering coefficient of oxides would therefore be required in order to clarify the above-mentioned influence of the evaporation process on the sputtering mechanism.

7.4.4 Effect of an Oxide Layer on a Bombarded Metal

A comparison between S for Ta_2O_5 and WO_3 and S for the corresponding metals is given in Figures 7-5 and 7-6. We note, in case of oxides, that S, when expressed in units of atoms/ion, is larger than S of metals which are bombarded with the same ions (Kr). At first sight, one might think that an oxide layer would enhance the rate of removal of metal. This conclusion, however, is not correct. When we express the sputtering coefficient S in units of atoms of metal per ion (see solid lines indicated by "Kr-Ta_2O_5 x 2/7" and "Kr-WO_3 x 1/4"), we clearly see that S for the oxide is smaller than the value for the corresponding metal, and that, in reality, the presence of an oxide layer (Ta_2O_5 or WO_3) constitutes a protective action against sputtering. This conclusion is similar to that obtained for Al_2O_3 on Al or TiO_2 on Ti[6]; the protective action, however, is not as large as previously believed[98].

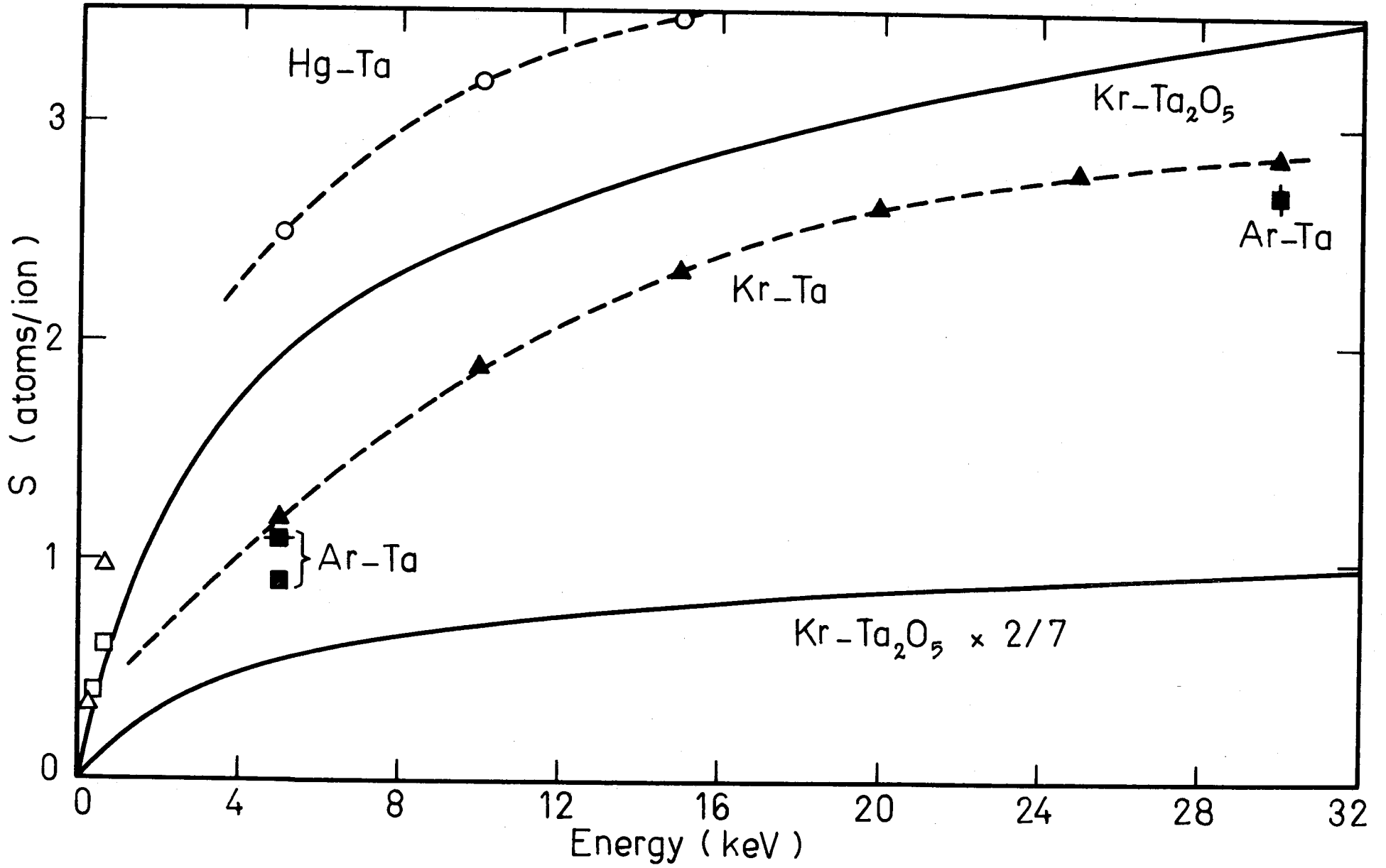

Figure 7-5 Comparison of S for various ions on Ta_2O_5 and Ta. The references are following: ○: 1, —: this work; △: 99; ▲: 100; □: 101; ■: 98; ⊣■⊢: 102; and ⊣■⊢: 103. The line marked with "Kr-Ta_2O_5 x 2/7" gives S in units of atoms of metal per ion.

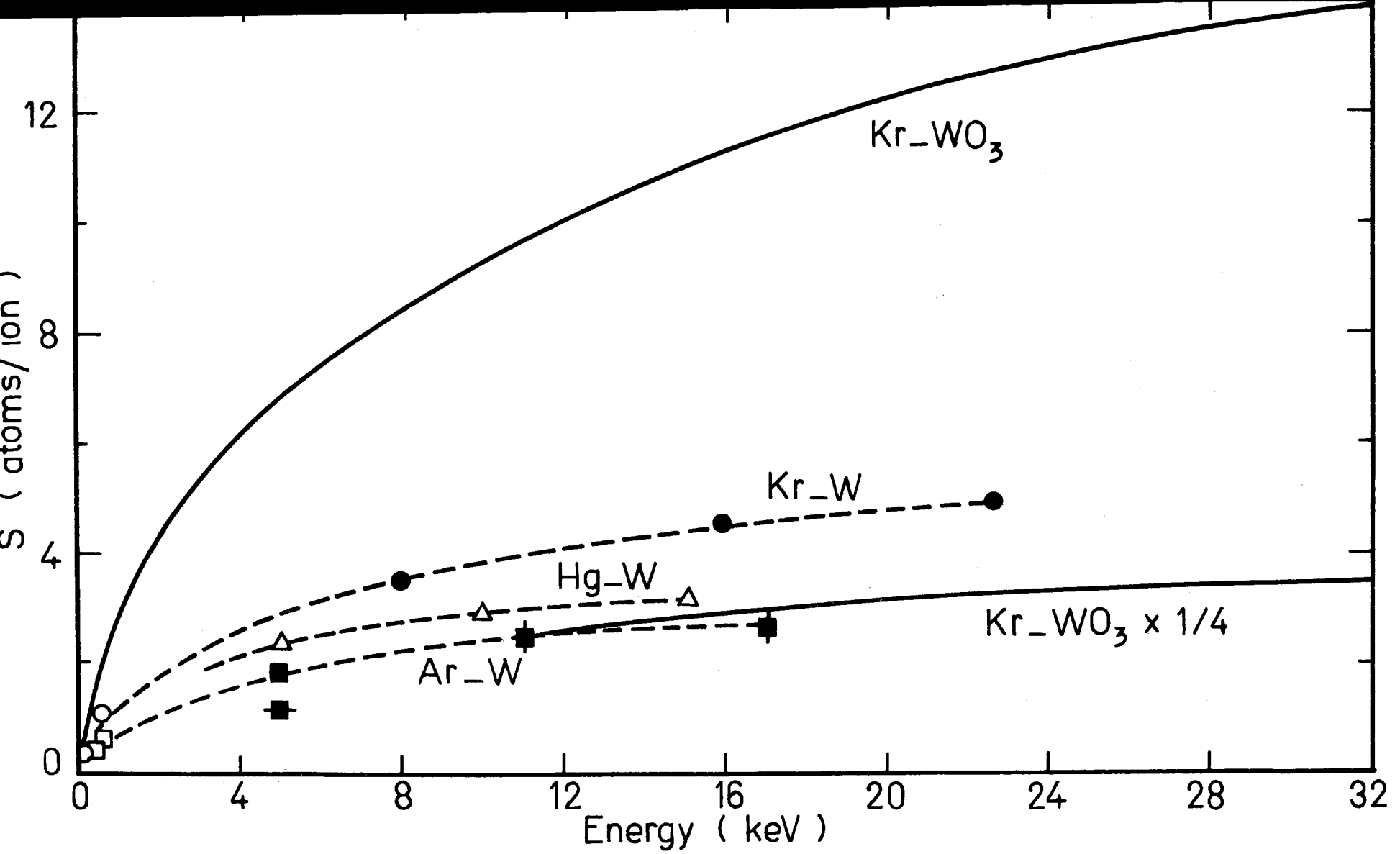

Figure 7-6 Comparison of S for various ions on WO_3 and W. The references are following: —: this work; ○: 99; ●: 104; △: 1; □: 101; ■: 98; —■—: 102; and ■: 105. The line marked with "Kr-WO_3 x 1/4" gives S in units of atoms of metal per ion.

CHAPTER 8

HIGH-DOSE DEPTH DISTRIBUTIONS IN ANODIC Al_2O_3, Nb_2O_5, AND WO_3

8.1 TECHNIQUES

8.1.1 Depth-Distribution Experiments

In brief, the experimental method consists of:

(a) formation of thin oxide films of known thicknesses;

(b) bombardment of the oxide films with radioactive Kr ions at different doses;

(c) counting the target activity after bombardment;

(d) removal (partial or complete) of the oxide layers; and

(e) counting the residual target activity after removal of oxide.

The technique is, in general, therefore closely similar to that developed previously by Domeij et al.[93].

Oxide Preparation: Al, Nb, and W foils were anodized in suitable electrolytes at different voltages from 1 to 12 volts, with 1-volt increments. The forming electrolyte and the thickness of Al_2O_3 films have been mentioned in Table 6-1. The Nb_2O_5 was formed in electrolytes (1) or (2) of Table 6-1 and the oxide thickness can be estimated from Figures 6-1 or 6-2. The thickness of WO_3 films formed in KNO_3-HNO_3 electrolyte is given by Figure 6-3.

Bombardment: Most of the bombardments were carried out at 10 keV with Kr containing Kr^{85}. The ion dose was determined by measuring the

the ionic current, bombardment time, and implanted area.

Activity Counting: The target activity was measured using a β-counter which consists of a Philips GM probe PW 4351 and a Philips PW 4237 scalar with high voltage supply PW 4290. The GM probe had a halogen gas as quenching agent and a mica end-window. The penetration depths involved in these range studies are much less than 1 mg/cm^2. For such a thin layer of absorbing material, the absorption corrections to the observed β-counting rate were found to be less than 1% and could therefore be neglected[81].

Transmission Technique: After bombardment and activity counting, the oxide layer (Al_2O_3 and WO_3)was completely removed, and the activity was then counted again. The ratio of two activities determines the fraction of the incident ions which was transmitted through the thin anodic film of known thickness. For high-dose bombardments, data points have been corrected by means of equation 7-1 for the reduction of the oxide-film thickness which necessarily results from sputtering during labeling. Typical values of the correction are shown in Table 8-1.

TABLE 8-1

Examples of the Correction for 10-keV Kr Sputtering

Substance	Anodic Voltage	Oxide thickness before bombardment	Bombardment dose	Thickness removed by sputtering (from eq(7-1b))	Oxide thickness after bombardment
Al_2O_3	6 volts	118 Å	4×10^{15} ions/cm^2	6 Å	112 Å
Nb_2O_5	6	208[+]	4×10^{15}	17	191
WO_3	6	157	4×10^{15}	48	109

[+] From Figure 6.1

Slow Dissolution Technique: Anodic films of Nb_2O_5 can be slowly dissolved, step by step if desired, in a solution of 40% HF saturated with NH_4F (or in 68% HNO_3 solution), while anodic WO_3 dissolves controledly in an aqueous solution of 0.1 g/liter KOH (see Table 6-2). After each dissolution step, specimens were immediately washed in distilled water and cleaned with alcohol, and the dissolution time and the residual activity were carefully noted. Since the oxides dissolve in these solutions faster than the metals, the activity-versus-time curves present a "knee" and then a plateau (with WO_3) or region of reduced slope (with Nb_2O_5), corresponding to the end of the dissolution process. Equation 7-1 has again been used to correct the oxide thickness for sputtering and determine the thickness of the oxide film remaining after high-dose bombardment. Knowing the total thickness and the time required for dissolving it, we could therefore estimate the rate of dissolution.

Figures 8-1 to 8-3 show typical activity-versus-time curves for WO_3 and Nb_2O_5 bombarded with 10- keV Kr, the "knees", which correspond to the oxide-metal interface, serving to calibrate the dissolution rate of the oxides.

Figures 8-4 to 8-6 illustrate the variation of the rate of dissolution of anodic WO_3 and Nb_2O_5 in the above-mentioned solvents, as a function of 10-keV Kr doses.

A characteristic of the dissolution of these oxides is that the dissolution rate decreases with increasing bombardment dose, i.e. there is a radiation-retarded solubility. Such a retardation has also been observed in case of Al_2O_3 and Ta_2O_5 bombarded with energetic electrons[106], though is not the usual result. Normally, bombardment enhances the

Figure 8-1 Activity-versus-time curves serving to determine the rate of dissolution of anodic WO_3 in an aqueous solution of 0.1 g/liter KOH

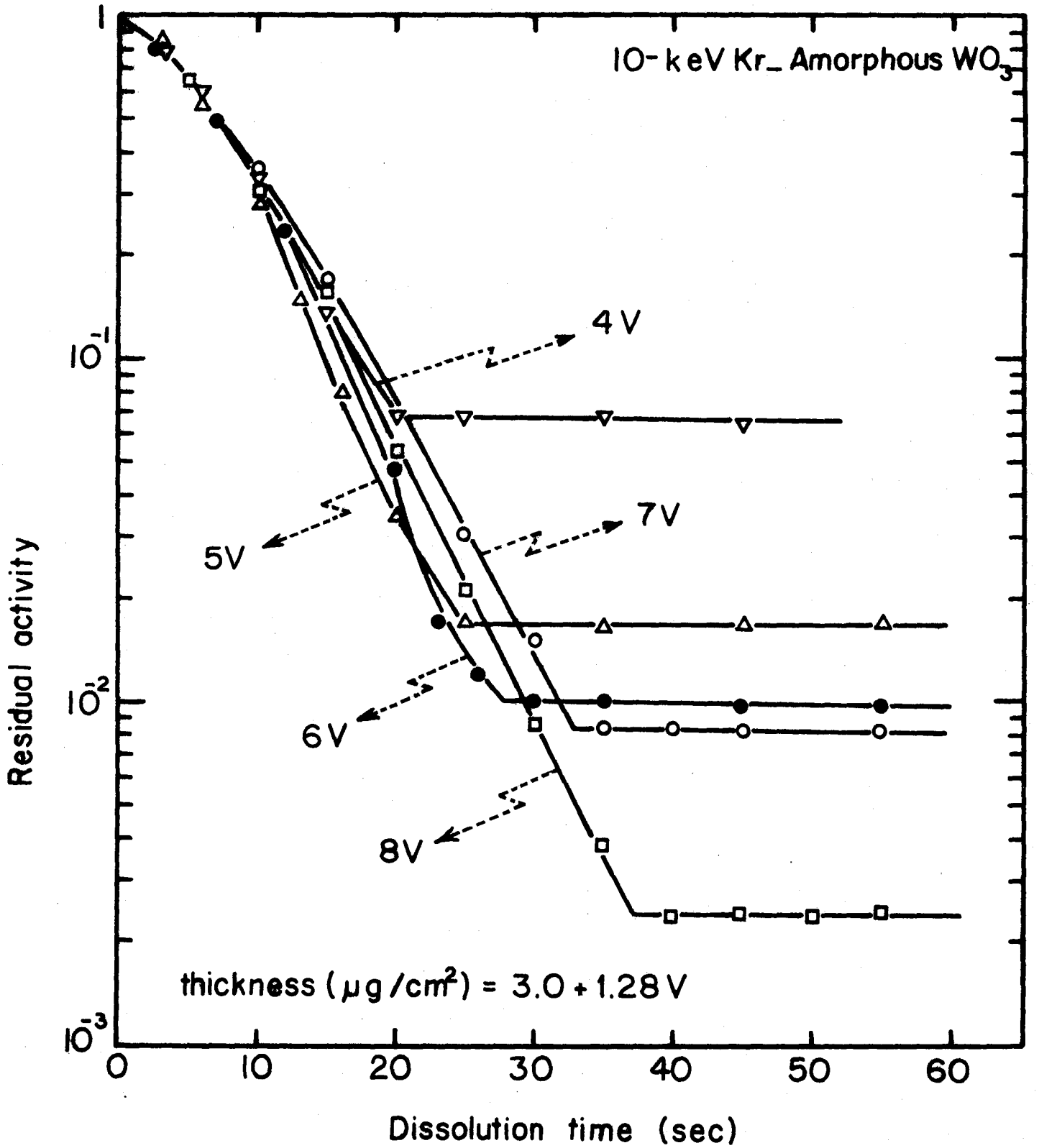

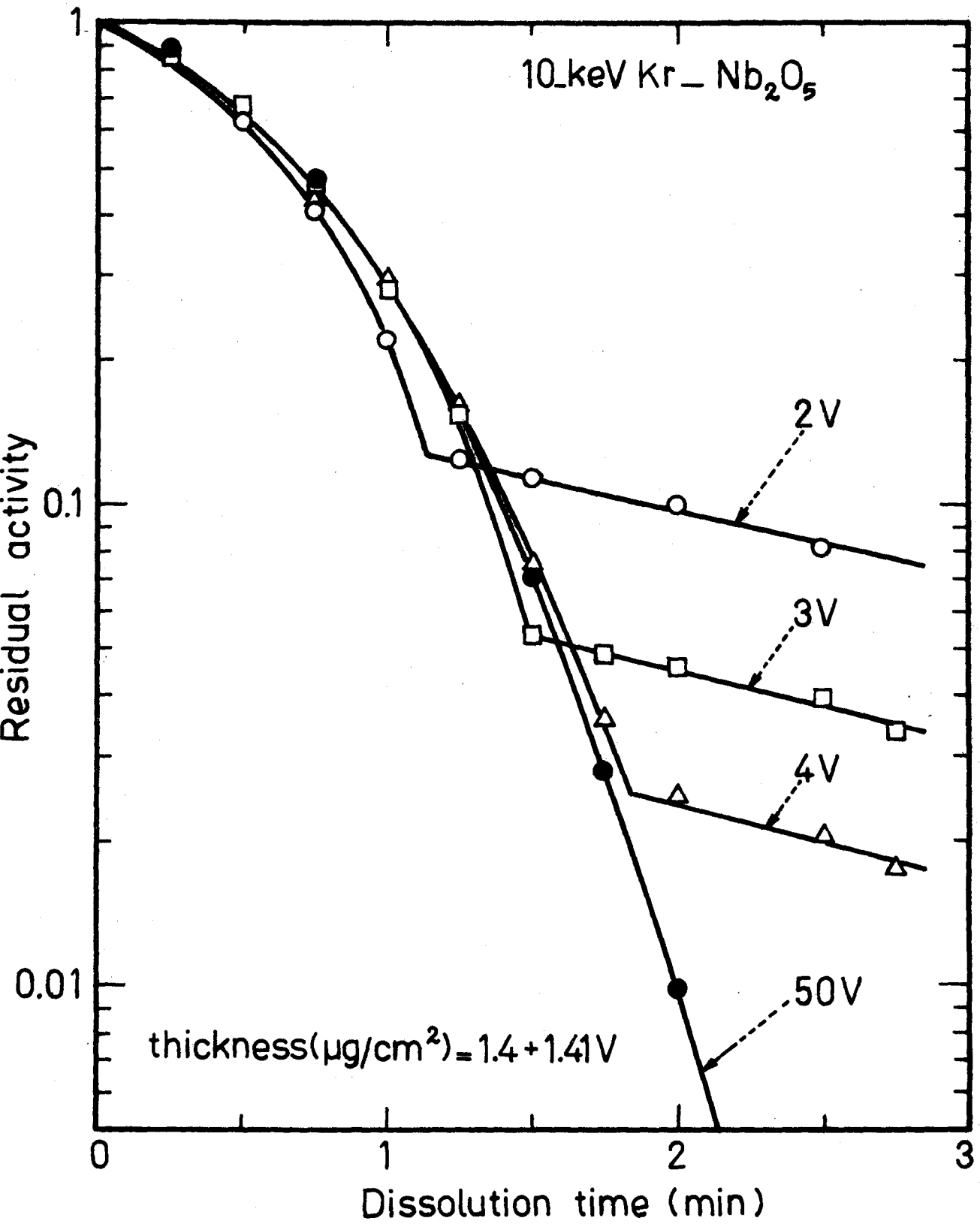

Figure 8-2 Activity-versus-time curves serving to determine the rate of dissolution of anodic Nb_2O_5 in a solution of 40% HF saturated with NH_4F.

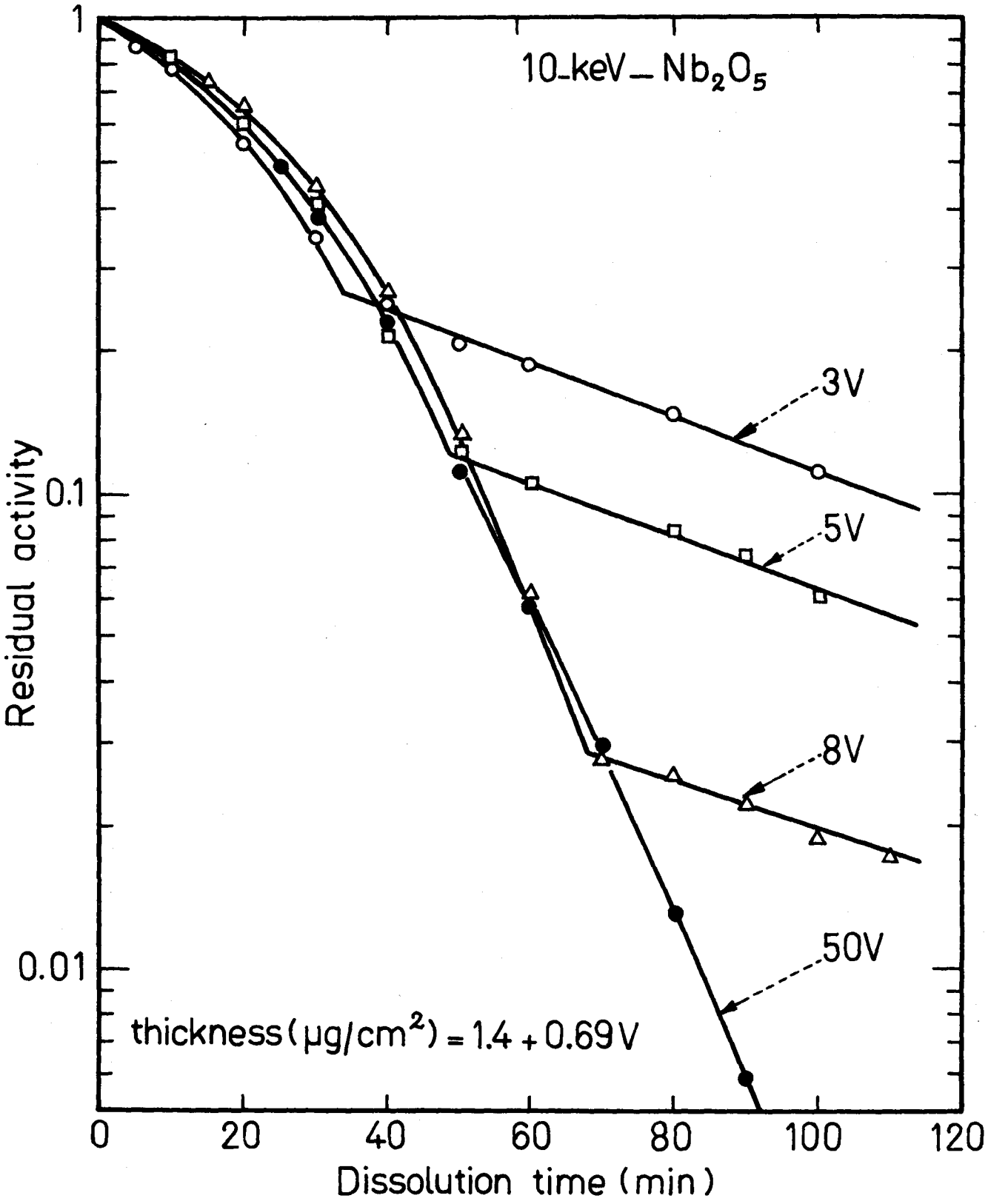

Figure 8-3 Activity-versus-time curves serving to estimate the rate of dissolution of anodic Nb_2O_5 in a 68% HNO_3 solution held at 120°C.

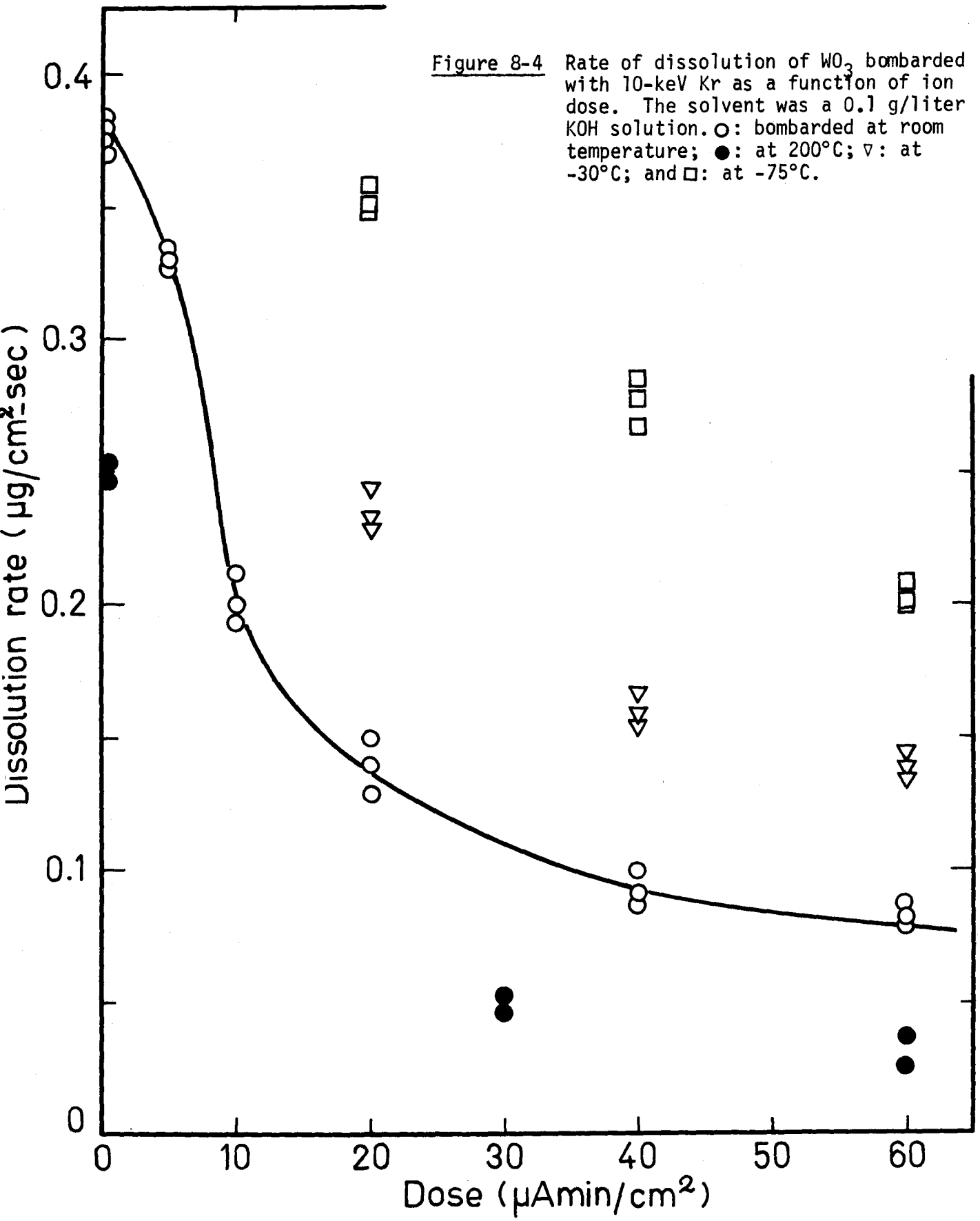

Figure 8-4 Rate of dissolution of WO_3 bombarded with 10-keV Kr as a function of ion dose. The solvent was a 0.1 g/liter KOH solution. ○: bombarded at room temperature; ●: at 200°C; ▽: at -30°C; and □: at -75°C.

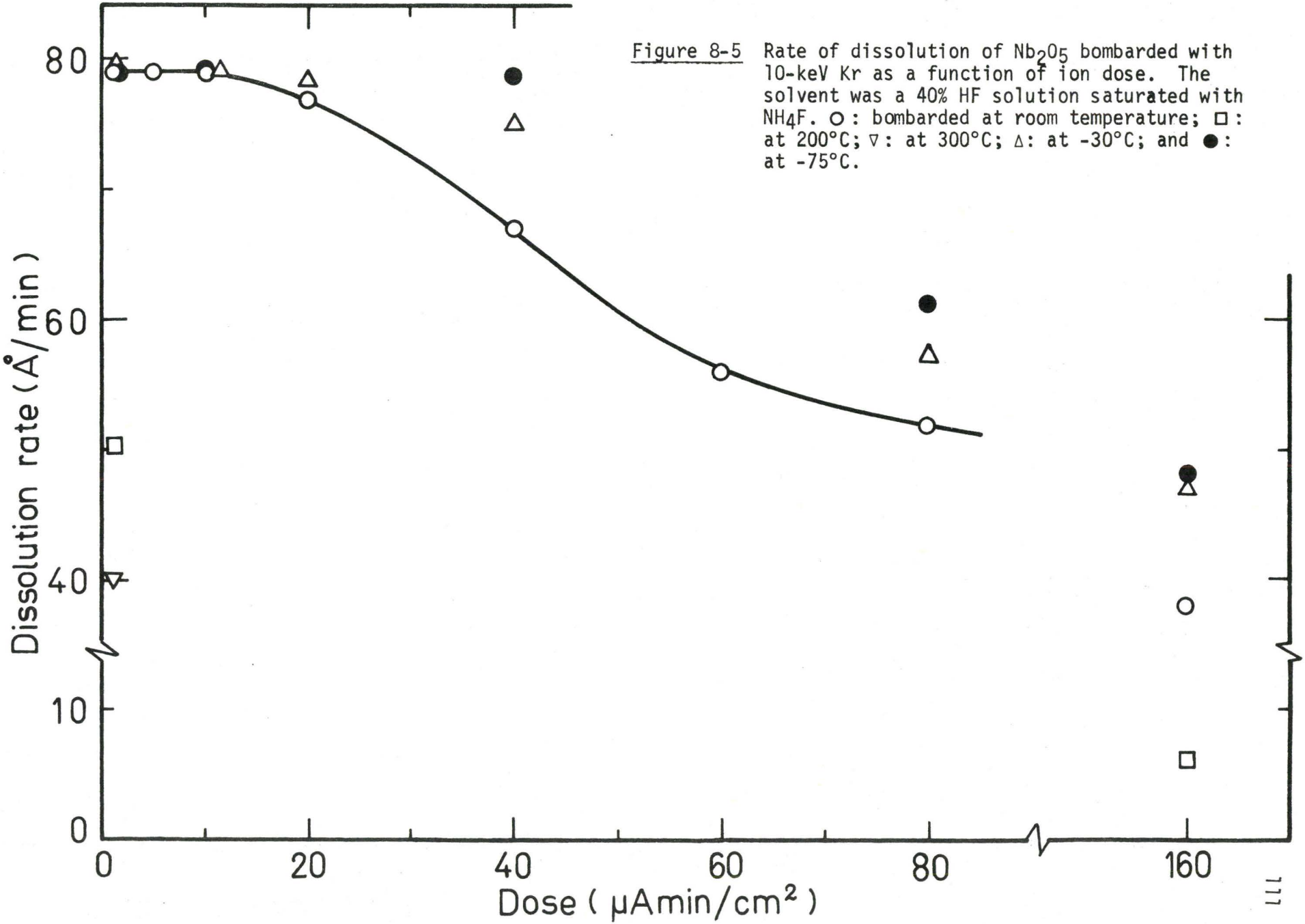

Figure 8-5 Rate of dissolution of Nb_2O_5 bombarded with 10-keV Kr as a function of ion dose. The solvent was a 40% HF solution saturated with NH_4F. ○ : bombarded at room temperature; □ : at 200°C; ▽ : at 300°C; △ : at -30°C; and ● : at -75°C.

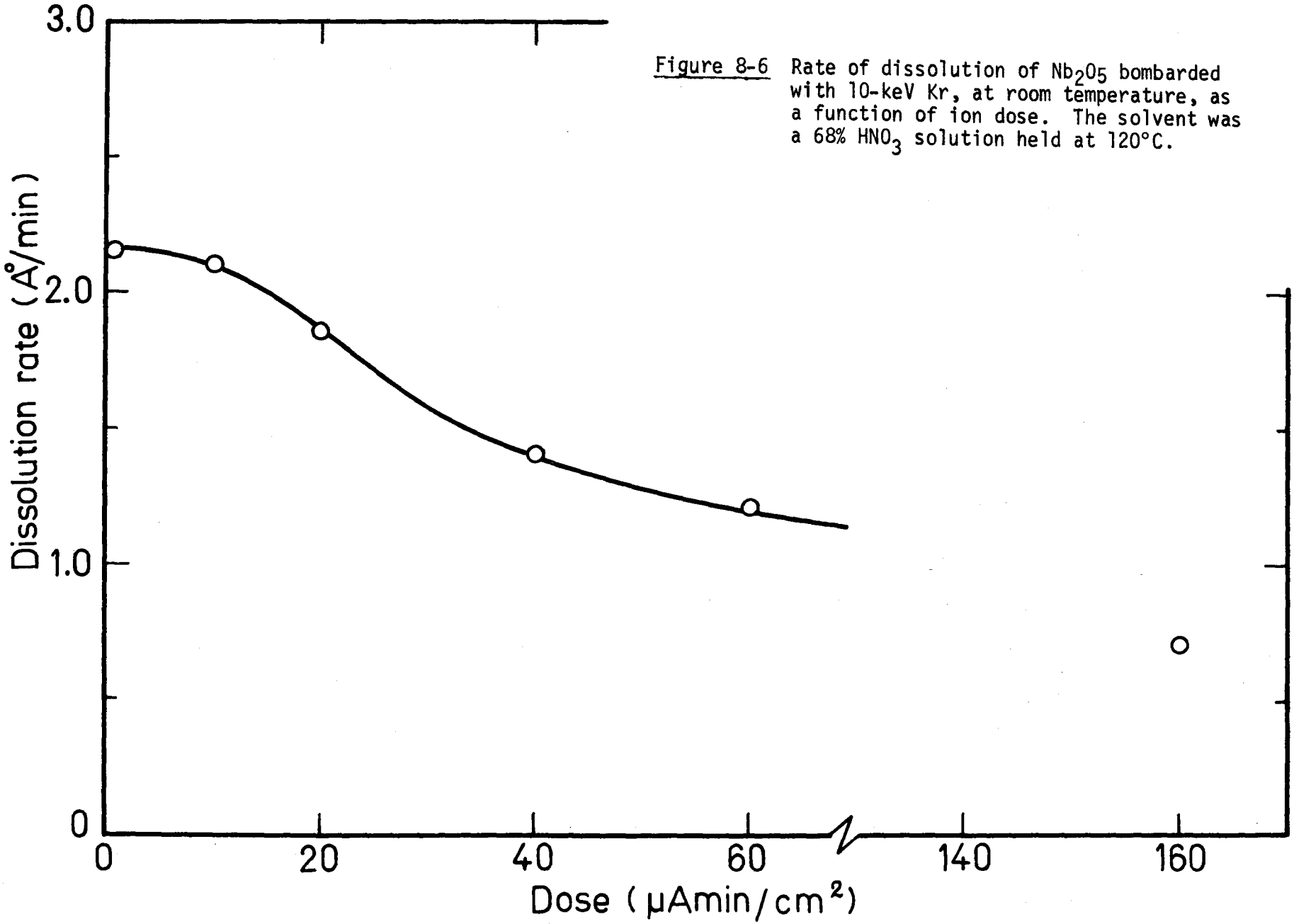

Figure 8-6 Rate of dissolution of Nb_2O_5 bombarded with 10-keV Kr, at room temperature, as a function of ion dose. The solvent was a 68% HNO_3 solution held at 120°C.

solubility[106-111].

8.1.2 Gas-Release Experiments

Thick films of Al_2O_3, Nb_2O_5, Ta_2O_5, WO_3 and ZrO_2, which were formed by anodizing at ∿ 100 volts, foils of polycrystalline Au, Si, and Pt, and KCl, which was prepared by cleavage from large boules, were Tessla-labeled with ∿ 1-keV Kr^{85} using the apparatus as described in Section 6-5.

Gas-release spectra were obtained with the usual technique[112-113], the basis of which is that He flowing at a constant rate is passed over the sample and through a G.M. counting chamber while the sample is heated linearly at 25°C/min. The specimen was heated first, in the chamber 2 (see Figure 6-7), to room temperature, and then, with the specimen transferred to another gas-release chamber, to 1000°C.

The rate of gas-release and the temperature of the specimen were recorded simultaneously by a 2-channel recorder.

8.2 RESULTS

8.2.1. Room-Temperature Bombardment

Figures 8-7 to 8-12 show Kr depth-distributions in Al_2O_3, Nb_2O_5, and WO_3. Distribution profiles in Figures 8-7 and 8-12 were obtained using the transmission technique. The slow-dissolution technique, on the other hand, was used to get the other curves. Figures 8-8 and 8-9 show a typical agreement between results obtained for Nb_2O_5 bombarded with 10-keV Kr, using two different solvents. However, the solvent containing HF and NH_4F was preferred in this work because of clearer appearance of a dissolution end-point at oxide-metal interface and the more reasonable rate of dissolution it gives. Similarly, Figure 8-10 shows that the

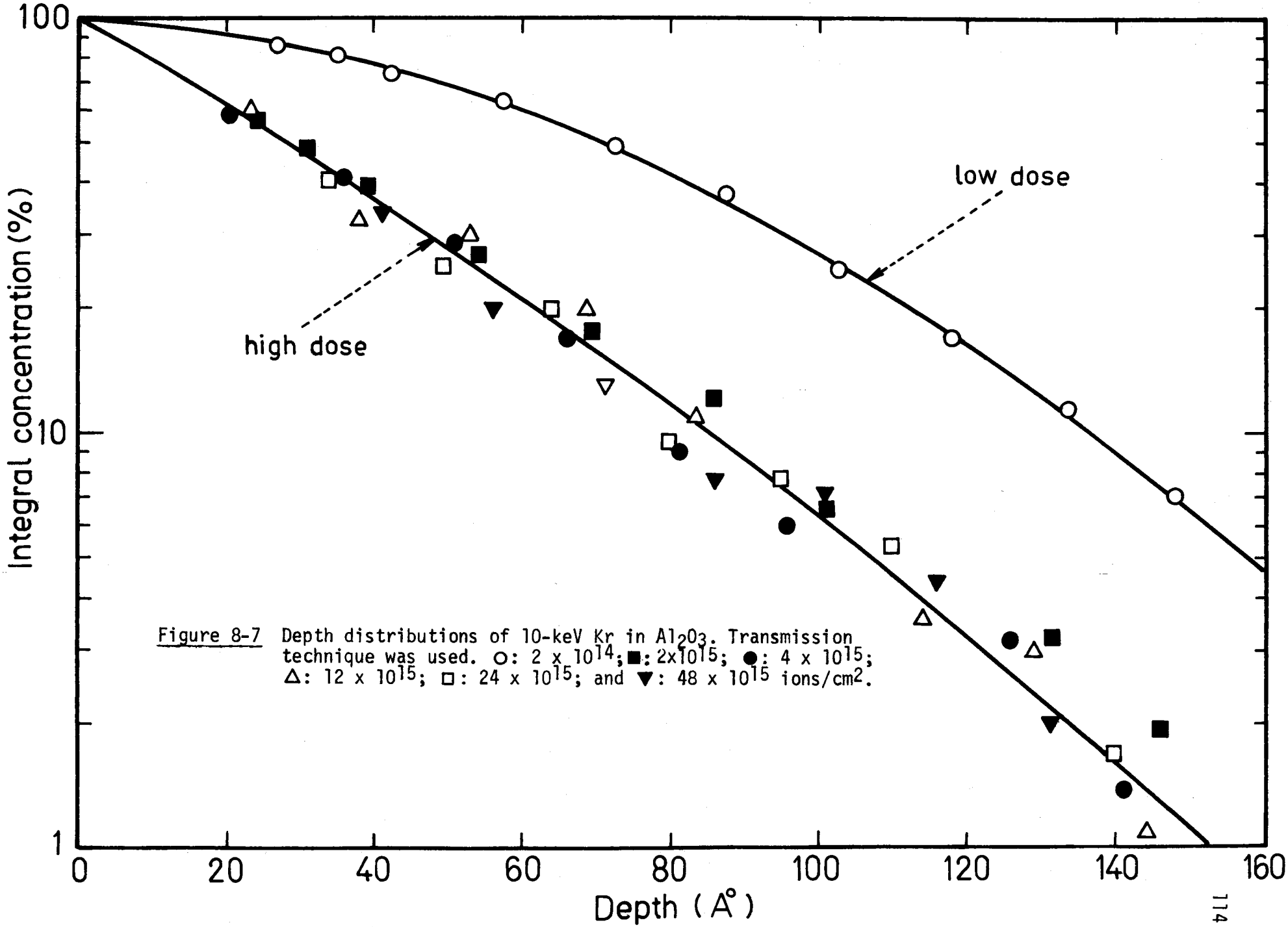

Figure 8-7 Depth distributions of 10-keV Kr in Al_2O_3. Transmission technique was used. ○: 2×10^{14}; ■: 2×10^{15}; ●: 4×10^{15}; △: 12×10^{15}; □: 24×10^{15}; and ▼: 48×10^{15} ions/cm^2.

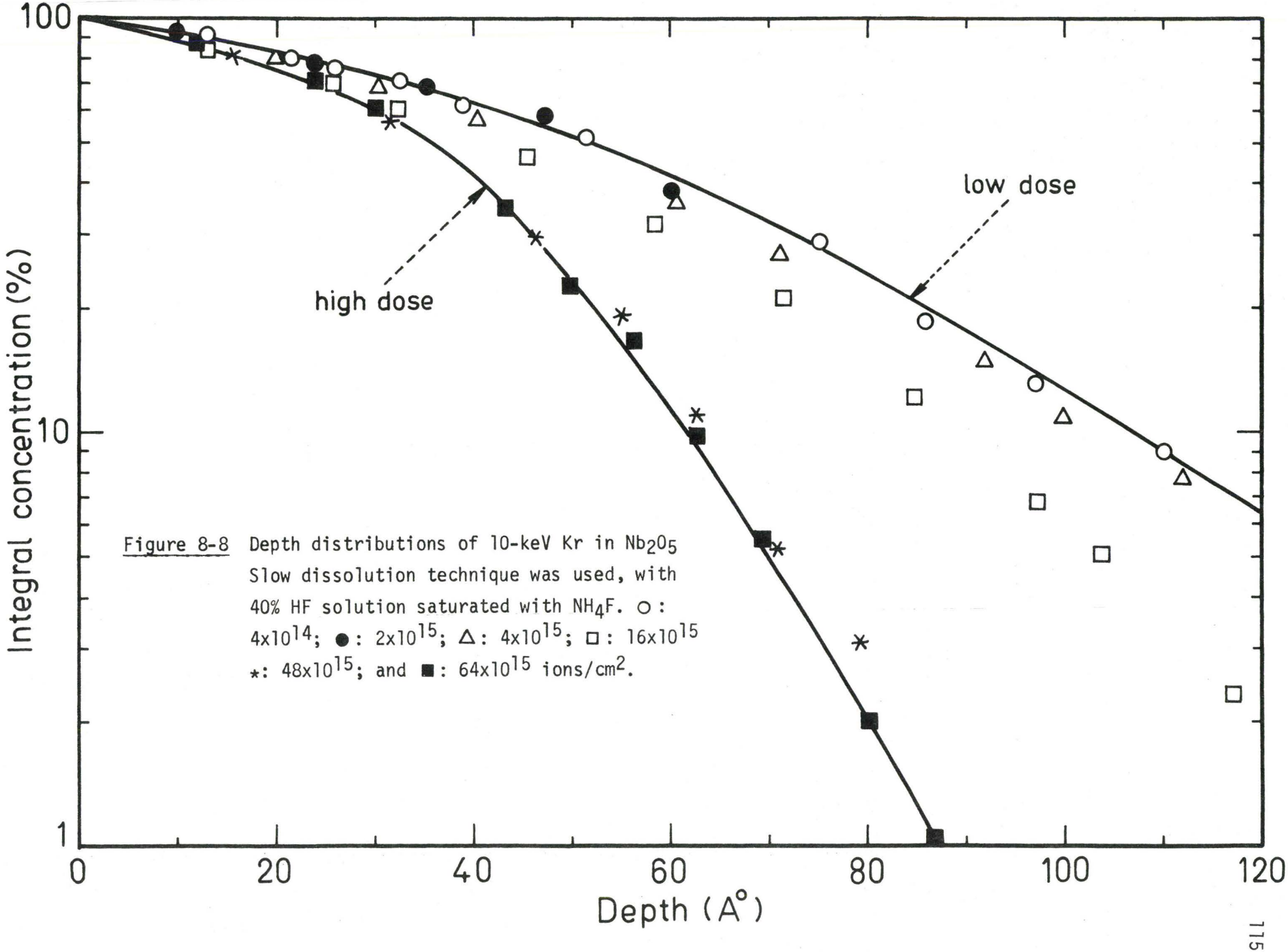

Figure 8-8 Depth distributions of 10-keV Kr in Nb_2O_5 Slow dissolution technique was used, with 40% HF solution saturated with NH_4F. ○: $4x10^{14}$; ●: $2x10^{15}$; △: $4x10^{15}$; □: $16x10^{15}$ ⋆: $48x10^{15}$; and ■: $64x10^{15}$ ions/cm^2.

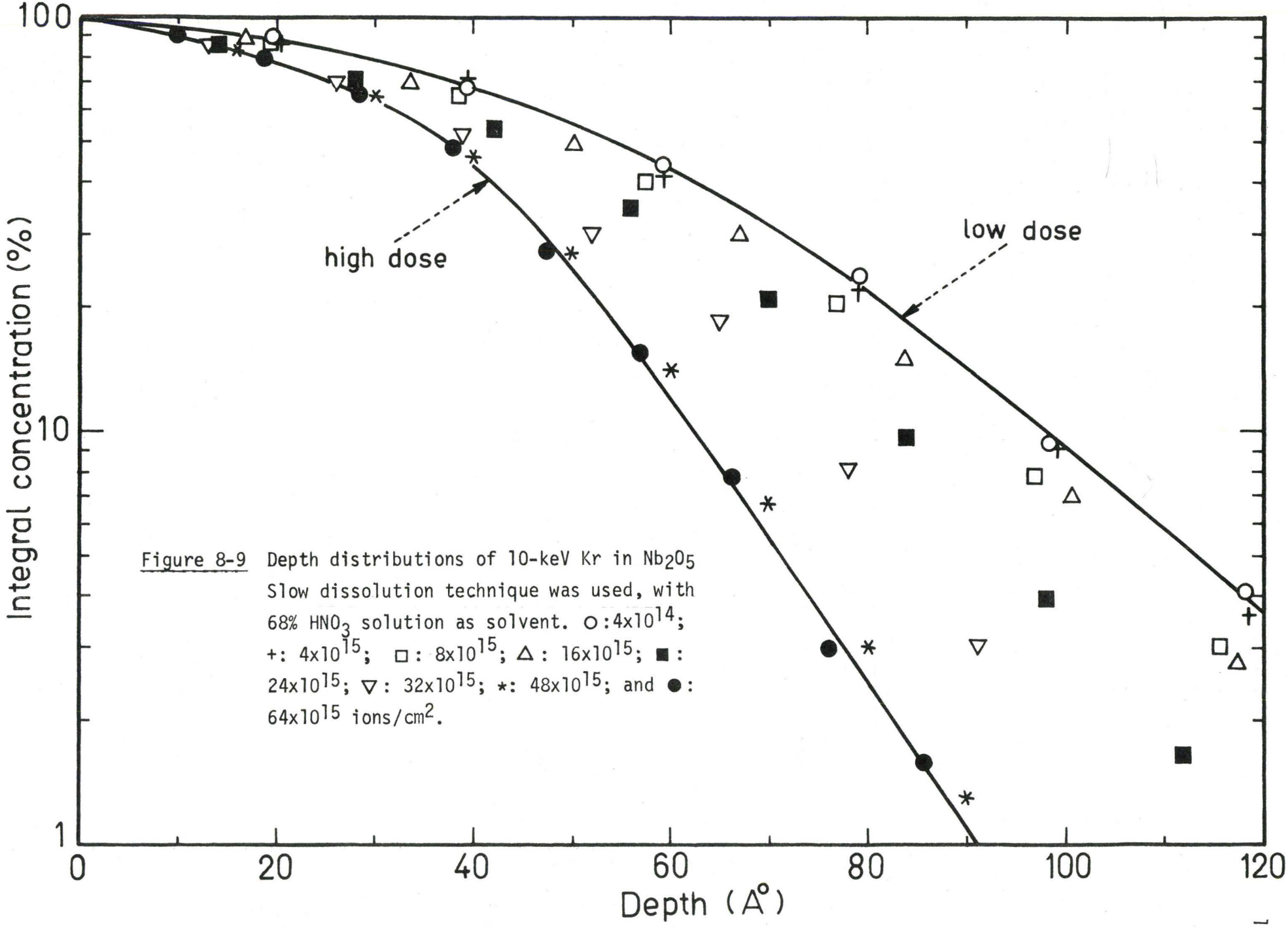

Figure 8-9 Depth distributions of 10-keV Kr in Nb_2O_5 Slow dissolution technique was used, with 68% HNO_3 solution as solvent. ○:$4x10^{14}$; +: $4x10^{15}$; □: $8x10^{15}$; △: $16x10^{15}$; ■: $24x10^{15}$; ▽: $32x10^{15}$; *: $48x10^{15}$; and ●: $64x10^{15}$ ions/cm^2.

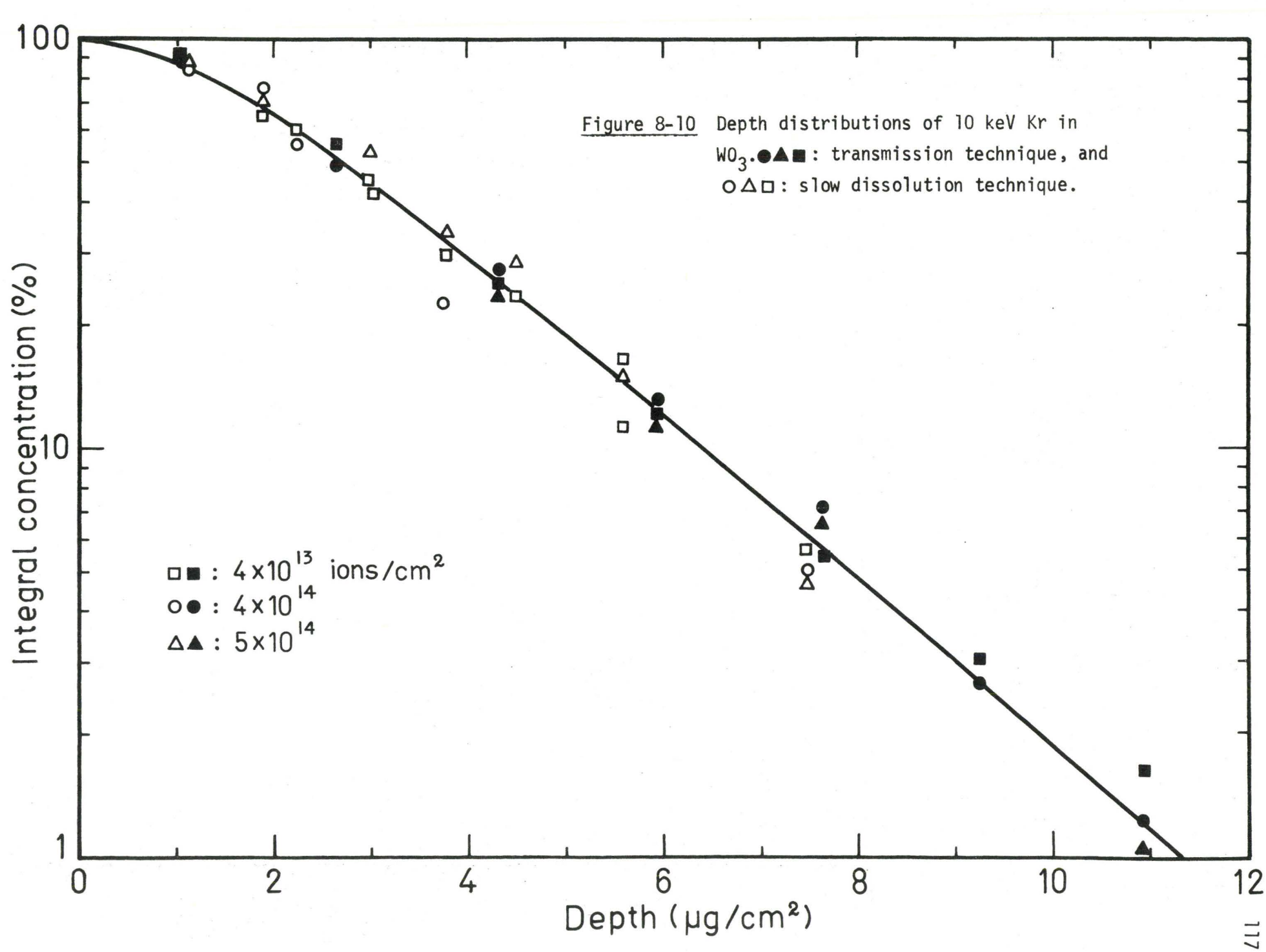

Figure 8-10 Depth distributions of 10 keV Kr in WO_3. ●▲■ : transmission technique, and ○△□ : slow dissolution technique.

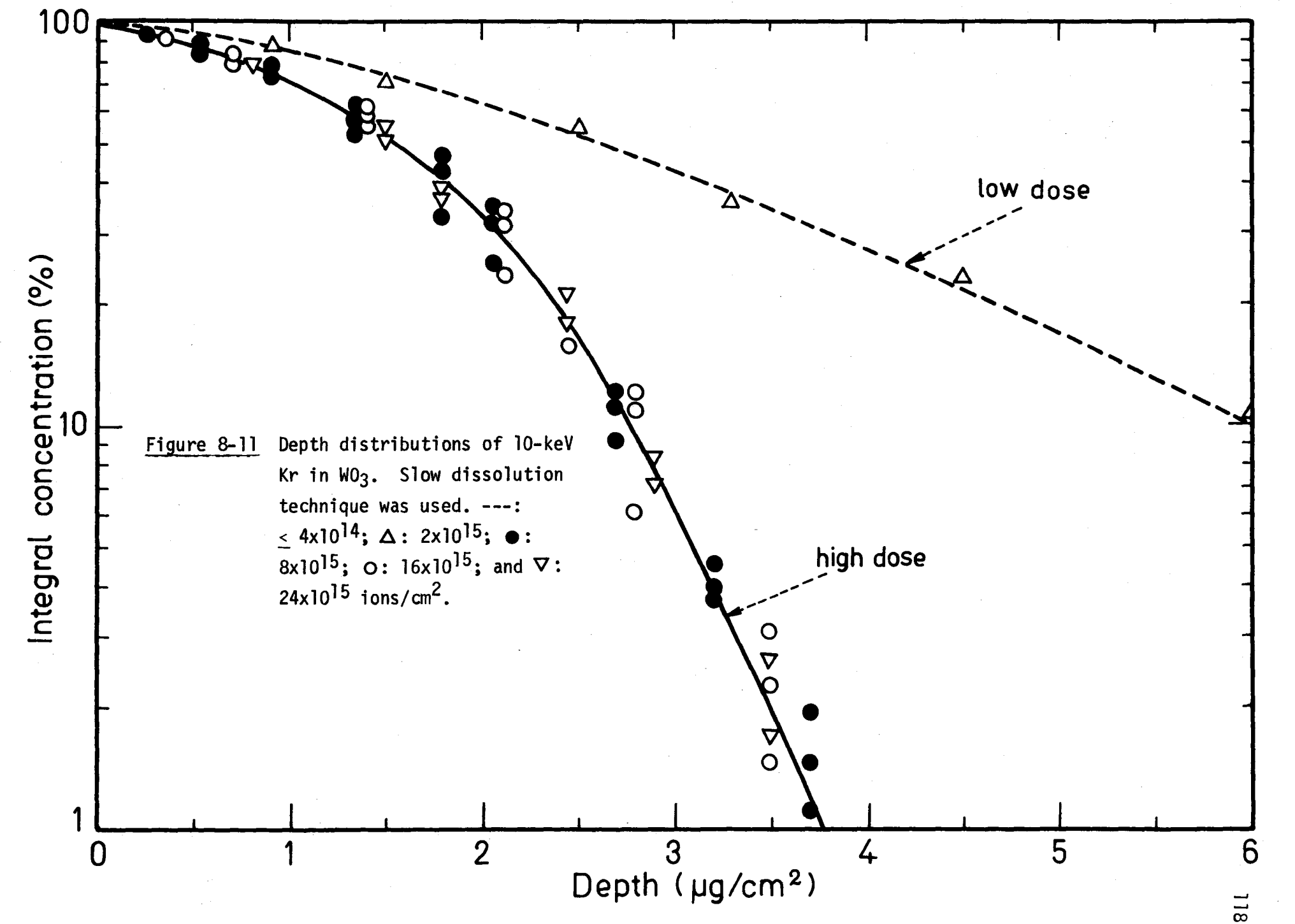

Figure 8-11 Depth distributions of 10-keV Kr in WO_3. Slow dissolution technique was used. ---: $\leq 4\times10^{14}$; △: 2×10^{15}; ●: 8×10^{15}; ○: 16×10^{15}; and ▽: 24×10^{15} ions/cm^2.

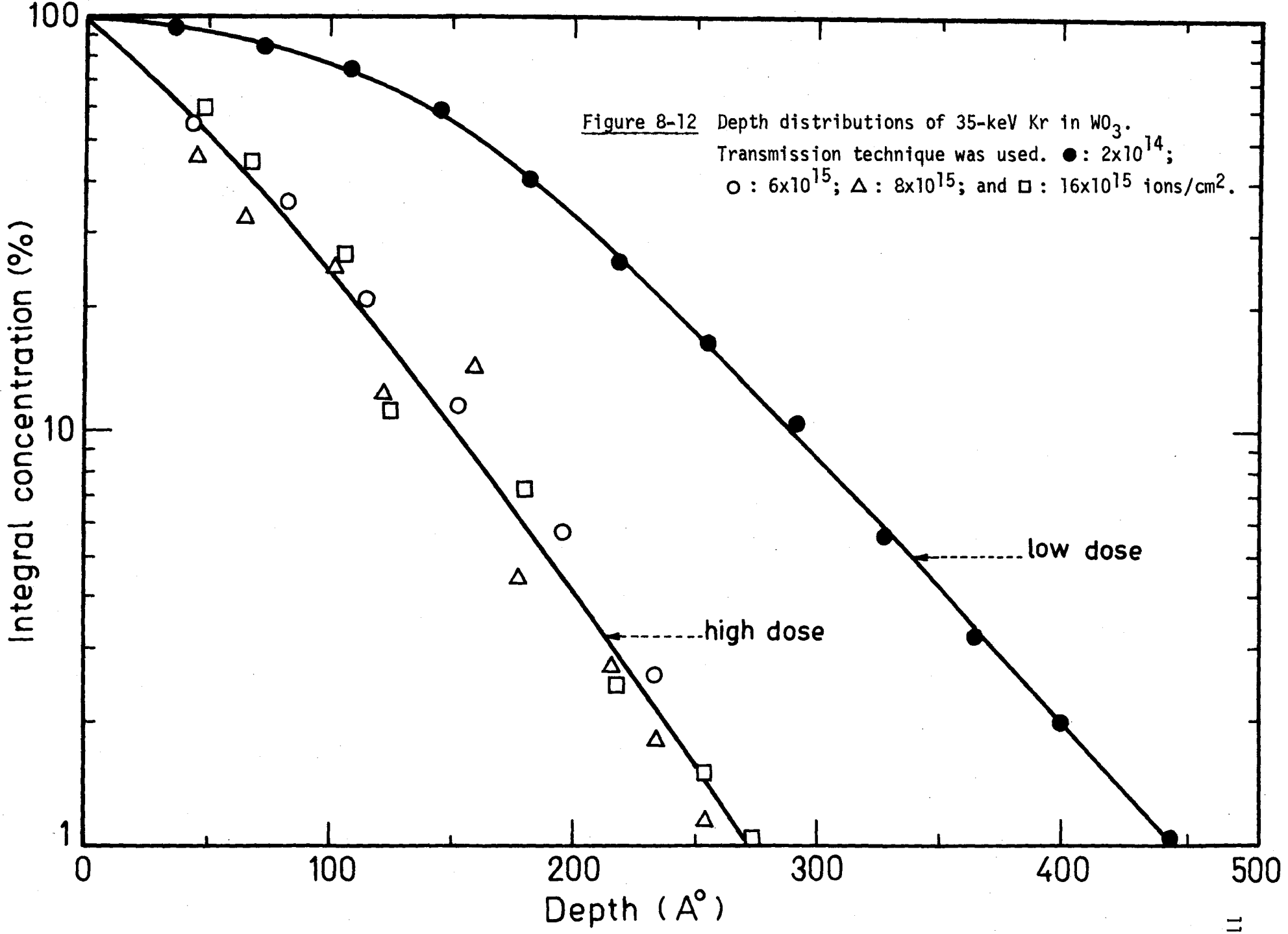

Figure 8-12 Depth distributions of 35-keV Kr in WO_3. Transmission technique was used. ●: 2×10^{14}; ○: 6×10^{15}; △: 8×10^{15}; and □: 16×10^{15} ions/cm^2.

agreement between the two techniques used in the case of WO_3 is excellent. High dose effects will be seen to be evident in all three oxides under study, in all cases being such that penetration depths are shortened.

Effects of pre-bombardment (implantation of non-radioactive Kr prior to bombardment with active Kr) and post-bombardment (bombardment with either non-radioactive Kr or O_2 after implantation of active Kr) are shown in Figures 8-13 to 8-16 for WO_3 and Al_2O_3. The main, though not unique, effect is again that penetration depths are shortened.

8.2.2 Low-Temperature Bombardment

Figure 8-17 presents the target arrangement which was used for low-temperature bombardment. The specimen holder has been connected to a liquid-nitrogen container, so that specimens to be bombarded could easily be cooled to -75°C.

Depth distributions of 10-keV Kr implanted in Nb_2O_5 and WO_3 at -30°C and -75°C are reported in Figures 8-18 to 8-21.

8.2.3 High-Temperature Bombardment

The target arrangement for high-temperature experiments is shown in Figure 8-22. Specimens to be bombarded were heated by a 6-ohm Kanthal filament which was connected to a 25-volt power supply. The power supply itself was powered via a 1:1 insulating transformer and could therefore be floated at the target potential.

Figures 8-23 to 8-26 show the distribution profiles of 10-keV Kr implanted in Al_2O_3 at 200, 400, and 500°C and in Nb_2O_5 and WO_3 at 200 and 300°C. Depth distributions in Nb_2O_5 and WO_3 could not be obtained at higher temperatures because of the reduced solubility of the oxides which

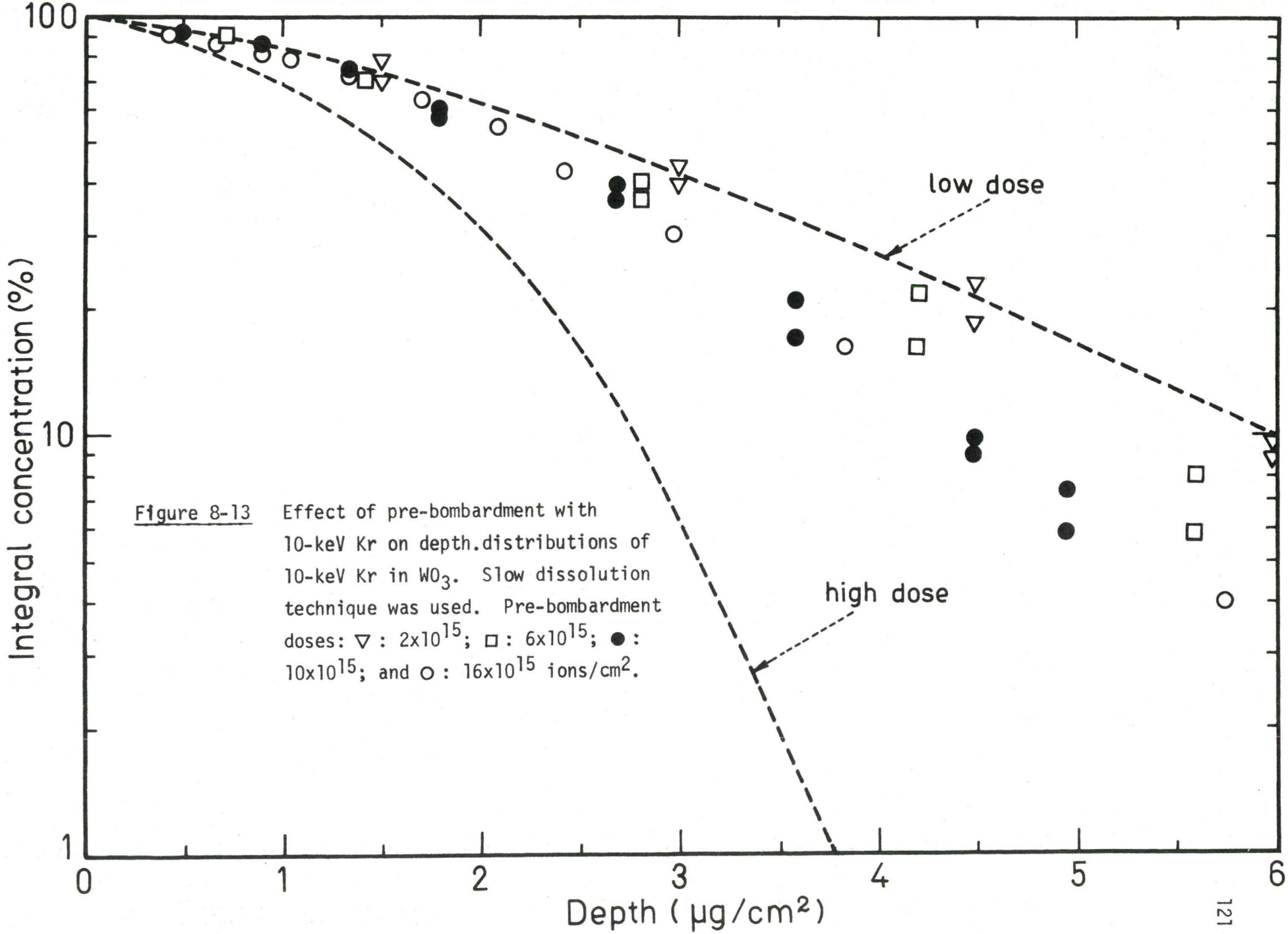

Figure 8-13 Effect of pre-bombardment with 10-keV Kr on depth.distributions of 10-keV Kr in WO_3. Slow dissolution technique was used. Pre-bombardment doses: ▽ : 2×10^{15}; □ : 6×10^{15}; ● : 10×10^{15}; and ○ : 16×10^{15} ions/cm^2.

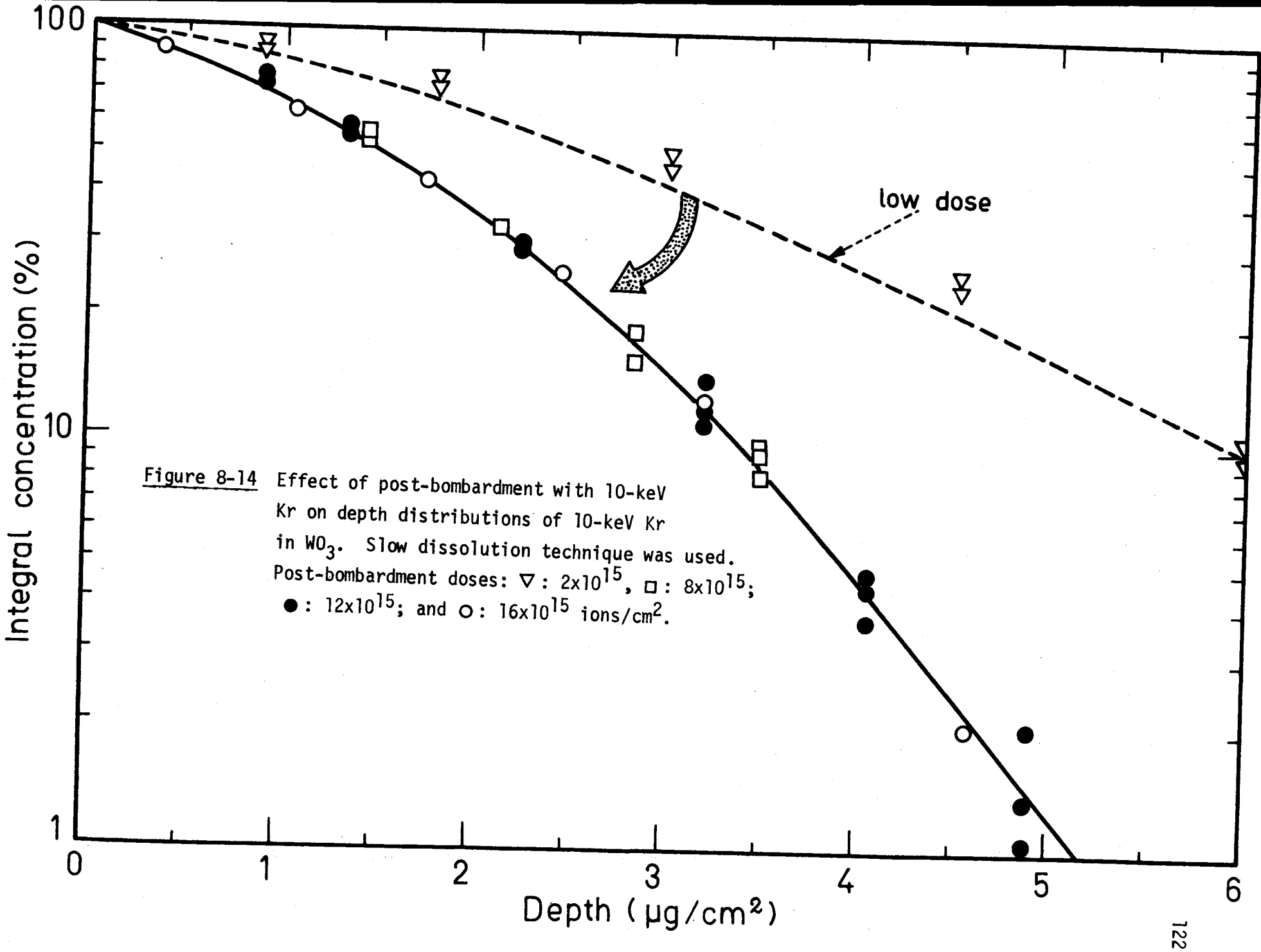

Figure 8-14 Effect of post-bombardment with 10-keV Kr on depth distributions of 10-keV Kr in WO_3. Slow dissolution technique was used. Post-bombardment doses: ▽ : 2×10^{15}, □ : 8×10^{15}; ● : 12×10^{15}; and ○ : 16×10^{15} ions/cm^2.

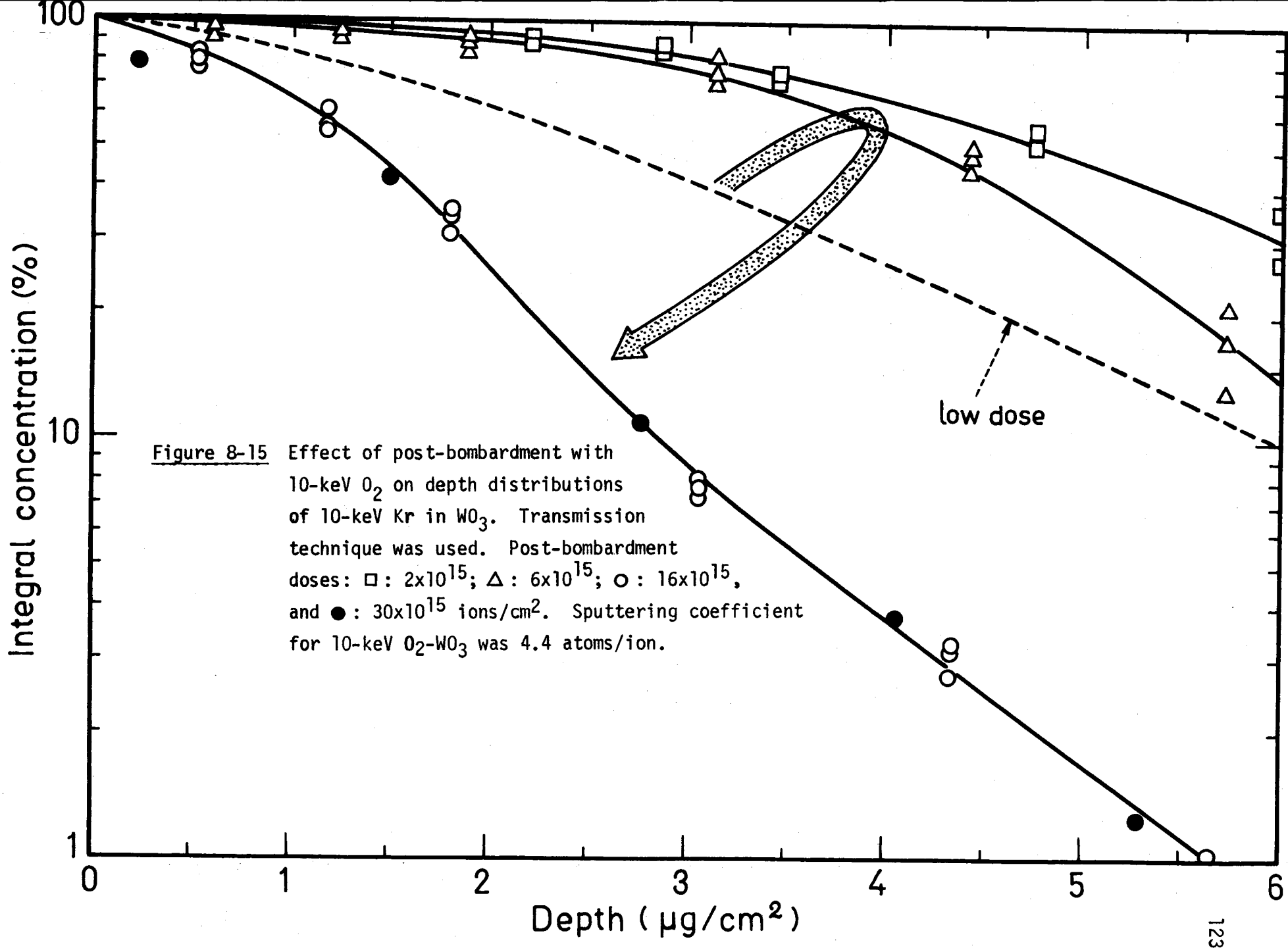

Figure 8-15 Effect of post-bombardment with 10-keV O_2 on depth distributions of 10-keV Kr in WO_3. Transmission technique was used. Post-bombardment doses: □ : 2×10^{15}; △ : 6×10^{15}; ○ : 16×10^{15}, and ● : 30×10^{15} ions/cm^2. Sputtering coefficient for 10-keV O_2-WO_3 was 4.4 atoms/ion.

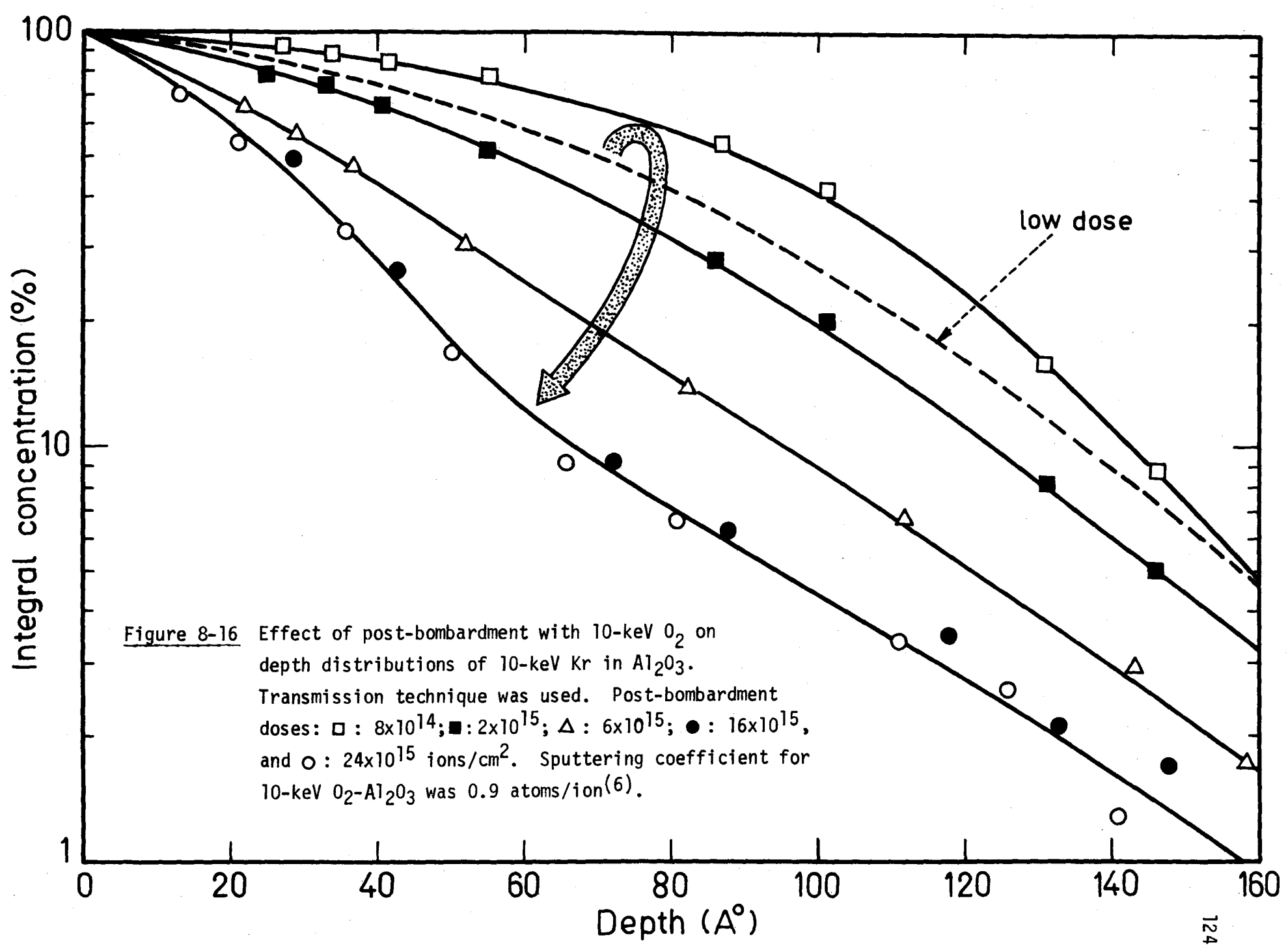

Figure 8-16 Effect of post-bombardment with 10-keV O_2 on depth distributions of 10-keV Kr in Al_2O_3. Transmission technique was used. Post-bombardment doses: □ : 8×10^{14}; ■ : 2×10^{15}; △ : 6×10^{15}; ● : 16×10^{15}, and ○ : 24×10^{15} ions/cm^2. Sputtering coefficient for 10-keV O_2-Al_2O_3 was 0.9 atoms/ion[6].

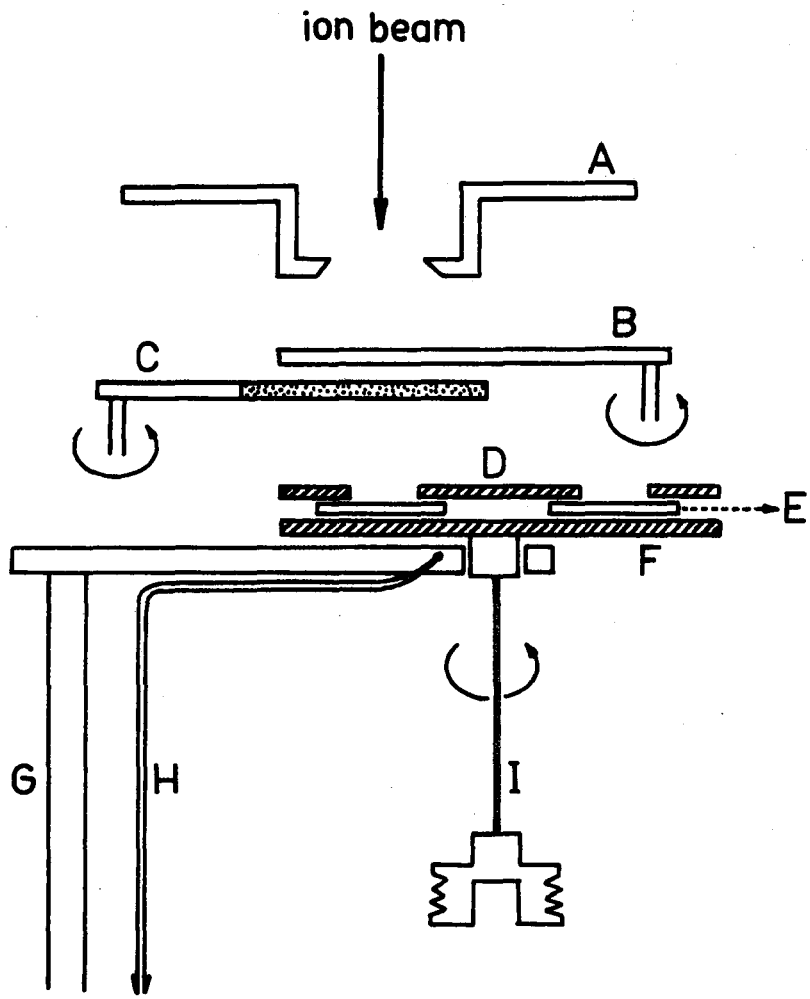

Figure 8-17 Target Arrangement for Low-temperature Bombardment. A: defining iris; B: shutter; C: fluorescent screen; D: mask; E: specimen; G: cooler connected to a liquid nitrogen container; H: thermocouple connected to a potentiometer; and I: metallic wire connecting the target to a high-tension power supply.

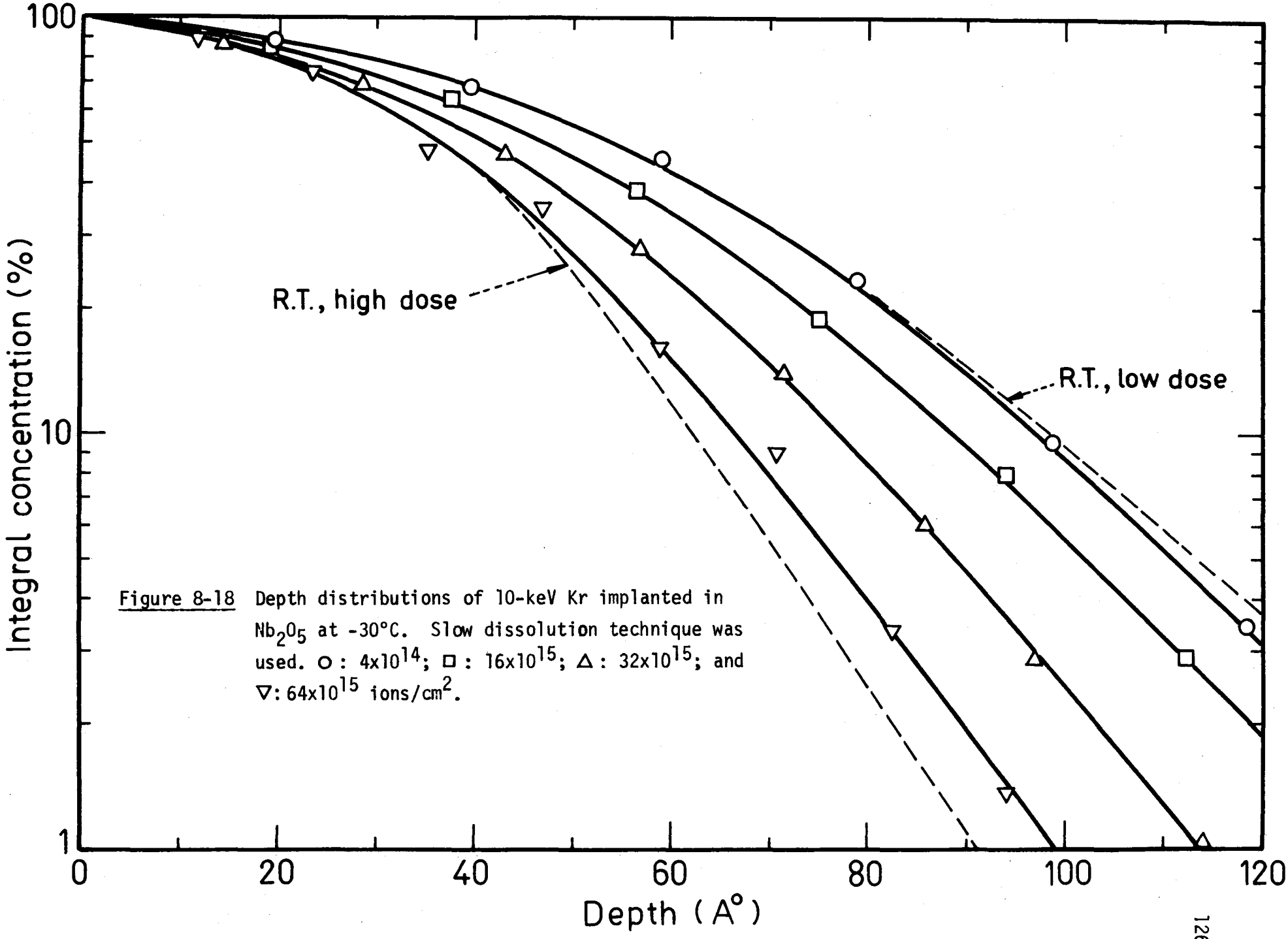

Figure 8-18 Depth distributions of 10-keV Kr implanted in Nb_2O_5 at -30°C. Slow dissolution technique was used. ○ : 4×10^{14}; □ : 16×10^{15}; △ : 32×10^{15}; and ▽: 64×10^{15} ions/cm^2.

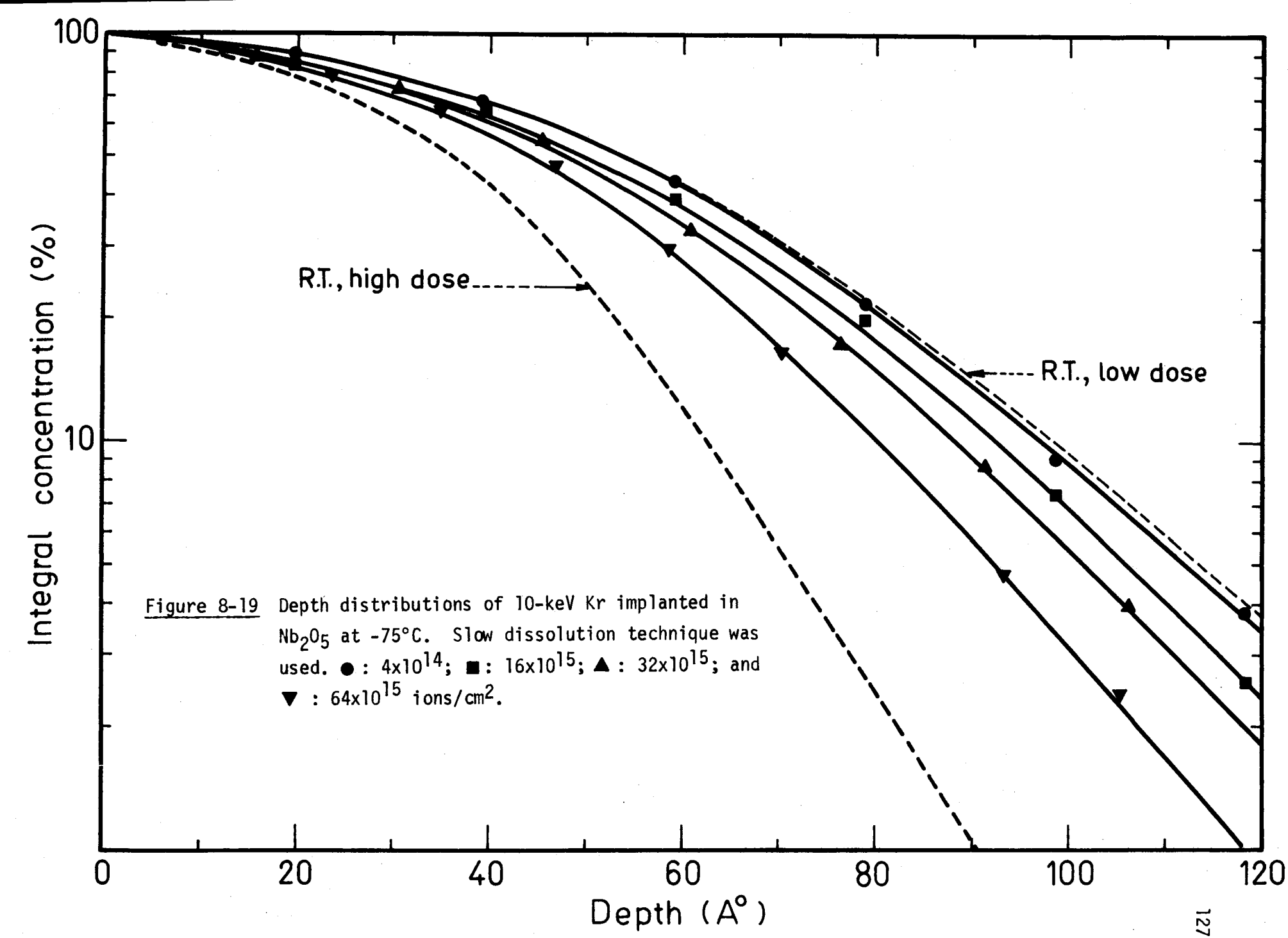

Figure 8-19 Depth distributions of 10-keV Kr implanted in Nb_2O_5 at -75°C. Slow dissolution technique was used. ● : 4×10^{14}; ■ : 16×10^{15}; ▲ : 32×10^{15}; and ▼ : 64×10^{15} ions/cm^2.

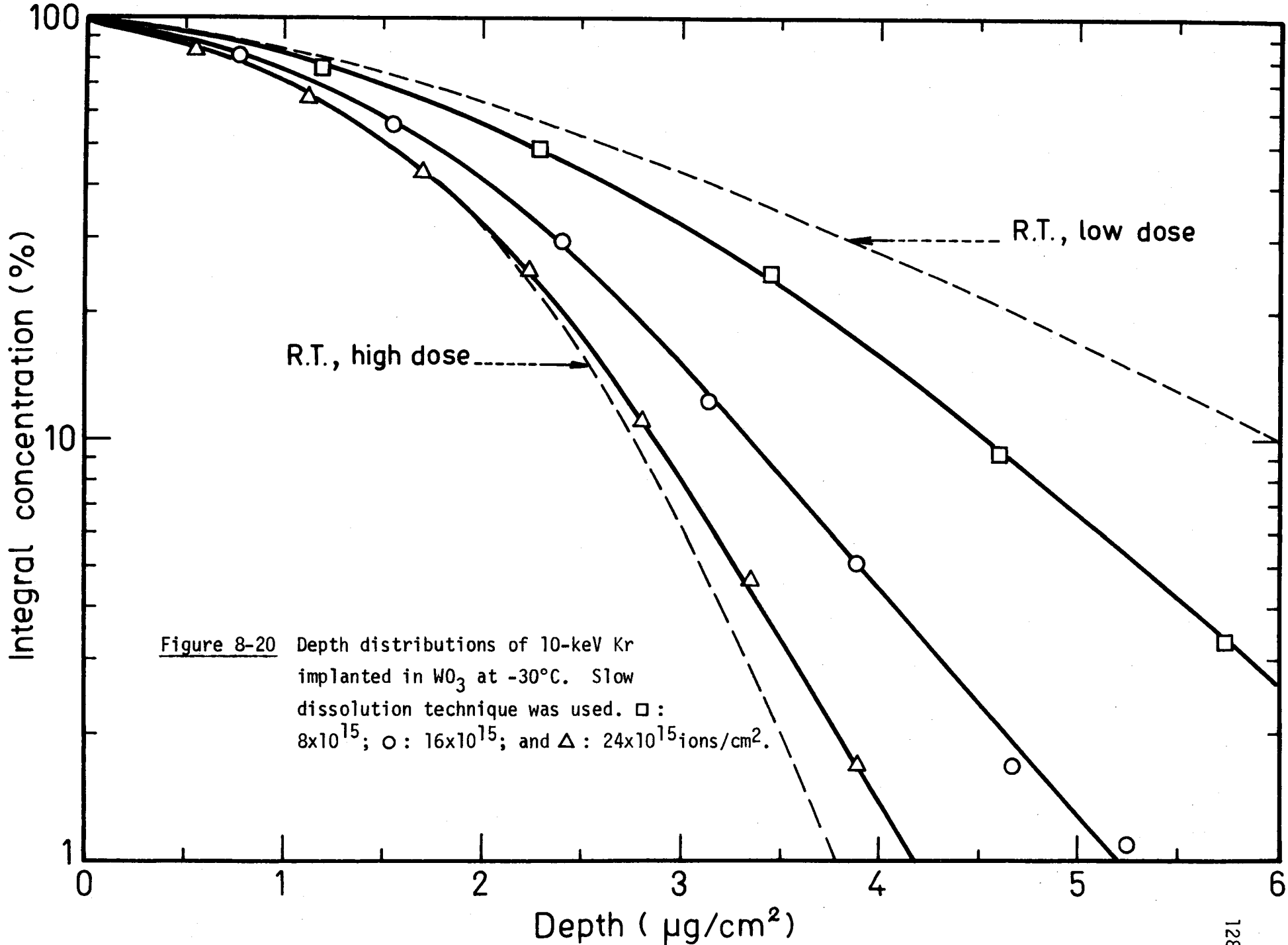

Figure 8-20 Depth distributions of 10-keV Kr implanted in WO_3 at -30°C. Slow dissolution technique was used. □ : 8×10^{15}; ○ : 16×10^{15}; and △ : 24×10^{15} ions/cm^2.

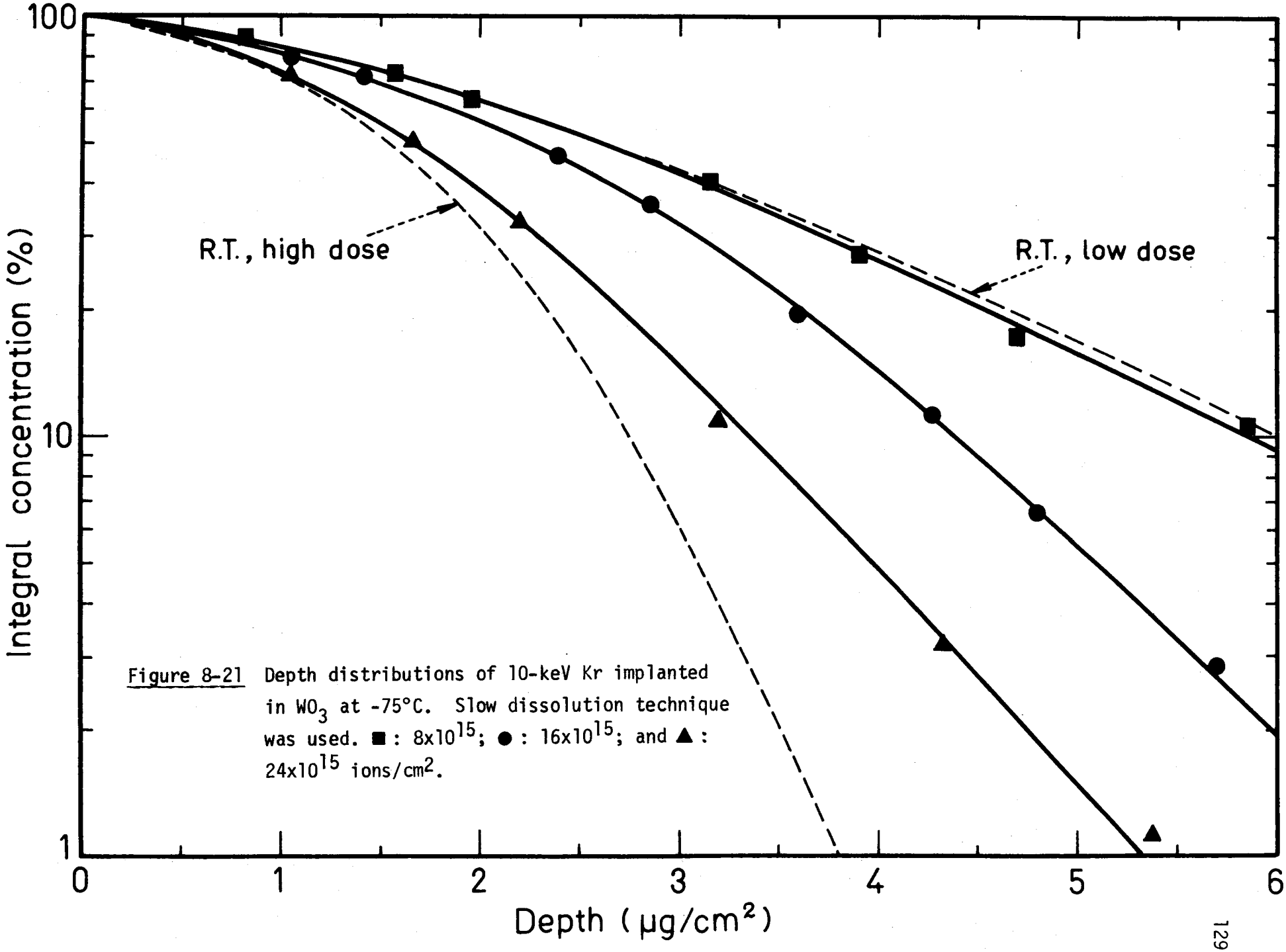

Figure 8-21 Depth distributions of 10-keV Kr implanted in WO_3 at -75°C. Slow dissolution technique was used. ■ : 8×10^{15}; ● : 16×10^{15}; and ▲ : 24×10^{15} ions/cm^2.

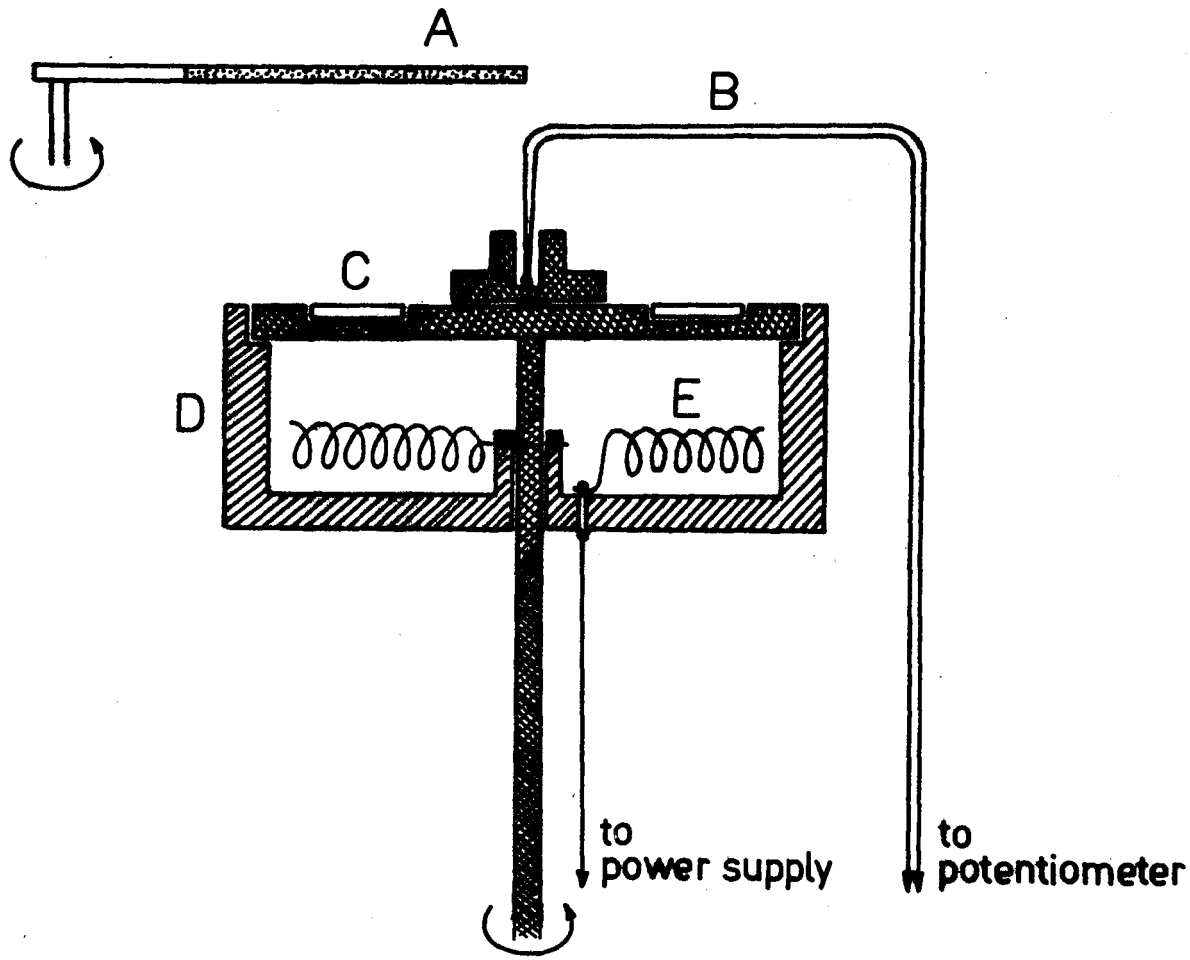

Figure 8-22 Target arrangement for hot implantation. A: fluorescent screen; B: thermocouple; C: specimen; D: pyrophillite furnace body; and E: kanthal filament, connected to a power supply.

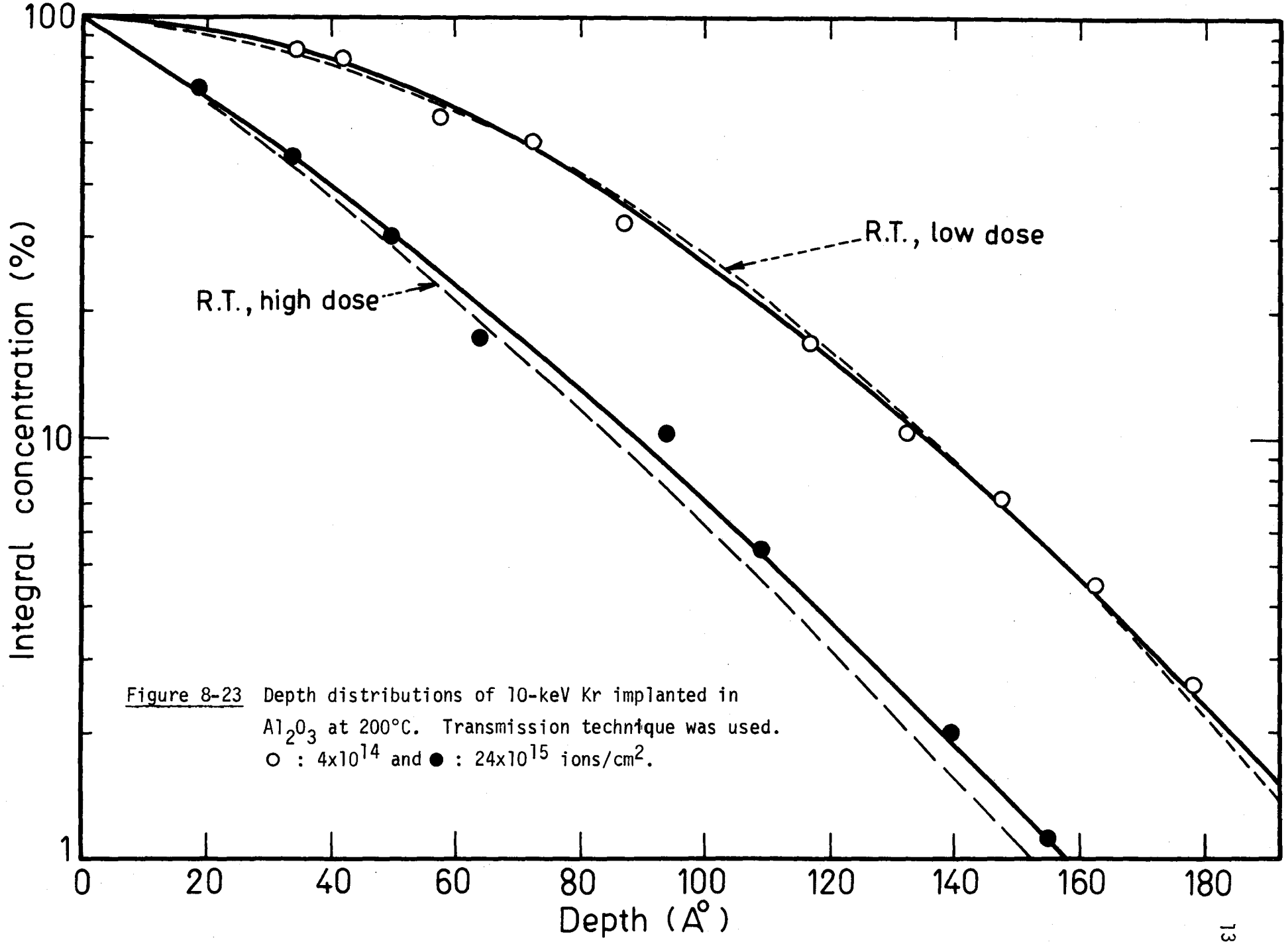

Figure 8-23 Depth distributions of 10-keV Kr implanted in Al_2O_3 at 200°C. Transmission technique was used. ○ : 4×10^{14} and ● : 24×10^{15} ions/cm^2.

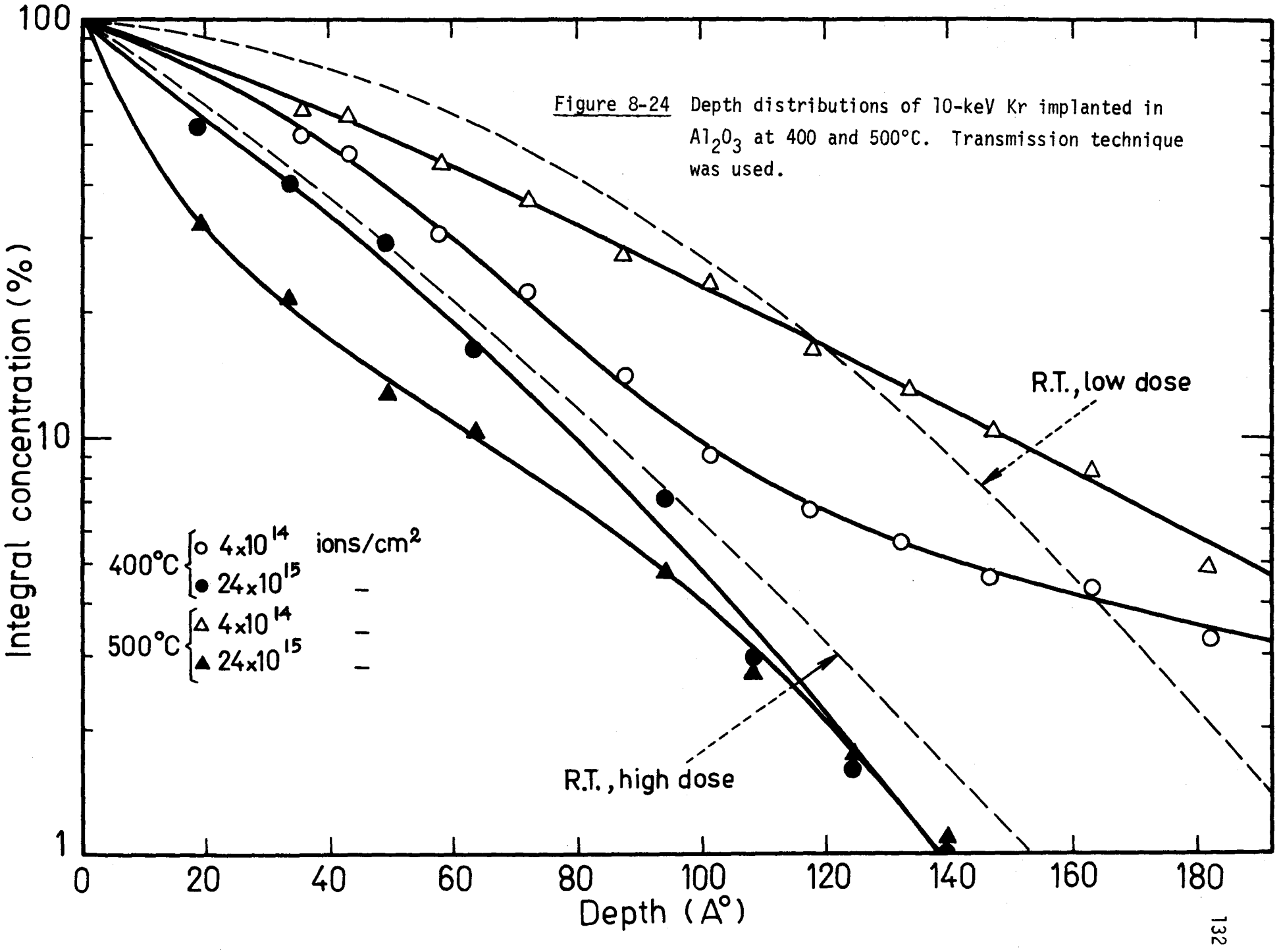

Figure 8-24 Depth distributions of 10-keV Kr implanted in Al_2O_3 at 400 and 500°C. Transmission technique was used.

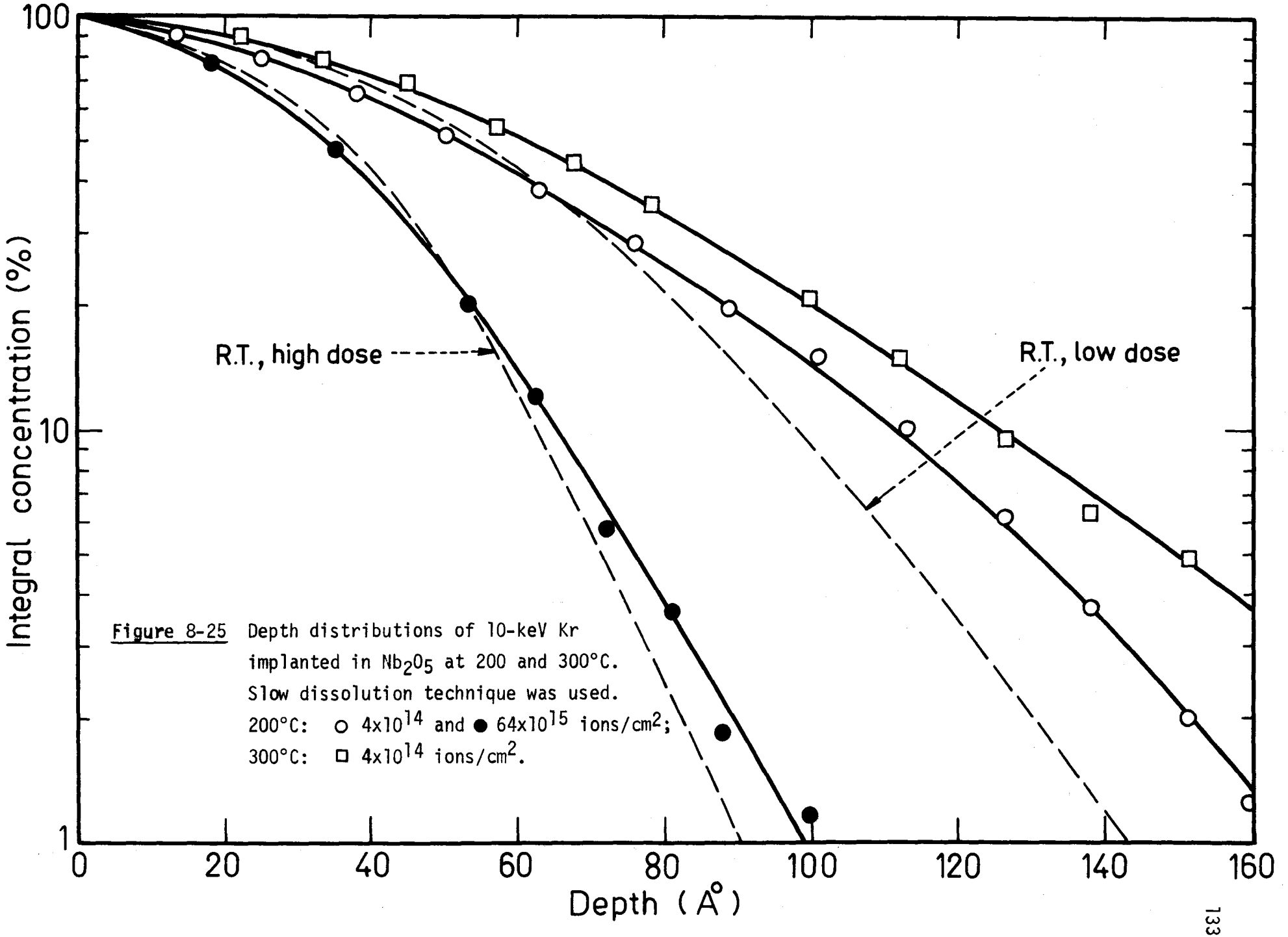

Figure 8-25 Depth distributions of 10-keV Kr implanted in Nb_2O_5 at 200 and 300°C. Slow dissolution technique was used.
200°C: ○ 4×10^{14} and ● 64×10^{15} ions/cm^2;
300°C: □ 4×10^{14} ions/cm^2.

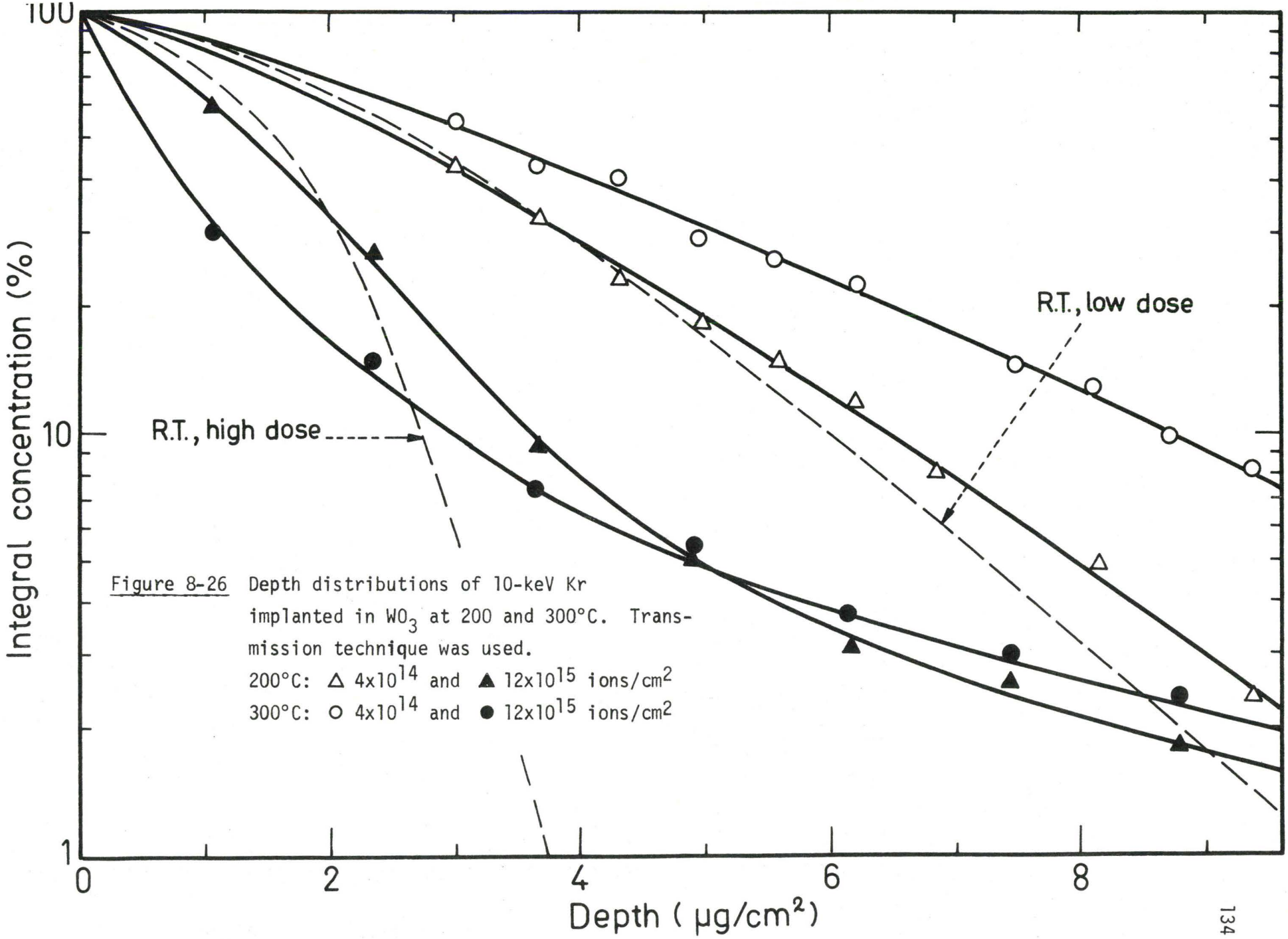

Figure 8-26 Depth distributions of 10-keV Kr implanted in WO_3 at 200 and 300°C. Transmission technique was used.
200°C: △ 4×10^{14} and ▲ 12×10^{15} ions/cm^2
300°C: ○ 4×10^{14} and ● 12×10^{15} ions/cm^2

was probably due to the onset of crystallization .

8.2.4 Gas-Release Spectra

The rate of Kr release from a wide variety of materials (Al_2O_3, Au, KCl, Nb_2O_5, Pt, Si, Ta_2O_5, WO_3, and ZrO_2) is shown in Figures 8-27 to 8-29. Note that the decreased release rate near room temperature is mainly an artifact of the heating schedule.

8.3 DISCUSSION

8.3.1 Depth Distributions at High Doses (Room Temperature)

The work on radiation-enhanced diffusion in Si and Ge by Pfister[114] and Brelot[115] has revealed that post-bombardments with light particles (protons) cause the expected deep penetration of various dopants (B, Ga, P, Sb), this being formally equivalent to the rotation effect as described in Section 5-2. In the work of Kelly[6,116] and the present investigation (Figures 8-7, 8-8, 8-11, 8-12, and 8-14 to 8-16), which are essentially post-bombardments with heavy particles, the converse has been found: the ion depth distributions tended to approach the surface at high doses. This is brought out also by examining Table 8-2 where the theoretical and experimental values of median and mean ranges of Kr in Al_2O_3, Nb_2O_5, and WO_3 are summarized. The observed values of R_m for high doses of 10-keV Kr in these oxides are a factor of 2 to 3 lower than those obtained for low dose.

These systems are of special interest in that the oxides were initially amorphous and the change in distribution cannot therefore be attributed to amorphization as in the work of Whitton and Matzke[118]. In addition, it can be shown that the increase in target stopping power is unimportant.

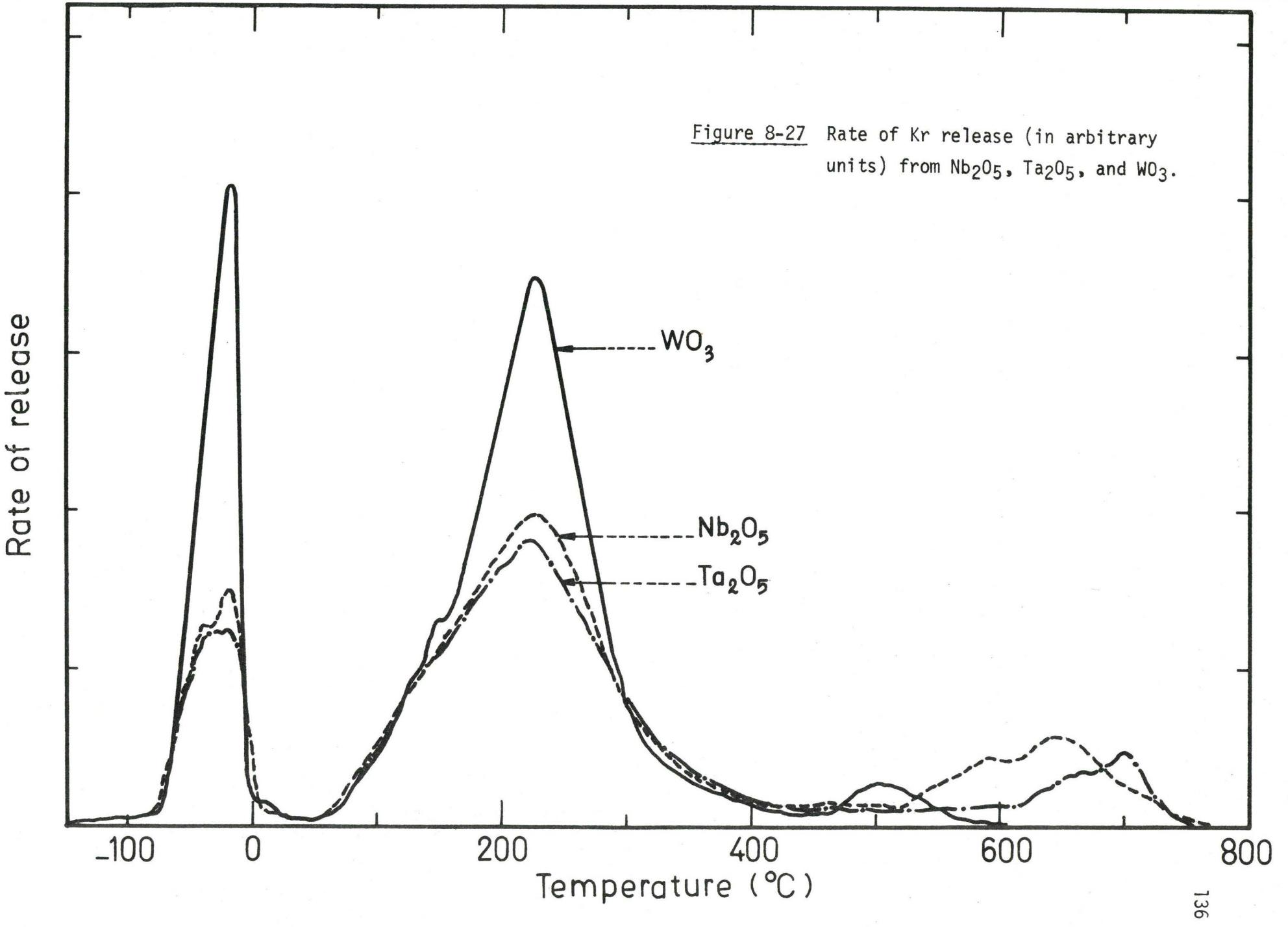

Figure 8-27 Rate of Kr release (in arbitrary units) from Nb_2O_5, Ta_2O_5, and WO_3.

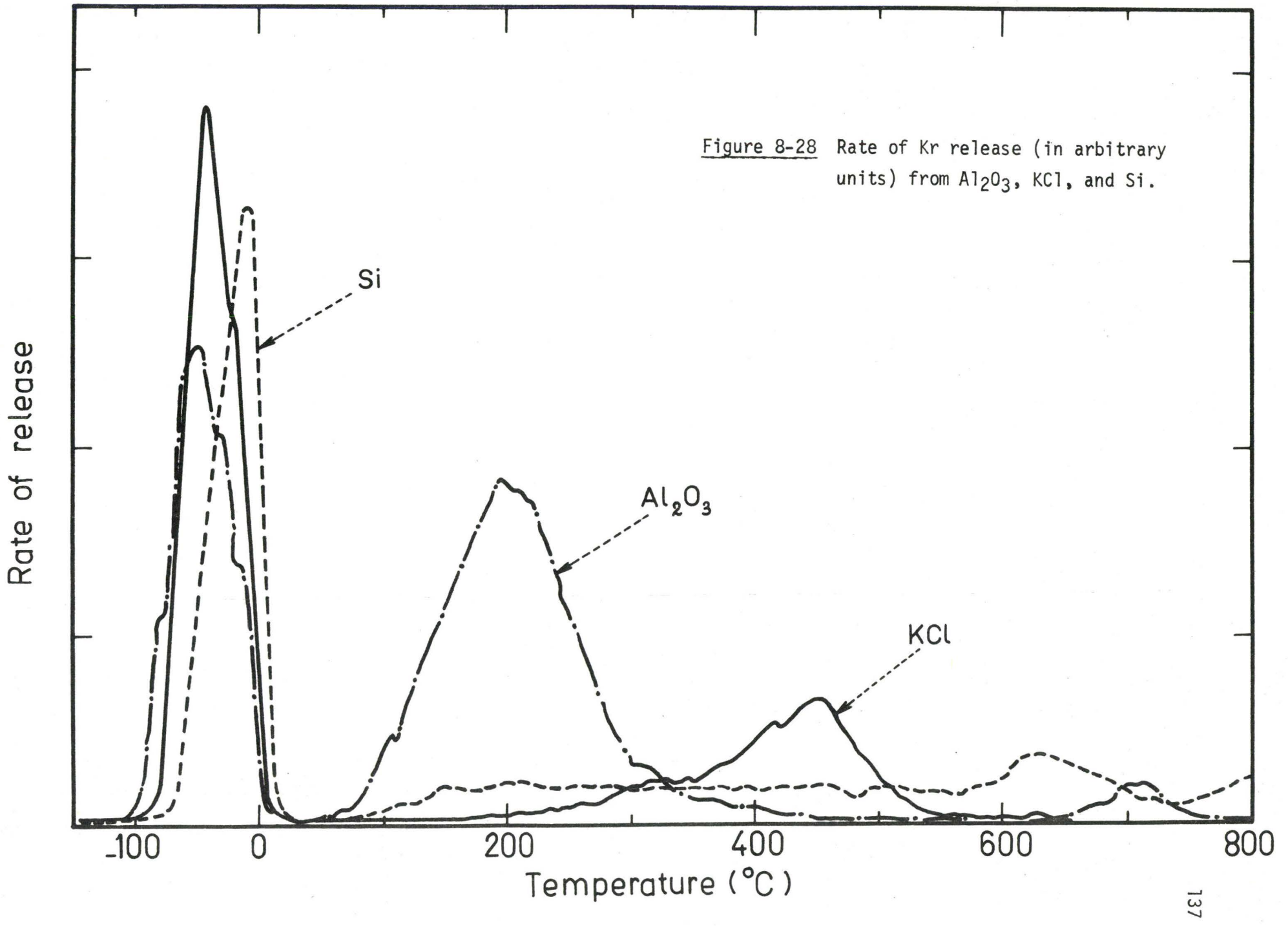

Figure 8-28 Rate of Kr release (in arbitrary units) from Al_2O_3, KCl, and Si.

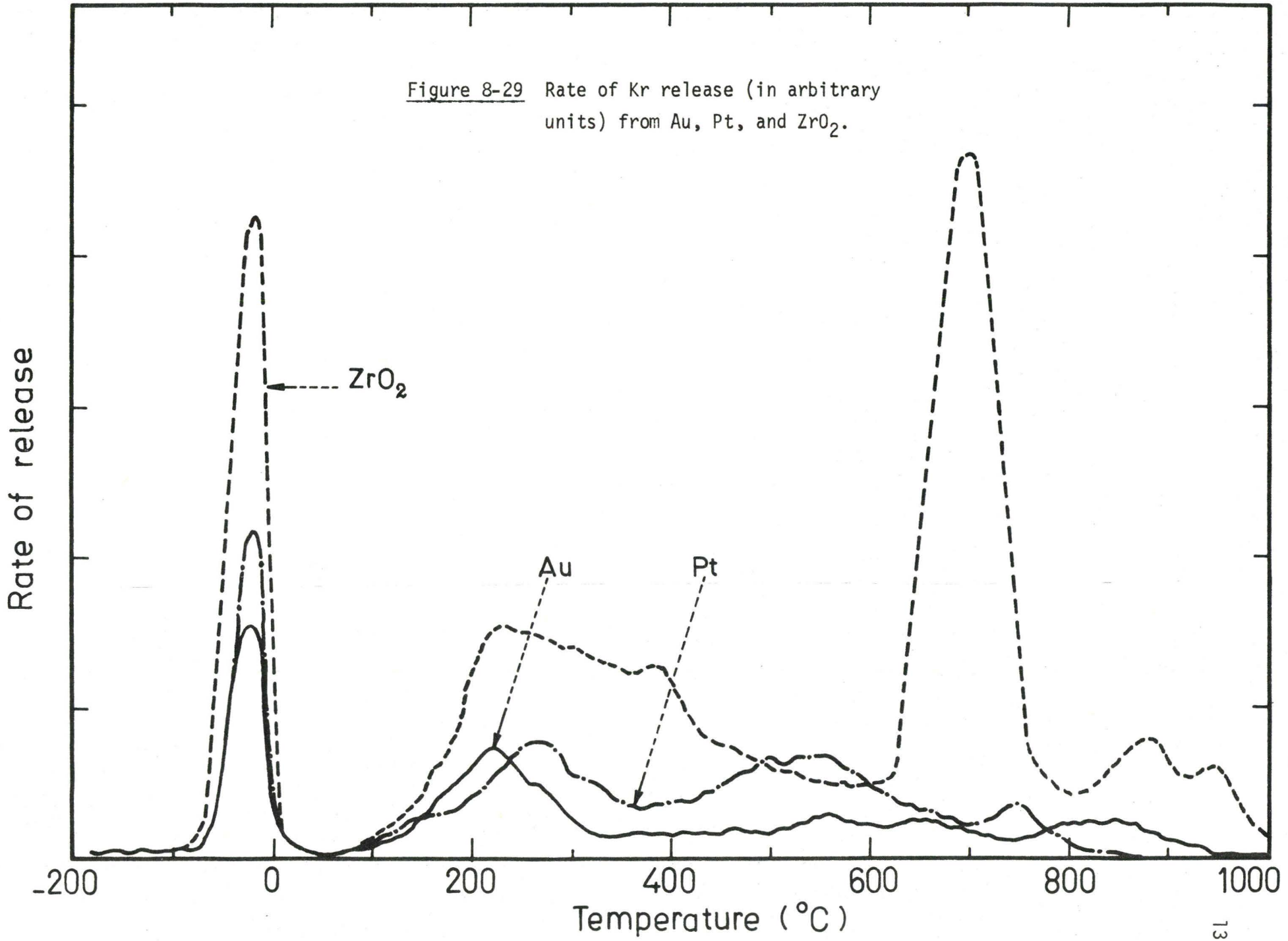

Figure 8-29 Rate of Kr release (in arbitrary units) from Au, Pt, and ZrO_2.

TABLE 8-2

Values of the Median Range, R_m, and the Mean Range, $\langle R_i \rangle$ for 10-keV Kr

Dose, ion-target	R_m(Å)	$\langle R_i \rangle$ (Å)	Reference
Low-dose Kr-Al_2O_3 (exper.)	72	86*	Fig. 8-7
	68	81*	(6)
	77	92*	(93)
Low-dose Kr-Al_2O_3 (theor.)		65	(53)
High-dose Kr-Al_2O_3	28		Fig. 8-7
	29		(6)
	11+		(6)
Low-dose Kr-Al_2O_3 + post-bombard. with O_2	26		Fig. 8-16
Low-dose Kr-Nb_2O_5 (exper.)	55	66*	Fig. 8-8
Low-dose Kr-Nb_2O_5 (theor.)		61	(53)
High-dose Kr-Nb_2O_5 (exper.)	37		Fig. 8-8
Low-dose Kr-WO_3 (exper.)	38	45*	Fig. 8-10
	37	44*	(93)
Low-dose Kr-WO_3 (theor.)		59	(53)
		58✓	(117)
High-dose Kr-WO_3 (exper.)	23		Fig. 8-11
High-dose Kr-WO_3 (prebombard)	34		Fig. 8-13
High-dose Kr-WO_3 (post-bomb. with Kr)	22		Fig. 8-14
Low-dose Kr-WO_3 + post-bomb. with O_2	21		Fig. 8-15

* Deduced from R_m by multiplying by 1.19 as would be true for a distribution which can be described analytically by $x dx / R^2_{mp} \exp(-x/R_{mp})$.

\+ Obtained by sputtering technique.

✓ Calculated using the formula $\langle R_i \rangle = 0.85576\ E^{2/3}$ with m = 1/3.

An attractive explanation for data as discussed above is that one is in all cases dealing with radiation-enhanced diffusion, whether due to excess vacancies[114-115], due to thermal spikes[119], or due to the implanted atoms being promoted into high mobility sites[6,120-122].

For light-particle post-bombardments, the implanted atoms would diffuse according to normal diffusion solutions such as equation 5-2. For high-dose bombardments with heavy particles, however, the damage which is created is very intense, and the ions would diffuse according to the models described in Sections 5.3.2 or 5.3.4. These models also predict that there would be a limiting diffusion profile for high enough doses with C^{int} proportional to either cos(ax) or $\exp(-\Delta H_o gx/RT)$. Though neither of these functions really fits the data exactly, the existance of a limiting profile is in good agreement with the experimental findings (Figures 8-7 to 8-9, 8-11, 8-12, and 8-14 to 8-16).

Erents and Carter[123] have had evidence that post-bombardment of W with Xe ions brought initially implanted Ne atoms closer to the target surface and caused the Ne release to occur at lower temperatures. This phenomenon has been considered as involving enhanced diffusion of the gas atoms in the thermally disturbed region near the point of ion impact. A slightly different mechanism has also been envisaged by Kelly[6], Nelson[120], Kelly and Jech[121], and Matzke and Jech[122], in which enhanced diffusion in other systems is again proposed but is assumed to arise owing to the knocking of the gas atoms into positions of high diffusivity, for example, interstitial sites. In addition, various authors have noted that the apparent sputtering yield of an inert gas in a metal, as caused by

impact of a different inert gas, is much too high[124-125]. We would regard this as still a further example of surface-directed motion.

One crucial experiment in helping to elucidate the problem of "range shortening" concerns the effect of post-bombardment with heavy ions on the distribution of Kr^{85} in WO_3 and Al_2O_3 (Figures 8-14 to 8-16). Post-bombardment with Kr of the same energy caused a "range shortening" similar to that found for high-dose bombardment (Figure 8-11). However, post-bombardment with O_2, which has a 4-fold longer range than Kr at the same energy, first, at low doses, lengthened the range of Kr^{85}, and then, at high enough doses, the "range shortening" set in. This would therefore be an expected result, for according to our model for describing the out-diffusion of implanted ions one is in all cases dealing with radiation-enhanced diffusion, though with details which differ completely depending on the dose.

Another crucial experiment is that shown in Figure 8-13, which concerns the effect of pre-bombardment with inactive Kr on the range of subsequently implanted Kr^{85}. The variation in the median range is seen to be very small, the reason for this presumably being as follows. The secondary Kr^{85} ions came to rest either in normal target material or in damage sites created by the primary Kr; they are subsequently immobile instead of being "stirred up" many times into high-diffusivity positions. Their depth distribution, therefore, does not show their surface-directed motion, though there was probably an out-diffusion of <u>inactive</u> gas during the pre-bombardment stage. A related effect of pre-bombardment has been observed by Erents and Carter[123] who found that the trapping of low energy He in W was greatly enhanced by the prior bombardment of the surface

with a more massive ion. We note, however, that with the heavy inert gases, the mobility is normally sufficiently low that it is not necessary to presuppose trapping effects for the gas to remain stationary.

A third crucial experiment for giving evidence of the "range shortening" due to out-diffusion concerns the rate of Kr release from various materials, as shown in Figures 8-27 to 8-29. The argument is essentially the following: whenever radiation-enhanced diffusion seems to occur, then it should be possible to confirm in conventional gas-release (or similar) experiments a diffusion component which is rate controlling at the bombardment temperature. The evidence to date suggests that surprisingly large amounts of diffusion occur near room temperature with a wide variety of materials, including Al_2O_3, Nb_2O_5, Ta_2O_5, WO_3, and ZrO_2. Such diffusion is apparently a low-temperature extension of the already well-documented stage-IA-type behaviour[121-122]. Stage IA is most simply described as any gas-release process which occurs well below the temperatures of volume self-diffusion and, at the same time, cannot be attributed to the annealing of bombardment-induced disorder. It has been explained in terms of gas which is fortuitously located in high mobility sites, for example, interstitial sites, though the exact explanation is unimportant in the present context.

In summary, the point being made here is that whenever a primary implanted atom, which came to rest in a heavily damaged medium, is promoted, by secondary incoming ions, to a high-mobility site, then it should start to diffuse toward the surface. But the same type of promotion in a less-damaged medium causes diffusion to greater depths.

The ideas of this section should apply equally to the case where a depth distribution is obtained by alternately counting and sputtering a target under conditions when the sputtering energy is comparable to the labeling energy[6,116]. In effect, these experiments do not give true range parameters.

8.3.2 Depth Distributions at High Doses (Low Temperatures)

Figures 8-18 to 8-21 show the Kr depth distributions in Nb_2O_5 and WO_3 for implantations at -30 and -75°C. The main result is that the low-dose limit persists to significantly higher doses than in room temperature implants. This would again be a natural result, however, if the range shortening were due to radiation-enhanced diffusion.

A major difficulty might seem to arise at first sight with this explanation: why does the usual motion towards the surface not occur following implantation when the specimen is brought up to room temperature? The reason is probably as follows. A 10-keV Kr bombardment of WO_3, for which $\langle R_i \rangle$ is 45 Å (Table 8-2), is characterized by a non-correlated transverse damage straggling, i.e. $(\langle y^2_D \rangle)^{1/2}$, of 15 Å[28] thence by an impact area of about 700 $Å^2$/ion. This means that for a dose of 8×10^{15} ions/cm^2, 90 per cent of the ions are "stirred up" about 500 times. In room-temperature or high temperature implants the ions will therefore have repeated opportunity to diffuse the trapping length L towards the surface.

In a low temperature implantation followed by heating to room temperature, on the other hand, a given ion has only one chance to diffuse the distance L.

A high-dose effect leading to "range shortening" in low-tempera-

ture bombardment was also observed by Davies[126] for 1-MeV B implanted in Si at 78°K.

8.3.3 Depth-Distributions at High Doses (High Temperatures)

Depth distributions of 10-keV Kr implanted in Al_2O_3 at 200,400, and 500°C have been plotted in Figures 8-23 and 8-24. Distribution profiles of Kr in Al_2O_3 held at 200°C are not different from those obtained for room-temperature implantation; only in bombardments at 400 and 500°C is there a significant change. The tails of the low-dose curves show a rotation effect corresponding to normal diffusion solutions, as discussed in Section 5.2, whereas the high-dose profiles consistently approach the surface. We recall at this point that bombardments at room temperature revealed only surface-directed motion. These results would suggest that the bombardment-induced traps (e.g. vacancy clusters) created in an Al_2O_3 substrate by low-dose bombardment at 400 and 500°C in part annealed out, whereas those created by any dose at room temperature as well as by high doses at 400 and 500°C still remained at these temperatures. As a result the implanted atoms could diffuse according to the mechanisms described in Sections 5.3.2 or 5.3.4. An electron-microscopy study, which we will not take the space to discuss, revealed that Al_2O_3 was still amorphous after 500°C implantation with high doses of Kr[127]. Note that the crystallization temperature of amorphous Al_2O_3 is quite high, 730°C[113].

We have no explanation for the slight differences between the 400 and 500°C curves.

Figures 8-25 and 8-26 show the concentration profiles of 10-keV Kr implanted in Nb_2O_5 and WO_3 at 200 and 300°C. The appearance of the

rotation effect can be seen on the low-dose curves of both cases. The high-dose depth distribution of Kr in Nb_2O_5 does not show any remarkable change at 200°C, from which we conclude (as with Al_2O_3 at 400 and 500°C) that 200°C is still too low a temperature for annealing the large trapping centers produced by bombardment with high doses. We would therefore confirm still again that whenever there exists a spatial variation in the diffusion activation enthalpy, the migration of implanted Kr becomes surface-directed. In fact, as an evidence, reflection-electron-diffraction (Figure 8-30a) showed that anodic Nb_2O_5 still retained its amorphousness after bombardment at 200°C with 64×10^{15} ions/cm^2. Depth distribution of Kr implanted in Nb_2O_5 at 300°C and high dose could not be obtained due to the reduced solubility, which in turn makes the dissolution end-point unclear.

The high-dose profiles of Kr in WO_3 (Figure 8-26) are of special interest in that, in distinction to Al_2O_3 and Nb_2O_5, long diffusion tails can be observed even at high doses. In addition, as shown in Figures 8-30b and c, reflection-electron-diffraction revealed an amorphous-crystalline conversion of anodic WO_3 bombarded at 200°C with 12×10^{15} and 24×10^{15} ions/cm^2. A new phenomenon is therefore observed here, involving the occurrence of inward diffusion <u>in spite of</u> the high bombardment dose. Perhaps it is due to the ordering of the amorphous lattice, thence a removal of the traps which would ordinarily form; however, other explanations are also possible so it is unwise to insist on any particular one. Also, the subject of bombardment-induced crystallization is beyond the scope of this thesis*.

* The topic of bombardment-induced crystallization will be discussed in Naguib's thesis (McMaster University, 1971).

(a)

(b)

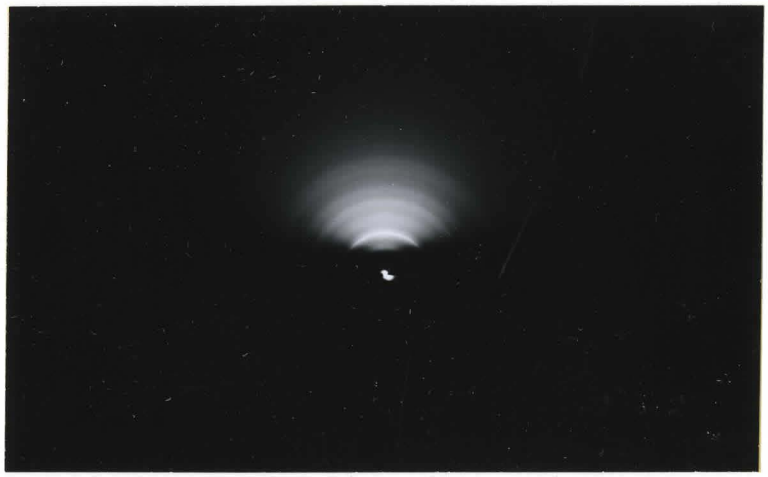

(c)

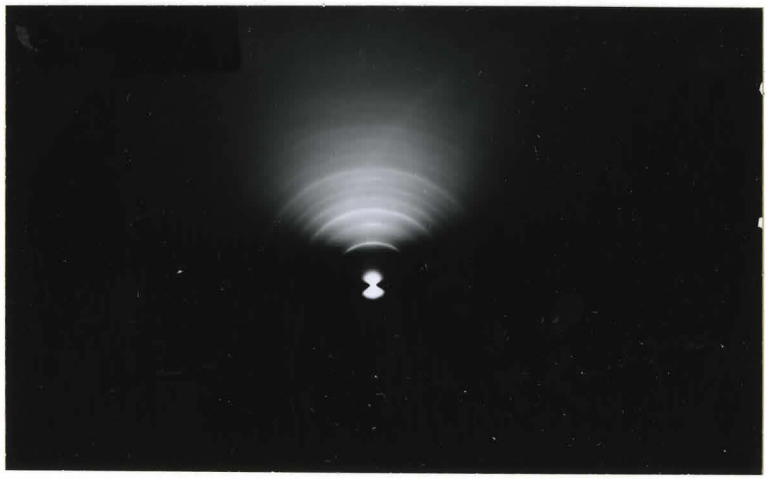

Figure 8-30 Reflection-electron-diffraction of (a) anodic Nb_2O_5 bombarded at 200°C with 64×10^{15} ions/cm^2, (b) anodic WO_3 bombarded at 200°C with 12×10^{15} ions/cm^2, and (c) anodic WO_3 bombarded at 200°C with 24×10^{15} ions/cm^2.

CHAPTER 9

BOMBARDMENT-INDUCED DISORDER IN WO_3*

9.1 TECHNIQUES

9.1.1 Preparation of Crystalline WO_3

Figure 9-1A shows a typical gas-release spectrum from a 65-volt anodic WO_3 film after labeling with 10-keV Kr, the peak at 475°C suggesting, by analogy with other amorphous materials[111, 130], that crystallization is complete at this temperature. To confirm this, a series of 65-volt specimens was heated to various temperatures for 15 min. in air. Reflection-electron-diffraction at 100 keV revealed that specimens heated to 200 and 350°C were only partially crystalline (Figures 9-2 a and b), whereas crystallization was virtually complete in specimens heated to 450 and 500°C (Figure 9-2c). The crystalline films were in a good physical state as demonstrated by scanning electron microscopy. As far as interference colors are concerned, specimens heated to 350°C showed no change, those heated to 450°C had colors implying increases in the anodization voltage of a factor of 1.15 ± 0.03, while those heated to 500°C had colors unrelated to the original thicknesses.

9.1.2 Amorphization of WO_3

It was established by both gas-release (Figures 9-1 B and C) and electron diffraction (Figure9-2d) that Kr bombardment of crystalline

---

* This Chapter is based on two papers by the author and R. Kelly[128-129]

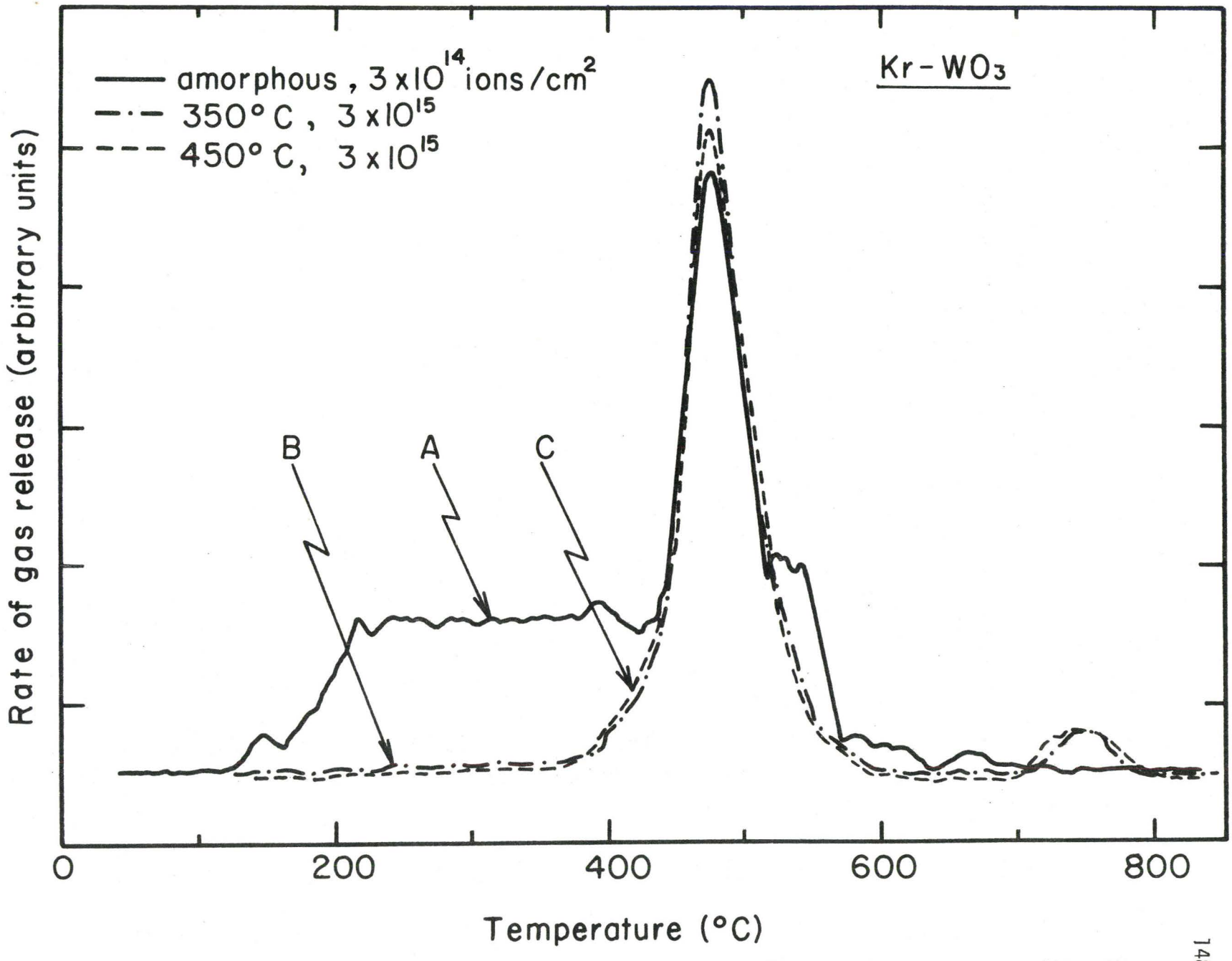

Figure 9-1 Rate of Kr release versus temperature for amorphous and crystalline WO_3.

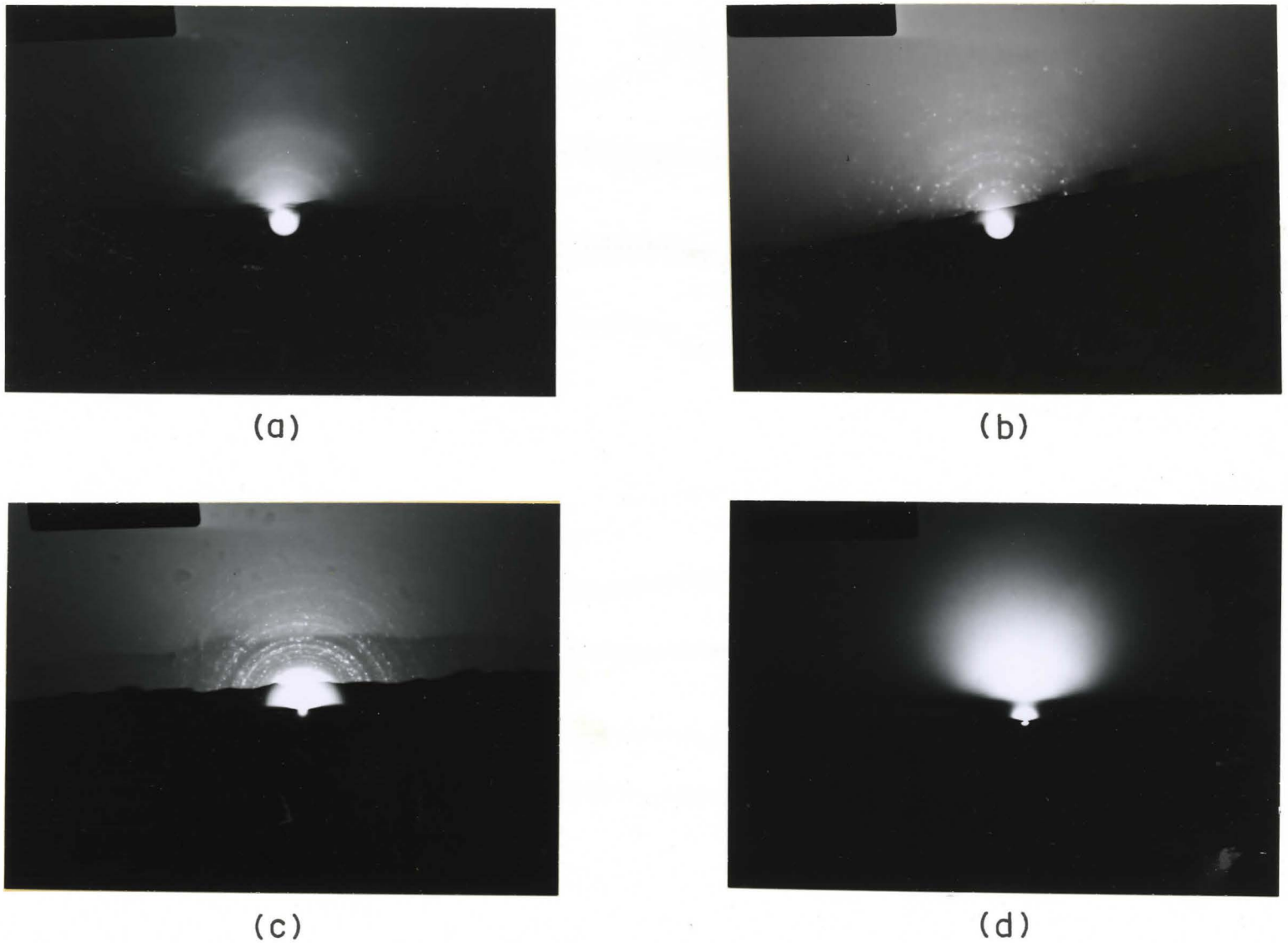

Figure 9-2 Reflection-electron-diffraction from WO_3: (a) heated to 200°C, (b) heated to 350°C, (c) heated to 450°C, and (d) heated to 450°C and then bombarded with 4×10^{14} ions/cm^2.

WO_3 restored an amorphous form. In general, amorphization was significant (corresponding to a fractional gas release greater than 0.1) for doses greater than 2×10^{13} ions/cm^2 (Figure 9-3); it tended to be lost, however, for doses greater than $\sim 1.5 \times 10^{16}$, probably due to preferential loss of oxygen. We recall that an analogous effect was found in Sections 8.1.1 and 8.3.3, in those cases as the tentative explanation for bombardment-induced solubility changes; the problem of oxygen loss, is however, beyond the scope of this thesis.

9.1.3 Methods of Measuring the Depth of Amorphization

Four different approaches were used to measure R_a, the depth of the amorphous-crystalline interface, for Kr-bombarded WO_3:

(a) Interference Colors: The most powerful approach was one which made direct use of the brilliant WO_3 interference colors. Unbombarded WO_3 which had been heated to 350 or 450°C was found to retain its original interference colors even after 5 hours exposure to 0.1 g/liter KOH, whereas the 10-keV Kr-bombarded regions took on colors characteristic of reduced thicknesses in less than 60 sec. R_a therefore follows as either:

$$R_a = (A-B) - C \quad \text{(films heated to 350°C)}$$

or

$$R_a = (A-B)/1.15 - C \quad \text{(films heated to 450°C)}$$

where A is the thickness inferred for the unbombarded region, B is the thickness inferred for the bombarded region after dissolution, 1.15 is the factor mentioned in Section 9.1.1, and C is the thickness of WO_3 removed by sputtering. C can be estimated for each ion dose with the sputtering parameters previously deduced (Chapter 7); see Table 8-1 for examples of C.

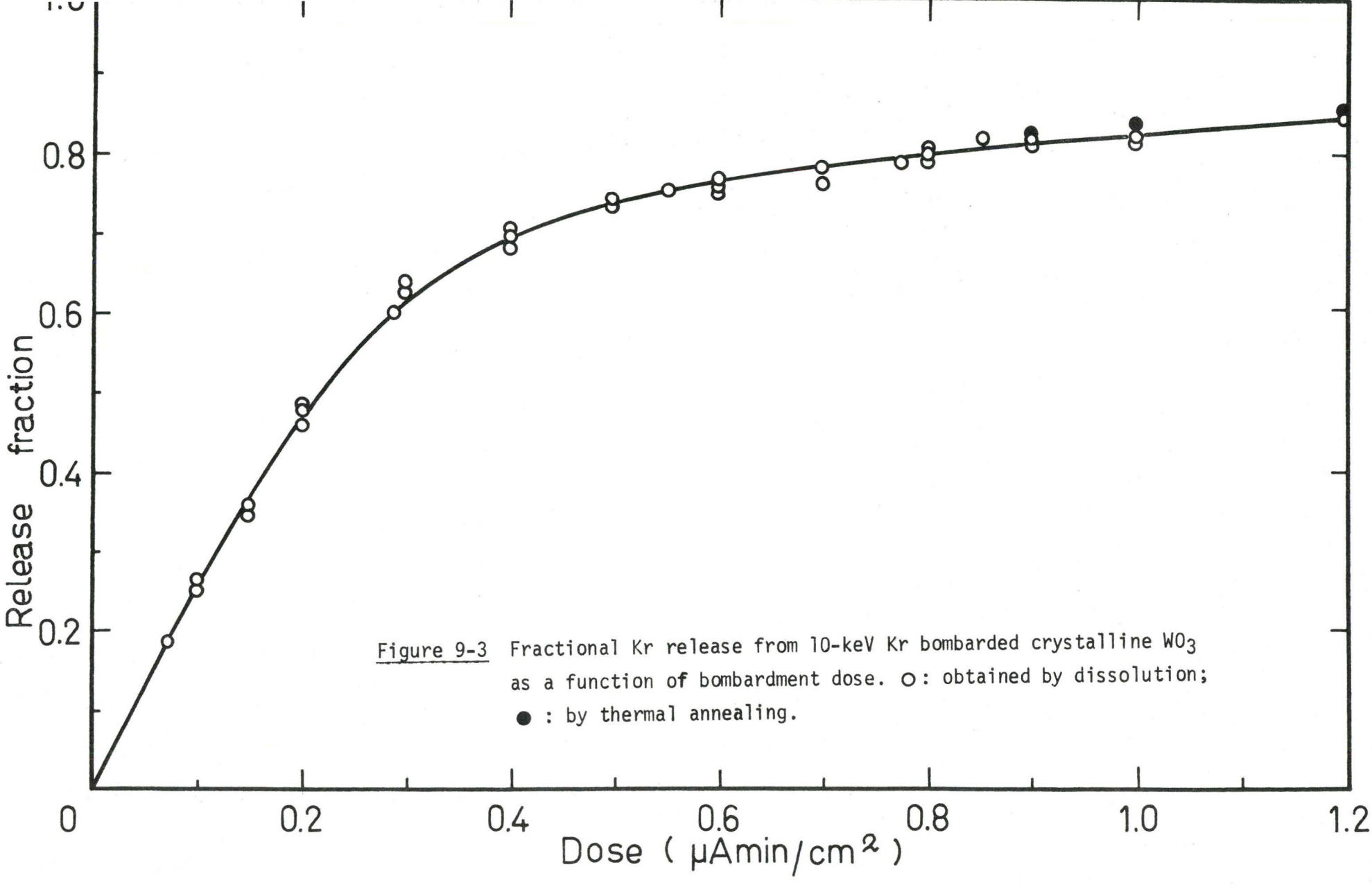

Figure 9-3 Fractional Kr release from 10-keV Kr bombarded crystalline WO_3 as a function of bombardment dose. ○: obtained by dissolution; ● : by thermal annealing.

(b) Time for Dissolution: An alternative estimate of R_a was made involving the direct use of the dissolution rate of 5.5 ± 0.1 Å/sec. for bombardment doses $\leq 1 \times 10^{15}$ ions/cm^2 and of 3.2 ± 0.1 Å/sec. for a dose of 3.5×10^{15} ions/cm^2, as given in Figure 8-4. Various 65-volt specimens were bombarded with 4- to 35-keV Kr and were then immersed in dilute KOH. Those which were either unheated or heated to 200°C (Figure 9-4A) yielded, as would be expected, what is simply an integral ion depth distribution, the observed mean ranges being summarized in column 2 of Table 9-2. Specimens exposed at 300°C (Figure 9-4B) showed a slight tendency for the dissolution rate to change after about 25 sec., but may be concluded to have retained most of the natural disorder associated with amorphousness. Specimens exposed at 350 or 450°C, on the other hand, gave markedly different behaviour as in Figures 9-4C, D,and E. The dissolution is seen to stop abruptly after 18-49 sec., at which point (as argued previously by Jech[108]), the disordered surface layer may be assumed to be completely removed. Such removal was confirmed by scanning electron microscopy as in Figure 9-5 and enabled R_a to be deduced simply from the known dissolution rates.

(c) Residual Kr Activity After Dissolution: A variation of the above approach, previously used by Jech[108] in a study of mica, is to match the "knee" activities in dissolution curves (e.g. Figures 9-4C, D, and E) with the corresponding activities in integral ion distributions (e.g. Figure 9-4A). This approach has the advantage of being independent of bombardment-induced solubility changes.

(d) Residual Kr Activity after Thermal Annealing: The simple gas-release spectra of Figures 9-1B and C make possible still a further

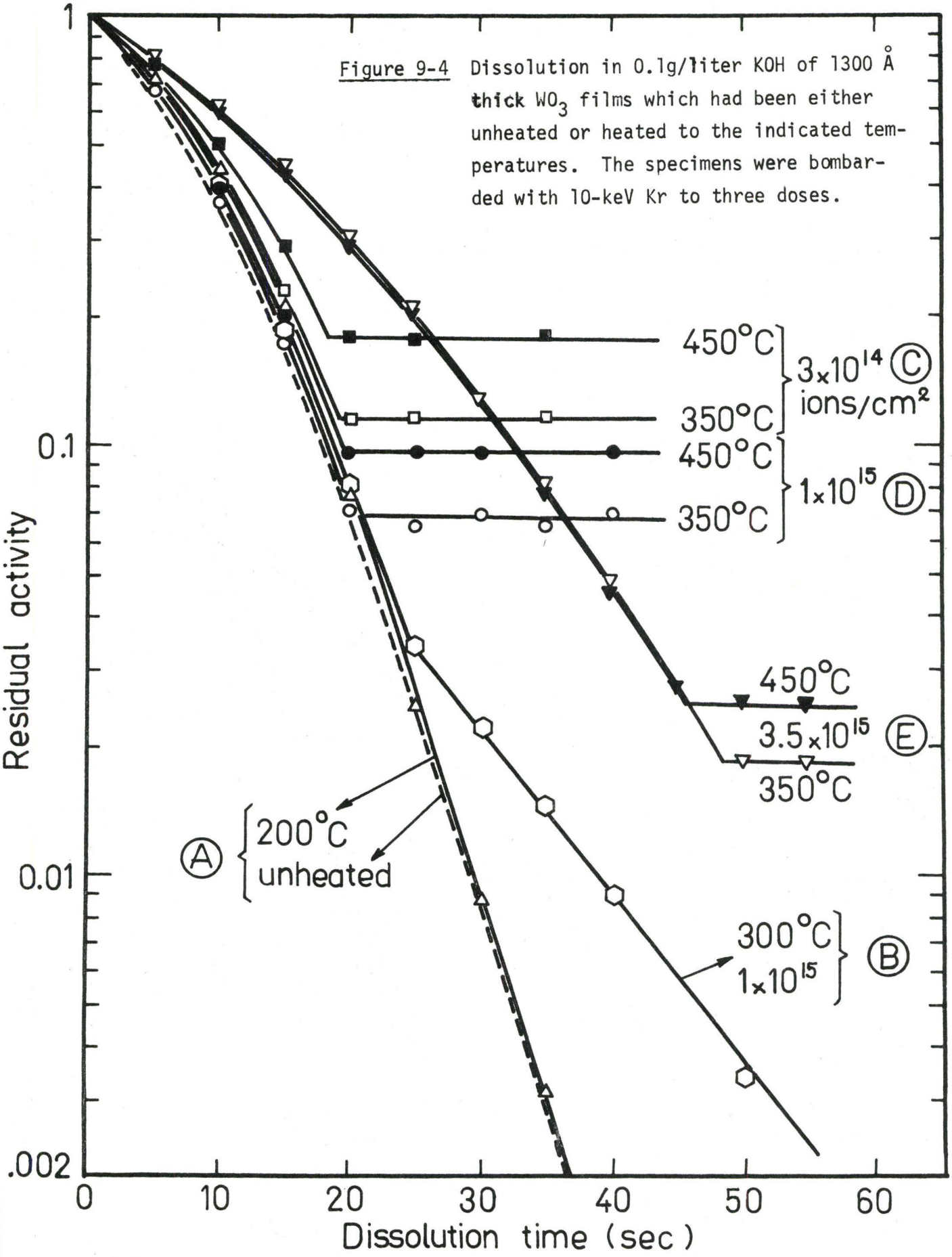

Figure 9-4 Dissolution in 0.1g/liter KOH of 1300 Å thick WO_3 films which had been either unheated or heated to the indicated temperatures. The specimens were bombarded with 10-keV Kr to three doses.

Figure 9-5

Surface topography after dissolution of disordered WO_3 in 0.1 g/liter KOH.

TABLE 9-1

The Depth of Amorphization (R_a) for WO_3 following 10-keV Kr Bombardment

Preparation Temperature of WO_3 (°C)	Kr Dose (ions/cm^2)	R_a from Interference Colors	R_a from Time for Dissolution	R_a from Activity After Dissolution	R_a from Activity After Annealing	$\langle R_a \rangle$
350	3×10^{14}	105 Å	105 Å	100 Å	100 Å	103
450		105	100	85	100	98
350	1×10^{15}	115	110	115	110	113
450		115	105	105	120	111
350	3.5×10^{15}	130	155	154	130	142
450		130	147	140	140	139

estimate of R_a. Thus the residual activity left after the annealing stage at 550°C but before the onset of normal diffusion at $\sim$ 650°C (e.g. Figures 9-1B and C) can be matched to an integral ion distribution. An important assumption here is that the crystallization process should involve unidirectional motion of the underlying crystalline WO_3 towards the surface with resultant expulsion of the inert gas when crystallization is complete. Since it is not self-evident that this would be so, we would regard the gas-release based estimates of R_a as the least reliable.

9.2 RESULTS

Table 9-1 shows the detailed results for 10-keV, while Figure 9-6 summarizes the values of R_a as obtained for a variety of energies. Agreement amongst the different techniques to within about ± 10 Å is indicated, even the gas release estimates of R_a being satisfactory.

9.3 DISCUSSION

9.3.1 Description of Amorphization by Particle Impact

The formation by particle impact of an amorphous phase can be described in several ways. For example, (a) it may be attributed to the random impingement of discrete disordered regions, perhaps the same entities as those observed by electron microscopy[131], such that, for a fractional coverage near unity, a planar amorphous-crystalline interface results at depth $x = R_a$ (Figure 9-7a)[132]. (b) A second model, closely related to the preceding, is one which attempts to describe how, as in Figure 9-7b, the random impingement of discrete disordered regions leads to amorphization which is continuous with the surface[133]. This model is of interest in connection with experiments which measure, instead of the depth of amorphization, the extent to which disorder causes the re-

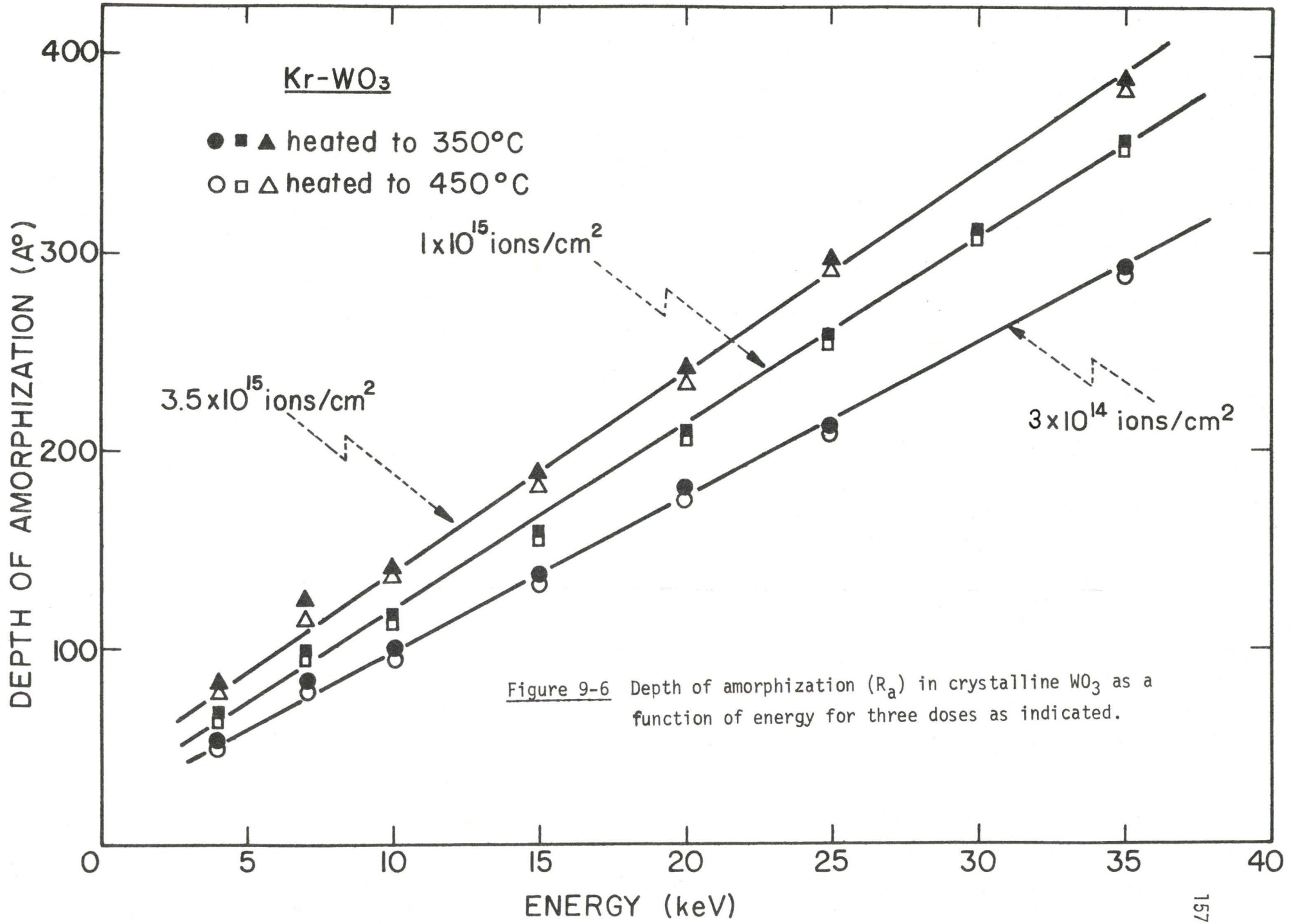

Figure 9-6 Depth of amorphization (R_a) in crystalline WO_3 as a function of energy for three doses as indicated.

lease of an inert marker by dissolution or thermal annealing[111] (our methods b,c, and d). (c) Again, similar to the preceding, several authors [82,134] have visualized amorphization as being due to the opposing tendencies of disordering due to displacements and crystallization due to thermal effects. The main differences were that Kelly and Naguib[82] considered thermal spikes as the source of heat and crystal growth as the annealing phenomenon; Morehead and Crowder[134], by contrast, emphasized the motion of point defects at the bombardment temperature. (d) As an alternative to these three models, amorphization might be described as occurring whenever the initial fraction of atoms which are displaced in any small volume element exceeds a critical value. Here the term "initial" means "present before thermal and athermal annealing". This model, which has been discussed by Kelly and the author[129], should lead to the usual planar interface at $x = R_a$ (Figure 9-7c). (e) Finally, one can envisage the formation of an amorphous phase as depending on whether the final fraction of displaced atoms, i.e. which remain after annealing, exceeds a critical value which is probably rather less than unity. This model is essentially equivalent to that discussed elsewhere in connection with Si[135], SiO_2[136], and Al_2O_3, C, and $ZrSiO_4$[111].

Models (a) to (c) will, for the present purposes, be described as involving discrete disordered regions. Likewise, models (d) and (e) will be said to be characterized by homogeneous damage accumulation.

9.3.2 Comparison of the Depth of Amorphization, R_a, with Damage Moments

The most direct basis of comparison of the estimates of R_a for Kr-WO_3 is with either the damage mean range, $\langle x_d \rangle$, or with the sum $\langle x_d \rangle + \mu_{2d}^{1/2}$, where μ_2 stands for $\langle \Delta x^2 \rangle = \langle (x - \langle x \rangle)^2 \rangle$. Since the maximum

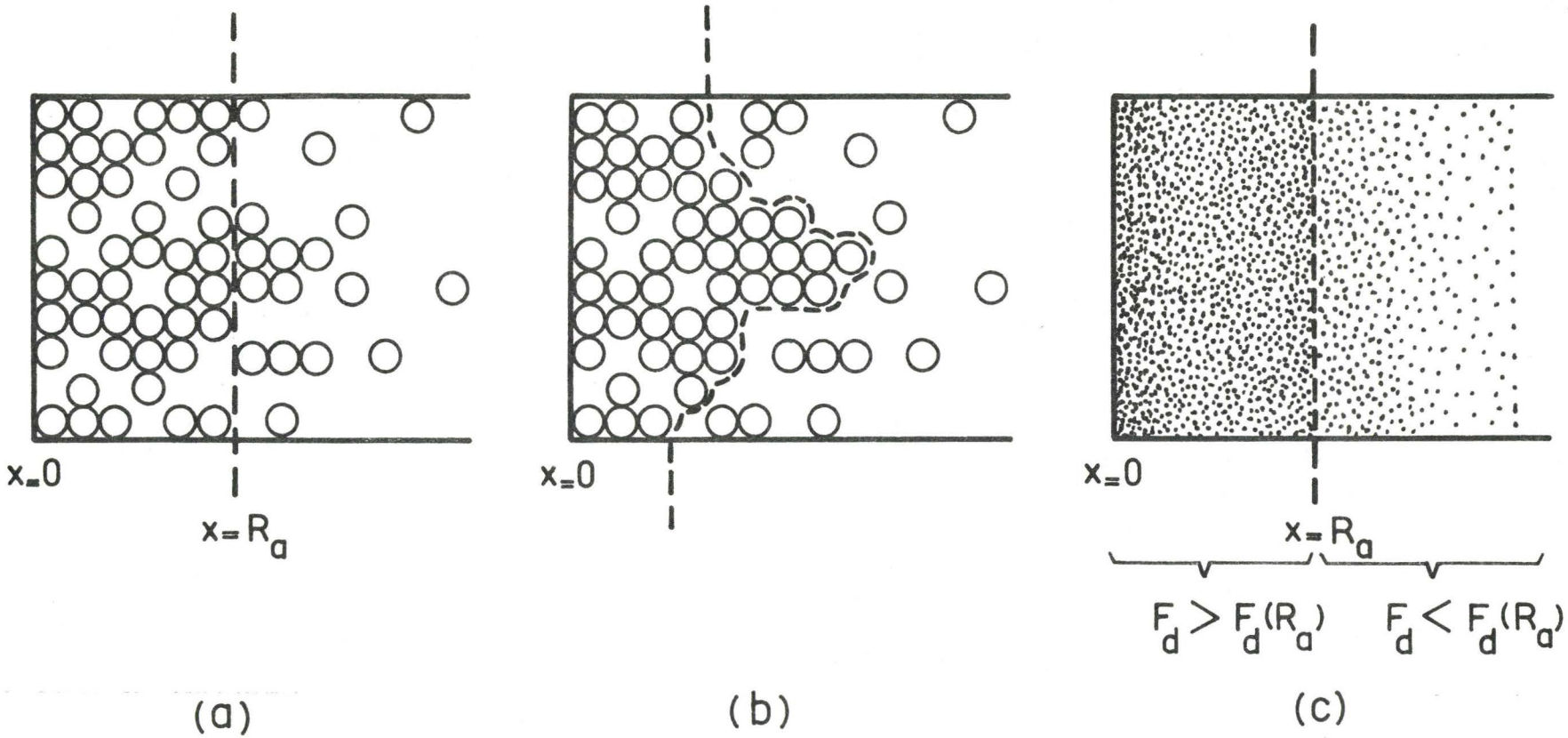

Figure 9-7 Formation of bombardment-induced amorphization in the near-surface region of a solid.

TABLE 9-2

Parameters Relating to Sections 9.3.2 and 9.3.3

E (keV)	Experim. mean range, $\langle R_i \rangle$+ (Å)	$\langle x_d \rangle$ [from eq.(9-1)] (Å)	$\mu_{2d}^{1/2}$ [from eq.(9-2)] (Å)	$R_a/\langle x_d \rangle$ (for 10^{15} ions/cm^2)	$R_a/(\langle x_d \rangle + \mu_{2d}^{1/2})$ (for 10^{15} ions/cm^2)	$F_d(R_a)$ [eq.(9-5)] (for all doses)
4	25	26	18	2.5	1.5	0.09
7	36	38	26	2.3	1.4	0.12
10	45	48	33	2.5	1.5	0.13
15	85	63	43.5	2.6	1.6	0.12
20	118	76	53	2.8	1.7	0.09
25	143	88.5	61.5	3.0	1.8	0.08
35	196	110.5	76.5	3.3	1.9	0.06

+ The conversion from $\mu g/cm^2$ to Å was made by assuming a density of 6.8 g/cm^3 for WO_3. Median ranges were converted to mean ranges, $\langle R_i \rangle$ by multiplying by 1.19. This factor applies for an xe^{-x}-type distribution, which can be shown to be much better than a Gaussian for describing our experimental results.

energy that we used was 35 keV, which corresponds to $\varepsilon = 0.11 < 0.2$, the power-law approximation with $m = 1/3$ can be employed with accuracy[25]. The damage moments can in principle be deduced from Figure 4-4; far simpler, however, is to use the following formulae which were kindly supplied by Winterbon[117]:

$$\langle x_d \rangle = 0.702\ E^{2/3} + 0.00787\ E^{14/9} + \ldots (\text{in } \mu g/cm^2) \quad (9\text{-}1)$$

$$\mu_{2d}/\langle x_d \rangle^2 = 0.482 + 0.00591\ E^{8/9} + \ldots . \quad (9\text{-}2)$$

where E is the Kr energy in keV. Partial results are given in columns 3 to 6 of Table 9-2.

We conclude, by considering all results, that $R_a/\langle x_d \rangle$ lies between 2.5 and 3.3, depending on the energy and dose, while $R_a/(\langle x_d \rangle + \mu_{2d}^{1/2})$ is also distinctly greater than unity. The damage mean range, as well as the sum $\langle x_d \rangle + \mu_{2d}^{1/2}$, are thus <u>not</u> realistic estimates for the depth at which the massive damage, which leads to the amorphization of WO_3, ceases. Rather, amorphization extends to a somewhat greater depth, the value depending upon the energy and ion dose.

9.3.3 Evaluation of $F_d(R_a)$, the Initial Displacement Fraction at $x = R_a$

The failure of a simple identification of R_a with $\langle x_d \rangle$ or $\langle x_d \rangle + \mu_{2d}^{1/2}$ suggests that the detailed damage distribution must be taken into account. One way of doing this is to consider $F_d(R_a)$, the fraction of atoms which is initially displaced at $x = R_a$. The details of estimating $F_d(R_a)$ for WO_3 are as follows: One first evaluates $C_d(R_a)$, the initial deposited-energy concentration at $x = R_a$, on the basis of a differential

Edgeworth expansion (Section 4.3.4):

$$C(x)dx = (dx)(2\pi\mu_2)^{-1/2}[\exp(-\xi^2/2)]f(\xi) \qquad (9\text{-}3)$$

with

$$f(\xi) \simeq 1 - 1/6(\mu_3/\mu_2^{3/2})(3\xi - \xi^3) + \frac{1}{24}(\mu_4/\mu_2^2 - 3)(3 - 6\xi^2 + \xi^4) - \frac{1}{72}(\mu_3^2/\mu_2^3)(15 - 45\xi^2 + 15\xi^4 - \xi^6) \qquad (9\text{-}4)$$

where ξ stands for $(\langle x\rangle/\mu_2^{1/2})(x/\langle x\rangle - 1)$. $\langle x_d\rangle$ and $\mu_{2d}^{1/2}$ are evaluated as in equations (9-1) and (9-2), $\langle x_d\rangle/\mu_{2d}^{1/2}$ is given the value 1.44 (independent of the energy), while $\mu_{3d}/\mu_{2d}^{3/2}$ and μ_{4d}/μ_{2d}^{2} are assigned the values 0.82 and 3.73 (approximated by adding 1/4 of the corresponding quantity for Kr-W to 3/4 of the value for Kr-O, both values having been taken from Figure 4-4b and c). With $C_d(R_a)$ known, $F_d(R_a)$ follows as:

$$F_d(R_a) = 1 - \exp\{-\frac{0.8Bt\nu(E)\ C_d(R_a)}{2E_dN}\} \qquad (9\text{-}5)$$

Here the exponential form serves to correct for repeated displacement of the same atoms, 0.8 is Sigmund's correction to $E/2E_d$ [137], Bt is the ion dose, $\nu(E)$ is that part of E leading to nuclear collisions (estimated from Figure 3 of reference 138), E_d is the displacement energy (which may be taken as roughly 50 eV for WO_3, cf. Al_2O_3 [139] and SiO_2 [140]), and N is the atomic density.

Average results valid for all doses are given in final column of Table 9-2.

We conclude that $F_d(R_a)$ is best described as being constant, i.e.

as lying within a factor of two of 0.1. Similar constancy was suggested elsewhere[129] to be characteristic also of the bombardment of Si, and there is reason to expect this to be true of other substances. A possible general conclusion is that models for amorphization based on homogeneous damage accumulation (i.e. models (d) and (e)) are self-consistent.

9.3.4 Evaluation of the Mean Size of Disordered Regions

A second way of taking the detailed damage distribution into account is based on the postulate that the formation of an amorphous phase results from the random impingement of discrete disordered regions (models (a) to (c)). Such an approach is obviously not quite "assumption free", though still has good precedent. On its basis it is possible to estimate $V_a^{1/3}$, the mean size of the assumed disordered regions. Thus it is a simple matter to argue that each ion impact will disorder a volume V_a distributed according to equation (9-3). (In fact, this is not strictly correct. A correlated distribution function, as discussed by Westmoreland and Sigmund[141], would be preferable.) The fractional amorphization at depth R_a is accordingly:

$$F_a(R_a) = 1 - \exp[-BtV_aC_d(R_a)] \qquad (9\text{-}6)$$

which allows for random impacts as in equation (9-5). The resulting estimates of $V_a^{1/3}$, deduced from equation (9-6) with $F_a(R_a)$ set somewhat arbitrarily equal to 0.5, are given in column 2 of Table 9-3.

The constancy of $F_d(R_a)$, as shown by the use of equation (9-5), implies that V_a has an energy dependence:

$$V_a \propto \nu(E) \overset{\sim}{\propto} E \qquad (9\text{-}7)$$

TABLE 9-3

Parameters Relating to Sections 9.3.4 and 9.3.5

E (keV)	$V_a^{1/3}$ [equation(9-6)] (for all doses)	$\frac{V_a^{1/3}}{E^{1/3}}$	$\langle x_d \rangle_{exp.}$ [equation(9-10)]	$\langle x_d \rangle_{theor.}$ [equation(9-1)]
4	14 Å	8.8	23 Å	26
7	15	7.9	27	38
10	17	7.9	36	48
15	20	8.1	48	63
20	24	8.8	61	76
25	27	9.2	78	88.5
35	34	10.4	100	110.5

while this can also be shown by dividing $V_a^{1/3}$ by $E^{1/3}$ as in column 3 of Table 9-3. Interestingly, a similar energy dependence follows from the ideas of Morehead and Crowder[134], which lead to the result:

$$V_a \propto \langle x_d \rangle \cdot \frac{dE}{dx} \tag{9-8}$$

By substituting power-law values of $\langle x_d \rangle$ and dE/dx, namely:

$$\langle x_d \rangle \propto R_i$$

$$\propto \frac{1-m}{2mC\Lambda^{1-m} N} E^{2m}$$

$$\frac{dE}{dx} \propto S_n(E)$$

$$\propto \frac{C\Lambda^{1-m}}{1-m} E^{1-2m}$$

we find $V_a \propto E$ for all m.

This is not the only possible description of V_a, however, a reasonable alternative being:

$$V_a \propto \mu_{2d}^{1/2} \langle y_d^2 \rangle \propto E^2 \tag{9-9}$$

where m = 1/3 is used and $\langle y_d^2 \rangle$ describes damage straggling perpendicular to the incident direction.

In conclusion, a description of the amorphization process based on the random impingement of disordered regions cannot be justified as convincingly as the model of Section 9.3.3. The corresponding models, (a) to (c), therefore rest on shakier ground.

9.3.5 Evaluation of $\langle x_d \rangle$

The essence of Sections 9.3.3 and 9.3.4 was to take theoretical estimates of $\langle x_d \rangle$ and then deduce the parameters $F_d(R_a)$ and $V_a^{1/3}$. Note-

worthy was the fact that $F_d(R_a)$ tended to be nearly constant. This would suggest that the procedures could have been reversed so as to yield $\langle x_d \rangle$ explicitly. Thus we will postulate that R_a occurs at that depth where the displacement fraction achieves a critical (but otherwise unspecified) value. Then, it follows that for a series of estimates of R_a for different doses, though the same energy, the following quantity must remain constant:

$$\gamma = (Bt) \exp(-\xi^2/2) f(\xi) \qquad (9\text{-}10)$$

Since equation (9-10) is a function of four independent moments or moment ratios, we will simplify the problem by giving $\langle x_d \rangle / \mu_{2d}^{1/2}$ and the higher moment ratios their power-law values for m = 1/3. Equation (9-10) can then, by trial-and-error methods, be used to deduce $\langle x_d \rangle$ with results as in the column 4 of Table 9-3.

We conclude that the experimental $\langle x_d \rangle$ values are, for all energies, surprisingly similar to those deduced from the theory of Winterbon, Sigmund, and Sanders[25], as reproduced in the final column of Table 9-3. Apparently, measurements of R_a constitute a particularly sensitive means to estimating $\langle x_d \rangle$; moreover, had a wider range of doses been used, or the data been of higher precision, one could probably have obtained both $\langle x_d \rangle$ and $\mu_{2d}^{1/2}$.

CHAPTER 10

SUMMARY

1. The sputtering coefficient, S, due to Kr bombardment of the amorphous anodic oxides Nb_2O_5, Ta_2O_5, and WO_3 has been determined for ion energies of 2-30 keV. Three methods were employed, based respectively on (a) the change of interference colors, (b) the perforation of a film of free oxide by an intense ion beam,and (c) the loss of weight of the target.

2. The sputtering coefficients of 10-keV Kr on other anodic oxides, Al_2O_3, MoO_3, SiO_2, TiO_2, V_2O_5, and ZrO_2, have also been estimated.

3. The values of S for Kr on Al_2O_3, Nb_2O_5, SiO_2, Ta_2O_5, TiO_2, and ZrO_2 were small, ranging from 1.6 to 4.2 atoms/ion at 10 keV. S for Kr on MoO_3, V_2O_5 and WO_3, on the other hand, was a factor of three larger, e.g. 9.2 to 12.7 atoms/ion at 10 keV.

4. The interpretation of the experimental results in terms of the recently formulated theory of Sigmund, which is completely analytical, permitted the surface binding energies to be defined with the oxides studied. The calculated surface binding energies were comparable to the heat of atomization for normal oxides; a factor-of-three difference, however, was found in the case of the oxides MoO_3, V_2O_5, and WO_3. We would propose that the deviant behaviour of the latter three oxides is due to their volatility, i.e. the volatility has apparently made an important contribu-

tion to the sputtering process.

5. A pronounced "range shortening" for high doses of Kr in Al_2O_3, Nb_2O_5, and WO_3 has been observed for room-temperature bombardments.

6. Migration of implanted dopants has been demonstrated to occur near room temperature with a wide variety of materials, including Al_2O_3, Nb_2O_5, Ta_2O_5, WO_3, and ZrO_2, and this suggests that "range shortening" may be a diffusion phenomenon.

7. The effects of prebombardment and post-bombardment have been studied with Kr and O_2. Post-bombardment with O_2 caused first a "range lengthening" at low dose, then, at high enough doses, a "range shortening". This experiment is important in emphasizing the dual effects of high-dose bombardments on range profiles, i.e. both deepening and shortening can occur.

8. High-dose bombardment at low temperatures (-30 and -75°C) also showed the "range shortening"; the effect was postponed, however, until significantly higher doses than in room-temperature implants. This is further evidence (besides the experiment mentioned in 6) that a diffusion effect may be involved.

9. The distribution profile for low-dose bombardments at high temperatures (200,300,400, and 500°C) revealed the "rotation effect" corresponding to normal diffusion, whereas the high-dose profiles still

showed the surface-directed motion of implanted Kr.

10. The above-mentioned "range shortening" has been shown analytically to be reasonable whenever there is a spatial variation in the diffusion activation enthalpy.

11. Putting the results summarized in 5 to 10 together, we have concluded that "range shortening" is a diffusional phenomenon. It is analogous to ordinary radiation-enhanced diffusion, except in so far as it is governed by spatially-varying diffusion coefficient.

12. Depths of amorphization due to ion impact have been measured with anodic WO_3 (crystallized at 350 or 450°C) using four techniques based on the bombardment-induced solubility and thermal annealing of the disordered surface layers.

13. The depth was found to vary linearly with energy, with values ranging from 50 ± 15 Å for a medium dose (3×10^{14} ions/cm^2) bombardment with 4-keV Kr to 395 ± 15 Å for a high-dose (3.5×10^{15} ions/cm^2) bombardment at 35 keV. The amorphization thus extends to about 2.3 to 3.3 times the damage mean range, the latter being taken as essentially that from the theory of Winterbon, Sigmund, and Sanders.

14. A more detailed application of damage-distribution theory permits, firstly, the fraction of atoms initially displaced at the amorphous-crystalline boundary to be estimated. It was found to lie within a

factor of two of 0.1, and it was therefore concluded that models for amorphization based on homogeneous damage accumulation are self-consistent.

15. Secondly, if it may be assumed that amorphization is due to the random impingement of discrete disordered regions, damage-distribution theory yields values for the mean size of the regions (14 to 34 Å).

16. Thirdly, and most important, damage-distribution theory enables an explicit evaluation of the damage mean range for Kr-WO_3. The values for 4,10,20, and 35 keV Kr-WO_3 are 23,36,61, and 100 Å, as compared with theoretical predictions of 26,48,76, and 110 Å. These are probably amongst the more accurate damage ranges that have been measured to date.

REFERENCES

1. G.K. Wehner and D. Rosenberg, J. Appl. Phys. 32, 887 (1961).
2. O. Almén and G. Bruce, Nucl. Instr. Methods 11, 257 (1961).
3. P.D. Davidse and L.I. Maissel, J. Vac. Sci. Technol. 4, 33 (1967).
4. O. Gautsch, C. Mustacchi, and H. Wahl, Euratom Rept. Eur. 2515.e.
5. E.H. Hasseltine, F.C. Hurlbut, N.T. Olson, and H.P. Smith, J. Appl. Phys. 38, 4313 (1967).
6. R. Kelly, Can. J. Phys. 46, 473 (1968).
7. L.Q. Nghi and R. Kelly, Can. J. Phys. 48,137 (1970).
8. B.V. Panin and V.G. Tel'kovskii, Soviet Phys. - Solid State, 8, 1031 (1966).
9. P. Sigmund, Phys. Rev. 184, 383 (1969).
10. R. Kelly, Prof. Intern. Conf. Applications of Ion Beams to Semiconductor Technology, p. 201 (Editions Ophrys, Gap, France, 1967).
11. J.A. Davies, L. Eriksson, and J.L. Whitton, Can. J. Phys. 46, 573 (1968).
12. R. Kelly and L. Q. Nghi, Rad. Effects, 6, 247 (1970).
13. L.T. Chadderton, Radiation Damage in Crystals, Chapter 6, pp. 114-138 (Methuen, London, 1965).
14. M.W. Thompson, Defects and Radiation Damage in Metals, Section 4.2 (Cambridge University Press, London, 1969).
15. P.T. Wedepohl, Rad. Effects 1, 77 (1969).
16. A.A. Abrahamson, unpublished (1966).
17. R.S. Nelson, The Observation of Atomic Collisions in Crystalline Solids, p.12 (North-Holland Publishing Company, Amsterdam, 1968).

18. K.B. Winterbon, Chalk River (Canada) Report AECL-3194 .

19. O.B. Firsov, Soviet Phys.-JETP, 5, 1192 (1957).

20. O.B. Firsov, Soviet Phys.-JETP 6, 534 (1958).

21. P. Gombas, Statistische Theorie des Atoms und Ihre Anwendungen, p. 127 (Springer-Verlag, Vienna, 1949) .

22. A.A. Abrahamson, Phys. Rev. 130, 693 (1963).

23. P.T. Wedepohl, Proc. Phys. Soc. 92, 79 (1967).

24. J. Lindhard, V. Nielsen, and M. Scharff, Kgl. Danske Videnskab. Selskab., Mat.-Fys. Medd. 36, no. 10 (1968).

25. K.B. Winterbon, P. Sigmund, and J.B. Sanders, Kgl. Danske Videnskab. Selskab., Mat.-Fys. Medd. 37, no. 14 (1970).

26. M.W. Thompson, same as reference 14, section 4.3 .

27. J. Lindhard, M. Scharff, and H.E. Schiøtt, Kgl. Danske Videnskab. Selskab, Mat.-Fys. Medd. 33, no. 14 (1963).

28. P. Sigmund and J.B. Sanders, Proc. Intern. Conf. on Applications of Ion Beams to Semiconductor Technology, p. 215 (Editions Ophrys, Gap, France, 1967).

29. M.W. Thompson, Phil. Mag. 18, 377 (1968).

30. G.K. Wehner, J. Appl. Phys. 30, 1762 (1959).

31. V.A. Molchanov and V.G. Tel'kovskii, Soviet Phys.-Doklady 6, 137 (1961).

32. P.K. Rol, J.M. Fluit and J. Kistemaker, Physica 26, 1000 (1960).

33. P.K. Rol, J.M. Fluit, and J. Kistemaker, Physica 26, 1009 (1960).

34. E.T. Pitkin, Progr. Astron. Rocketry 5, 195 (1961).

35. K. Kopitzki and H.E. Stier, Z. Naturforsch. 16a, 1257 (1961).

36. K. Kopitzki and H.E. Stier, Z. Naturforsch. 17a, 346 (1962).

37. K. Kopitzki and H.E. Stier, Phys. Letters 4, 232 (1963).

38. F. Keywell, Phys. Rev. 97, 1611 (1955).

39. D.T. Goldman and A. Simon, Phys. Rev. 111, 383 (1958).

40. R.S. Pease, Rendiconti S.I.F. Corso 13, 158 (1960).

41. D.D. Odintsov, Soviet Phys.-Solid State 5, 813 (1963).

42. D. Onderdelinden, F.W. Saris, and P.K. Rol, Nucl. Instr. Methods 38, 269 (1965).

43. D. Onderdelinden, F.W. Saris, and P.K. Rol, Proc. 7th Intern. Conf. Phenomena in Ionized Gases, vol. 1, Belgrade (1966).

44. D. Onderdelinden, Can. J. Phys. 46, 739 (1968).

45. Yu. V. Martynenko, Soviet Phys.-Solid State 6, 1581 (1965).

46. P. Sigmund, Bull. Am. Phys. Soc. 13, 1445 (1968).

47. G.H. Kinchin and R.S. Pease, Rept. Prog. Phys. 18, 1 (1955).

48. G.K. Wehner, G.S. Anderson, and C.E. Kenknight, Surface Bombardment Studies, USAEC Report no. 3031, p. 76 (1966).

49. J.B. Sanders, Can. J. Phys. 46, 455 (1968).

50. P. Sigmund, Can. J. Phys. 46, 731 (1968).

51. E.M. Baroody, J. Appl. Phys. 46, 3565 (1965).

52. H.E. Schiøtt, Kgl. Kanske Videnskab. Selskab., Mat-Fys. Medd. 35, no. 9 (1966).

53. H.E. Schiøtt, Private communication (1970).

54. P.V. Pavlov, D.I. Tetel'baum, E.I. Zorin, and V.I. Alekseer, Sov. Phys.-Solid State 8, 2141 (1967).

55. D.K. Brice, Appl. Phys. Letters 16, 103 (1970).

56. A.R. Sattler and F.L. Vook, Phys. Rev. 173, 435 (1968).

57. H.J. Stein, F.L. Vook, and J.A. Borders, Appl. Phys. Letters 16, 106 (1970).

58. K.L. Brower, F.L. Vook, and J.A. Borders, Appl. Phys. Letters 16, 108 (1970).

59. D.K. Brice, Rad. Effects (in press).

60. R. Kelly and Hj. Matzke, J. Nucl. Mat. 20, 171 (1966).

61. G. Di Cola and Hj. Matzke, Nucl. Instr. Methods 57, 341 (1967).

62. D.G. Hurst, Chalk River (Canada) Report CRRP-1124 (1962).

63. H. Gaus, Z. Naturforsch. 20a, 1298 (1965).

64. R. Kelly and E. Ruedl, Phys. Stat. Sol. 13, 55 (1966).

65. Hj. Matzke, Z. Naturforsch. 22a, 507 (1967).

66. J.M. Fairfield and B.L. Crowder, Trans. Met. Soc. AIME 245, 469 (1969).

67. O. Meyer and J.W. Mayer, J. Appl. Phys. 41, 4166 (1970).

68. P.P. Pronko and R. Kelly, Rad. Effects 3, 161 (1970).

69. H.S. Carslaw and J.C. Jaeger, Conduction of Heat in Solids, pp. 87-370 (Oxford University Press , Oxford, 1959).

70. M.J. Norgett and A.B. Lidiard, Phil. Mag. 18, 1193 (1968).

71. D.I.R. Norris, Proc. Intern. Conf. on Atomic Collision Phenomena in Solids p. 97 (North-Holland; Amsterdam, 1970).

72. R. Kelly and Hj. Matzke, J. Nucl. Mat. 17, 179 (1965).

73. E. Jahnke, F. Emde, and F. Loesch, Tables of Higher Functions, p. 193 (McGraw-Hill, New York, 1960).

74. J.A. Davies, J. Friesen, and J.D. McIntyre, Can. J. Chem. 38, 1526 (1960).

75. M.R. Arora, M.Sc. thesis, McMaster University (1971).

76. F. Kover and M.J. Musselin, Revue Générale de l'Electricité 76,793 (1965).

77. E.F. Duffek, E.A. Benjamini, and C. Mylroie, Electrochem. Technol. 3 75 (1965).

78. I. Reid and R. Kelly, unpublished.

79. E. Giani and R. Kelly, unpublished.

80. R.E. Pawel, Rev. Sci. Instr. 35, 1066 (1964).

81. M. McCargo, J.A. Davies and F. Brown, Can. J. Phys. 41, 1231 (1963).

82. R. Kelly and H.M. Naguib, Proc. Intern. Conf. on Atomic Collision Phenomena in Solids, p. 172 (North-Holland, Amsterdam, 1970).

83. D.A. Vermilyea, Acta. Met. 1, 282 (1953).

84. V.A. Lavrenko, Russ. J. Phys. Chem. 35, 537 (1961).

85. J.P.S. Pringle, private communication (1969).

86. J.A. Davies, G.C. Ball, F. Brown, and B. Domeij, Can. J. Phys. 42, 1070 (1964).

87. F. Brown, G.C. Ball, D.A. Channing, L.M. Howe, J.P.S. Pringle and J.L. Whitton, Nucl. Instr. Methods 38, 249 (1965).

88. J.C. Banter, J. Electrochem. Soc. 114, 508 (1967).

89. C. Jech, Intern. J. Appl. Radiation and Isotopes 8, 179 (1960).

90. R.E. Nielsen and W.B. Shepherd, Rev. Sci. Instr. 35, 123 (1964).

91. A.J. Schrijner and A. Middelhoek, J. Electrochem. Soc. 111, 1167 (1964).

92. L. Young, Anodic Oxide Films, pp. 272-273 (Academic Press, London, 1961).

93. B. Domeij, F. Brown, J.A. Davies, and M. McCargo, Can. J. Phys. 42, 1624 (1964).

94. A.K. Vijh, J. Electrochem. Soc. 116, 353 (1969).

95. O. Kubaschewski, E.L. Evans, and C.B. Alcock, Metallurgical Thermochemistry, fourth edition, pp. 303-420 (Pergamon Press, Oxford 1967).

96. M.W. Thompson and R.S. Nelson, Phil. Mag. 7, 2015 (1962).

97. L.I. Maissel and R. Glang, Handbook of Thin Film Technology, 1st edition, pp. 1-65 to 1-69 (McGraw-Hill, New York, 1970).

98. H. Schirrwitz, Beitr. Plasmaphysik 2, 188 (1962).

99. D. Rosenberg and G.K. Wehner, J. Appl. Phys. 33, 1842 (1962).

100. M.I. Guseva, Radio Eng. Elect. Phys. 7, 1563 (1962).

101. N. Laegreid and G.K. Wehner, J. Appl. Phys. 32, 365 (1961).

102. C.E. Carlston, G.D. Magnuson, A. Comeaux, and P. Mahadevan, Phys. Rev. 138, A759 (1965).

103. O.C. Yonts, C.E. Normand, and D.E. Harrison, J. Appl. Phys. 31 447 (1960).

104. E.T. Pitkin, Progr. Astron. Rocketry 5, 195 (1961).

105. B.M. Gurmin, T.P. Martynenko, and Yu. A. Ryzhov, Soviet Phys.-Solid State 10, 324 (1968).

106. B.H. Hill, J. Electrochem. 116, 668 (1969).

107. U.F. Gianola, J. Appl. Phys. 28, 868 (1957).

108. C. Jech, Phys. Stat. Sol. 21, 481 (1967).

109. C. Jech, Phys. Stat. Sol. 27, 573 (1968).

110. R.L. Fleischer, P.B. Price, and R.M. Walter, Science, 149, 385 (1965).

111. C. Jech and R. Kelly, J. Phys. Chem. Sol. 31, 41 (1970).

112. C. Jech and R. Kelly, Proc. Brit. Ceram. Soc. No.9, 259 (1967).

113. C. Jech and R. Kelly, J. Phys. Chem. Sol. 30, 465 (1969).

114. J.C. Pfister, in Radiation Damage in Semiconductors, p. 281, (Dunod, Paris, 1965).

115. A. Brelot, in Radiation Effects in Semiconductors, p. 460, (Plenum Press, New York, 1968).

116. R. Kelly, Phys. Stat. Sol. 30, 37 (1968).

117. K.B. Winterbon, private communication (1971).

118. J.L. Whitton and Hj. Matzke, Can. J. Phys. 44, 2905 (1966).

119. K. Erents and G. Carter, Vacuum 17, 97 (1967).

120. R.S. Nelson, J. Nucl. Mat. 25, 227 (1968).

121. R. Kelly and C. Jech, J. Nucl. Mat. 30, 122 (1969).

122. Hj. Matzke and C. Jech, J. Phys. Chem. Sol. 31, 753 (1970).

123. K. Erents and G. Carter, Vacuum 17, 215 (1967).

124. E.V. Kornelsen, Can. J. Phys., 42, 364 (1964).

125. L.H. James and G. Carter, Brit. J. Appl. Phys. 14, 147 (1963).

126. D.E. Davies, Solid-State Electronics 13, 229 (1970).

127. H.M. Naguib and R. Kelly, unpublished.

128. L.Q. Nghi and R. Kelly, submitted to Can. J. Phys.

129. R. Kelly and L.Q. Nghi, submitted to J. Appl. Phys.

130. Hj. Matzke and J.L. Whitton, Can. J. Phys. 44,995 (1966).

131. J.R. Parsons, Phil. Mag. 12, 1159 (1965).

132. J.F. Gibbons, E.O. Hechtl, and T. Tsurushima, Appl. Phys. Letters 15, 117 (1969).

133. R. Kelly, Rad. Effects 2, 281 (1970).

134. F.F. Morehead and B.L. Crowder, to be published.

135. M.L. Swanson, J.R. Parsons, and C.W. Hoelke, Rad. Effects (in press).

136. R. Comes, M. Lambert, and A. Guinier, Proc. Conf. on Radiation Damage, Cairo, 1966, p. 319 (Plenum Press, N.Y., 1967).

137. P. Sigmund, Appl. Phys. Letters 14, 114 (1969).

138. J. Lindhard, V. Nielsen, M. Scharff, and P.V. Thomsen, Kgl. Danske

Videnskab. Selskab, Mat.-Fys. Medd. 33, no. 10 (1963).

139. G.W. Arnold and W.D. Compton, Phys. Rev. Letters 4, 66 (1960).

140. S. Lungu, Phys. Stat. Sol. 23, 147 (1967).

141. J.E. Westmoreland and P. Sigmund, Rad. Effects 6, 187 (1970).